Astronomy Letters, Vol. 31, No. 5, 2005, pp. 291–298. Translated from Pis'ma v Astronomicheskiĭ Zhurnal, Vol. 31, No. 5, 2005, pp. 323–331.

Superlong Gamma-Ray Bursts

Ya. Yu. Tikhomirova[1*] and B. E. Stern[1,2]

[1] *Astro Space Centre, Lebedev Physical Institute, Russian Academy of Sciences, Profsoyuznaya ul. 84/32, Moscow, 117997 Russia*

[2] *Nuclear Research Institute, Russian Academy of Sciences, pr. Shestidesyatiletiya Oktyabrya 7a, Moscow, 117312 Russia*

Received December 24, 2004

Abstract—We searched for anomalously long gamma-ray bursts (GRBs) in the archival records of the Burst and Transient Sources Experiment (BATSE). Ten obvious superlong (>500 s) GRBs with almost continuous emission episodes were found. Nine of these events were known from the BATSE catalog, but five had no duration estimates; we found one burst for the first time. We also detected events with emission episodes separated by a long period of quiescence (up to ~1000 s) with a total duration of 1000–2000 s. In the latter case, we cannot reach an unequivocal conclusion about a common origin of the episodes due to the BATSE poor angular resolution. However, for most of these pairs, the probability of independent GRBs coinciding is much lower than unity, and the probability that all of these are coincidences is $\sim 10^{-8}$. All of the events have a hardness ratio (the ratio of the count rates in different energy channels) typical of GRBs, and their unique duration is unlikely to be related to their high redshifts. Superlong bursts do not differ in their properties from typical long (>2 s) GRBs. We estimated the fraction of superlong GRBs (>500 s) among the long (>2 s) GRBs in the BATSE sample with fluxes up to 0.1 ph cm^{-2} s^{-1} to be between 0.3 and 0.5%, which is higher than the estimate based on the BATSE catalog. © *2005 Pleiades Publishing, Inc.*

Key words: *gamma-ray bursts*.

INTRODUCTION

At present, it is well known that the events beginning as cosmic gamma-ray bursts (GRBs), isolated nonrecurrent bursts with very different light-curve profiles commonly observed in the energy range from tens to hundreds of keV, are subsequently followed by optical and X-ray emission (van Paradijs *et al.* 2000). The following important question remains: how long do these events last in the gamma-ray range (GRBs proper)? There is no universally accepted model of the physical GRB emission mechanism (although the question of their association with a certain class of supernovae seems to have been solved), and the existence of anomalously long GRBs can impose significant constraints on the model of this mechanism.

BATSE was the most sensitive among the experiments in which GRBs were observed (Fishman 1989). Furthermore, this was an experiment in which continuous all-sky monitoring was performed in the energy range 25 keV–1 MeV during a uniquely long period of 9.1 yr (1991–2000). Before the beginning of this experiment, GRBs were considered to be a unified class of events with a duration of up to ~100 s (Mazets *et al.* 1981). According to the BATSE catalog (http://gammaray.msfc.nasa.gov/batse/grb/catalog/current/, see Table 1), more than a hundred events with a duration of 100–500 s, three events with a duration of 500–1000 s, and one event with longest duration of 1300 s were detected during the BATSE experiment among ~2700 bursts.

In addition, a subclass of short bursts with a duration below ~2 s (Kouveliotou 1993) with harder spectra that account for a quarter of the total number of BATSE GRBs was revealed.

There are several types of BATSE records, in particular, records of the continuous all-sky monitoring by eight BATSE detectors with a time resolution of 1024 ms in four energy channels (DISCLA) and with a time resolution of 2048 ms in 16 channels (CONT) in the energy range 25–1000 keV.

Recently, Connaughton (2002) searched for long-lived GRB emission in the CONT records. Having added up the episodes of records from the burst trigger to thousands of seconds for hundreds of events, she found that the signal extends to ~1000 s and is observable even longer. Since bursts with an emission episode widely separated from the main peak were excluded from the analysis, this suggests that the

*E-mail: jana@anubis.asc.rssi.ru

Table 1. Statistics of superlong GRBs found from BATSE data

GRB sample	Number of bursts with $T > 500$ s	
	500–1000 s	1000–2000 s
BATSE catalog* (according to table of durations)	3	1
UC catalog by Stern and Tikhomirova** (search in BATSE DISCLA records)	5	1
Superlong candidate pairs in UC catalog	1	6

* Accessible at http://gammaray.msfc.nasa.gov/batse/grb/catalog/current./
** Accessible at http://www.astro.su.se/groups/head/grb_archive.html

emission of long GRBs on time scales of ~1000 s could be their common feature.

Whereas Connaughton (2002) applied a statistical approach, we used an individual approach and searched for anomalously long bursts in the BATSE DISCLA records.

THE SEARCH FOR SUPERLONG (>500 s) GRBs

We scanned the records of the photon count rate in each of the eight BATSE detectors in two of the four energy channels, 50–100 and 100–300 keV (which coincides with the triggering spectral range in BATSE itself) with a time resolution of 1024 ms over the entire period of BATSE observations, 9.1 yr. The scanning was performed as part of our search for nontriggered GRBs (Stern *et al.* 2000, 2001). However, special attention was paid to the search for anomalously long bursts, including those with unusual profiles; additional runs of records with variations of the main search criteria were carried out.

By nontriggered bursts we mean events whose parameters did not satisfy the triggering criteria (most frequently due to a low intensity) in the main event-detection procedure; therefore, these events were missed and were not detected during the experiment itself. However, being statistically significant and reliably classifiable, these can be found in the BATSE records. In contrast to the BATSE catalog, which contains GRBs with a peak flux down to ~0.2 ph cm^{-2} s^{-1} (Paciesas *et al.* 1999), the search for nontriggered events by Stern *et al.* (2001) revealed bursts with a peak flux down to ~0.1 ph cm^{-2} s^{-1}.

Our scans of the DISCLA records revealed a total of 3906 GRBs (see the catalog by Stern and Tikhomirova at http://www.astro.su.se/English/groups/head/grb_archive.html and Stern *et al.* (2001)); 1838 of these were new, previously unknown, nontriggered events, and 2068 were GRBs known from the BATSE catalog. Among all the detected GRBs, ten were obvious superlong events with a duration longer than 500 s (see Fig. 1 and Table 1). Nine of these were known triggered events from the BATSE catalog, but only four of the nine events were known as superlong bursts, according to the table of durations in the catalog. Our estimates for the five remaining GRBs and one nontriggered GRB found for the first time are given in Table 2. Only one of these six bursts, GRB 910425, has an estimate of its duration in the BATSE catalog, $t_{90} = 430$ s, which is clearly indicative of the loss of episodes and the underestimation of the event duration.

Note that the parameter T_{90}, the time in which from 5 to 95% of the total burst fluence is radiated, is commonly used as the GRB duration. Here, however, we study the maximum duration of the gamma-ray emission, and it is inappropriate to use this parameter. Therefore, in this paper, we use mainly an estimate of the total burst duration by visually determining the beginning and the end of the event. In addition, it is more difficult to estimate T_{90} for superlong >500 s bursts in the BATSE DISCLA records than for ≤100 s bursts, since the fluctuations of the high, strongly variable background are difficult to take into account on long time scales. Data gaps are also occasionally encountered in the records, making this estimate impossible.

The longest of the six bursts whose duration was either not estimated or underestimated in the BATSE catalog, GRB 971208 (see Fig. 1), is known from Connaughton *et al.* (1997) and is unique in its own way. It has a classical fast rise exponential decay profile. However, it has both an anomalously long rise time, ~70 s, and an anomalously long tail. This burst has a smooth profile and the longest duration, ~1000 s, among the bursts with a classical profile (the second longest burst with a similar profile has a duration of ~250 s). After ~1000 s, the record is interrupted for ~500 s, which does not allow us to estimate the duration of this burst more accurately.

Table 2. Obvious superlong (>500 s) GRBs found in the BATSE DISCLA archival records

Date (TJD)	Seconds of day	Catalog entry	T, s	α, deg	δ, deg	R, deg[a]	F^{b}_{peak}, ph cm^{-2} s^{-1}	HR[c] 2 + 3/1
Superlong, with duration not (under)estimated in BATSE catalog								
971 208	**28 085**	**UC 10790a**	**1000**	**355.8**	**76.2**	**0.4**	**2.0**	**2.36**
(10 790)	28 092	BATSE 6526	None	356.5	77.9	1.2	1.8	
960 425	**1102**	**UC 10198a**	**740**	**64.3**	**45.5**	**9.7**	**0.45**	**2.38**
(10 198)	1113	BATSE 5446	None	59.9	40.8	5.1	0.44	
981 104	**8114**	**UC 11121a**	**730**	**108.5**	**11.5**	**3.2**	**1.27**	**2.26**
(11 121)	8160	BATSE 7188	None	104.3	12.4	2.8	None	
990 123	**5838**	**UC 11201a**	**660**	**87.7**	**−4.4**	**9.7**	**0.33**	**4.1**
(11 201)	nontriggered							
910 425	**20 208**	**UC 8371c**	**610**	**341.8**	**25.0**	**7.9**	**0.45**	**3.11**
(8371)	20 253	BATSE 110	430[d]	335.9	25.8	4.8	0.37	
981 219	**34 133**	**UC 11166b**	**530**	**216.0**	**−44.6**	**5.5**	**0.88**	**3.8**
(11 166)	33 948	BATSE 7270	None	218.9	−43.6	2.0	0.9	
Superlong, already known from BATSE catalog								
970315	**80 021**	**UC 10522d**	**1360**	**129.9**	**−52.6**	**3.5**	**0.66**	**3.8**
(10522)	80 022	BATSE 6125	1307.	130.6	−52.4	0.99	None	
950305	**54 303**	**UC 9781b**	**930**	**195.5**	**−12.2**	**0.9**	**8.17**	**3.05**
(9781)	54 305	BATSE 3458	674.	197.2	−11.1	0.3	8.1	
971029	**22 424**	**UC 10750b**	**730**	**70.7**	**−40.5**	**1.5**	**1.73**	**3.27**
(10750)	22 429	BATSE 6454	616.	66.9	−45.0	1.3	1.62	
950509	**83 719**	**UC 9846b**	**700**	**41.6**	**27.0**	**6.8**	**1.26**	**1.71**
(9846)	83 766	BATSE 3567	590.	44.4	22.9	3.2	1.05	

[a] Radius of the error box.

[b] Peak flux in the BATSE spectral channels 2–3 (50–300 keV).

[c] Hardness as the ratio of the total count rates in the BATSE spectral channels 2–3 (50–300 keV) to the total count rates in one spectral channel (25–50 keV).

[d] t_{90}.

An important point is that, for an anomalously long burst, its episodes can be detected as independent events, particularly if the interval of silence between the episodes is much longer than their duration. Therefore, we checked all of the GRBs found in the BATSE records for the presence of correlated pairs, which could be episodes of anomalously long events. We searched for bursts that were separated by no more than 2000 s and that had overlapping error boxes. We found nine pairs of such events.

In view of the specific properties of gamma-ray detectors, the localization accuracy for these GRBs is very low, ~10°. Therefore, we cannot reliably determine whether each of the pairs found is a superlong burst from the same source or independent bursts from different sources. Invoking data from the *Ulysses* interplanetary spacecraft (Hurley 2004), which operated simultaneously with BATSE in the same spectral range, for a triangulation attempt did not allow us to clarify the situation due to the low sensitivity (in all cases, *Ulysses* does not see one of the episodes), and we can estimate the confidence level only theoretically.

For each of the nine pairs, we estimated the expectation of the observation of two independent bursts in the sample of detected GRBs with a separation in

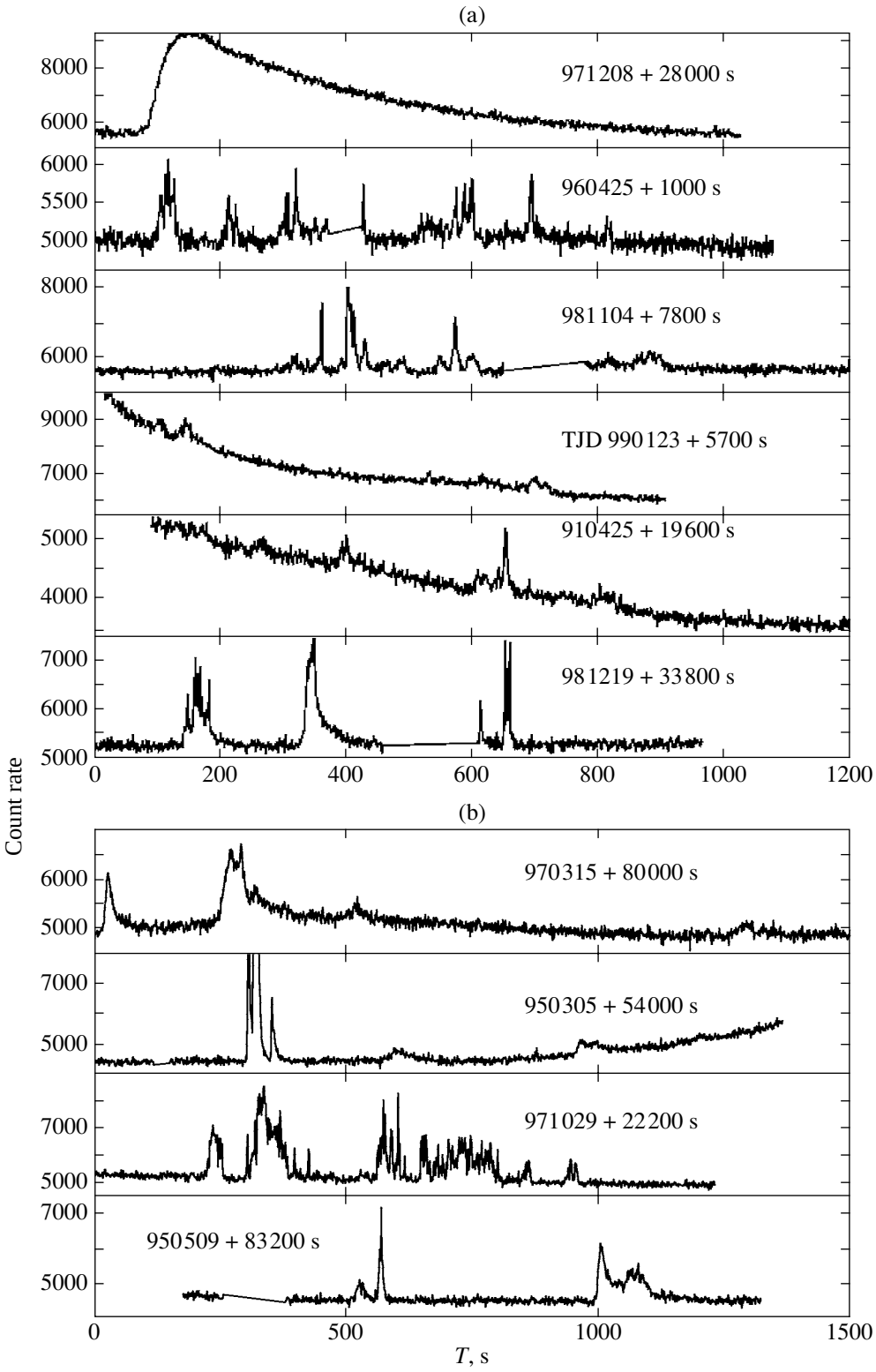

Fig. 1. Fragments of the BATSE DISCLA records containing obvious superlong (>500 s) GRBs: (a) events whose duration was not estimated or underestimated in the BATSE catalog and (b) superlong events known from the BATSE catalog. The sum of the photon count rates in two of the eight BATSE detectors with a maximum flux (the second and third energy channels, 50–300 keV) is shown. The date and seconds of the day are indicated for each burst.

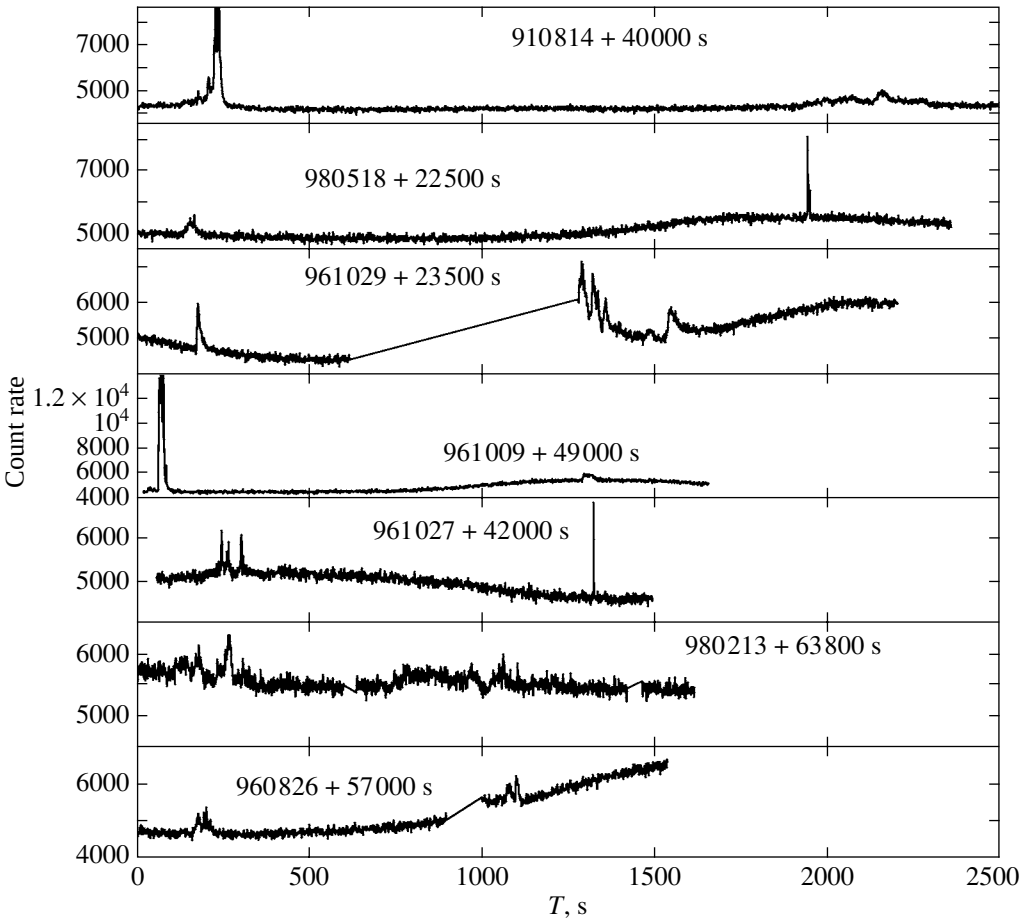

Fig. 2. Fragments of the BATSE DISCLA records containing the detected pairs of GRBs that could be single superlong bursts. The sum of the photon count rates in two of the eight BATSE detectors with a maximum flux (the second and third energy channels, 50–300 keV) is shown. The date and seconds of the day are indicated for each event.

angle and time no larger than a given value and with fluxes no lower than given values:

$$P = \frac{(1-\cos\delta)}{2}\Delta T R_{\rm GRB} N(F_p),$$

where δ is the angular separation between the episodes, ΔT is the time interval between them, $R_{\rm GRB}$ is the GRB detection rate ($R_{\rm GRB} = N/(T_{\rm obs}\eta) = 1.75\times10^{-5}$ s^{-1}, $N = 3400$ is the total number of detected long GRBs, $T_{\rm obs} = 9.1$ yr is the BATSE operation time, $\eta = 0.7$ is the exposure factor that includes the gaps in the data and the periods of a high background), and $N(F_p)$ is the number of detected bursts with fluxes no lower than a given value. We introduced the last factor in such a form, because the probability of detecting both episodes (if these have a common origin) depends on the brightness of the event.

For two pairs, this number was >1, and these were excluded from the analysis. We consider the remaining seven pairs as candidates for superlong GRBs. Their duration from the beginning of the first episode to the end of the last episode ranges from ~950 to ~2300 s. The probability of seven such pairs of independent bursts in the sample coinciding is roughly equal to the product of their expectations, $\sim10^{-8}$; i.e., at least some of the pairs found are superlong bursts with a high probability.

The light curves of the detected pairs are shown in Fig. 2, and some of their parameters, including the expectation of a coincidence, are listed in Table 3. Both events were triggered, detected during BATSE, and included in the catalog as independent events, only in two pairs. In two of the remaining pairs, both events were nontriggered; these were not detected during BATSE (probably because of their low intensity). We detected them when scanning the BATSE DISCLA records. In the three remaining events, one burst is nontriggered and another is triggered.

It should be noted that the BATSE observational algorithm was not intended for the detection of superlong GRBs: during the detection immediately after

Table 3. Pairs of GRBs, candidates for single superlong (>500 s) bursts found in the BATSE DISCLA archival records

Date (TJD)	Seconds of day	Catalog entry	T_{total}, s (T_{event})	α, deg	δ, deg	R, deg	F_{peak}, ph cm^{-2} s^{-1}	HR, 2, 3/1
			2300 $P = 0.06$					
910 814	**40 132**	**UC 08482c**	**72.**	**62.2**	**46.8**	**0.8**	**4.29**	**3.46**
(08482)	40 180	BATSE 676	78.	58.0	45.2	1.0	4.08	
	41 941	**UC 08482d**	**324.**	**60.0**	**35.3**	**3.1**	**0.58**	**2.12**
	–	–	–	–	–	–	–	
			1810 $P = 0.03$					
980 518	**22 649**	**UC 10951a**	**42.**	**160.3**	**−44.5**	**11.1**	**0.35**	**1.69**
(10 951)	–	–	–	–	–	–	–	
	24 441	**UC 10951b**	**8.**	**164.2**	**−41.9**	**5.4**	**1.34**	**2.4**
	24441	BATSE 6762	8.	162.1	−42.5	2.0	1.46	
			1500 $P = 0.02$					
961 029	**23 676**	**UC 10385b**	**24.**	**62.1**	**−53.5**	**6.5**	**0.57**	**2.34**
(10 385)	23 677	BATSE 5648	40.	59.4	−52.6	3.3	0.84	
	24 781	**UC 10385c**	**49.**	**56.4**	**−53.0**	**1.8**	**0.67**	**1.68**
	24 350	BATSE 5649	None	59.8	−48.9	0.3	None	
			1300 $P = 0.007$					
961 009	**49 065**	**UC 10365c**	**20.**	**135.5**	**−79.0**	**1.1**	**6.69**	**2.91**
(10 365)	49 065	BATSE 5629	None	130.2	-80.2	0.4	6.4	
	50 292	**UC 10365d**	**36.**	**110.2**	**−79.0**	**6.6**	**0.25**	**2.57**
	–	–	–	–	–	–	–	
			1150 $P = 0.2$					
961 027	**42 247**	**UC 10383d**	**75.**	**72.0**	**−43.5**	**10.4**	**0.42**	**3.04**
(10 383)	42 247	BATSE 5646	109.	67.4	−42.4	5.6	109.	0.47
	43 323	**UC 10383e**	**2.**	**84.4**	**−51.0**	**17.4**	**0.78**	**8.2**
	43 322	BATSE 5647	1.	68.7	−54.3	5.8	0.85	
			1000 $P = 0.7$					
980 213	**63 928**	**UC 10857c**	**198.**	**11.1**	**−23.8**	**7.4**	**0.33**	**2.23**
(10 857)	64 849	UC 10857d	104.	6.2	−10.6	13.1	0.25	2.7
			950 $P = 0.6$					
960 826	**57 175**	**UC 10321d**	**45.**	**191.1**	**15.8**	**10.2**	**0.32**	**1.68**
(10 321)	58 072	UC 10321e	34.	191.1	28.3	12.6	0.23	4.63

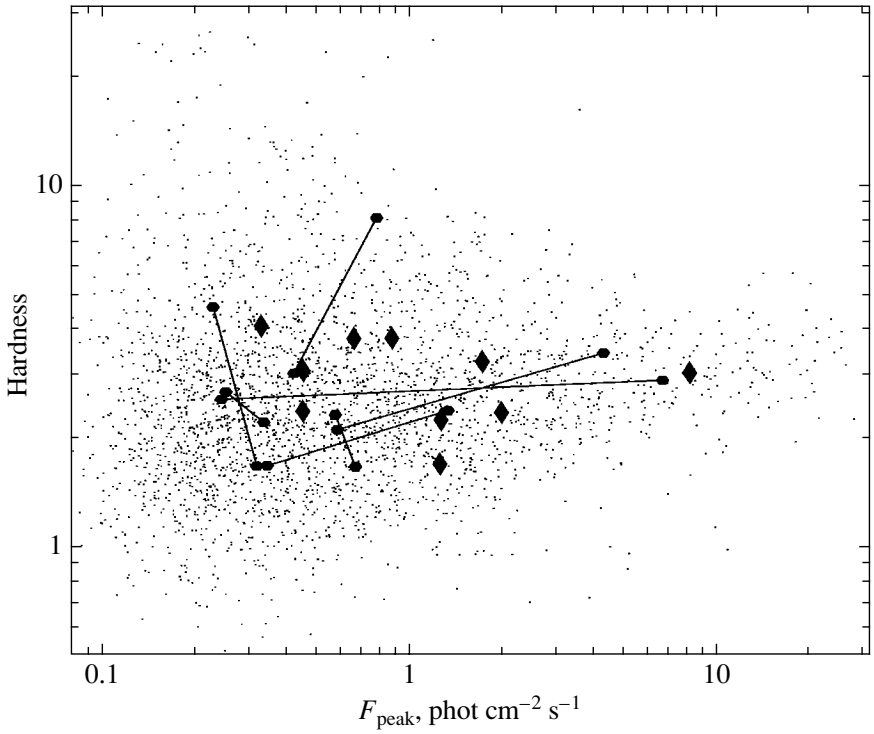

Fig. 3. Hardness of the GRBs found in the BATSE DISCLA records as the ratio of the count rates in the energy ranges 50–300 keV (spectral channels 2 and 3) and 25–50 keV (channel 1). The peak photon flux in the energy range 50–300 keV is along the horizontal axis; the diamonds indicate the obvious superlong events from Table 2; the dumbbells indicate the correlated pairs of events that are candidates for superlong bursts; the dots indicate GRBs from the catalog by Stern *et al.* (2002).

the accumulation of limited information, data were transmitted from the satellite to the Earth; during the data transmission, another event was detected only if it was more intense than the previous one. Hence, the remote faint episodes of anomalously long bursts have been lost, and it is possibly these events that we found in the BATSE records as pairs 910814 and 961009 (Fig. 2).

Note that we searched for pairs of bursts as possible episodes of superlong bursts separated by a time interval of ~2000 s. For a longer interval, the expectation of a coincidence of two independent bursts in the sample is ≥ 1 for most pairs, and no possible candidates for superlong bursts can be identified. However, since no obvious superlong GRBs (with almost continuous emission) with a duration $\geq$2000 s were found over the long period of BATSE observations, such superlong bursts probably do not exist, because a wide morphology of light curves is typical of any duration.

Like obvious superlong bursts, the pairs do not differ from typical long bursts in their parameters, except their duration (see Table 3). In general, their light curves (Fig. 2) represent a wide morphology of the profiles typical of GRBs. Their hardness is typical of GRBs (Fig. 3). The second episode in a pair can be either harder or softer, more or less intense. There is no reason to believe that the second episode in a pair can be produced by a different physical mechanism, as in the case of afterglow.

No counterparts were observed for these events in other spectral ranges. Given the broad distribution of the intrinsic GRB luminosities (Stern *et al.* 2002), it is difficult to estimate the distance to the sources of these bursts from their brightness; however, these are clearly neither the nearest nor the farthest GRBs. If the time dilation due to the unusually high redshift were responsible for the anomalous duration, this would affect the hardness of these GRBs, which is not observed.

We present the duration distribution for all the long GRBs found in the BATSE DISCLA records, including the detected obvious superlong bursts and superlong candidate pairs (Fig. 4). Since data gaps are regularly encountered in the records and a considerable part of the sky is blocked by the Earth when observing from a satellite, the probability that superlong bursts could be identified as such in the

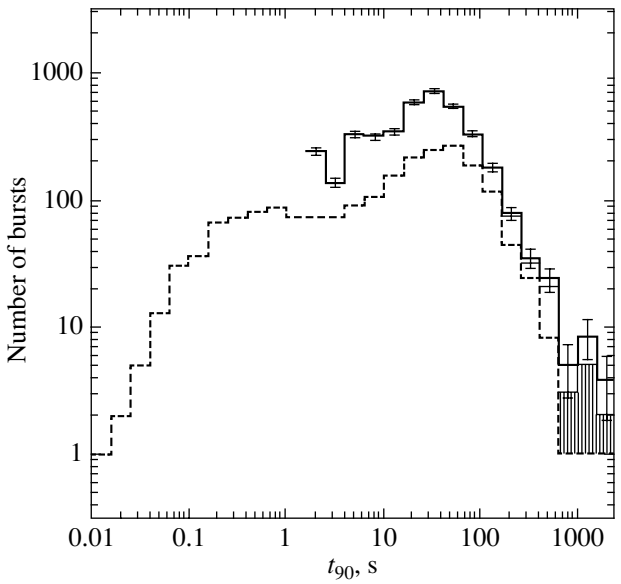

Fig. 4. GRB duration distribution. The thin line indicates the GRBs found in the BATSE DISCLA records with the superlong bursts found here, including the correlated pairs; we use a visual estimate of the total duration for the superlong bursts and t_{90} for the remaining events; the thick line indicates the same distribution corrected for the probability of observing the total event duration; the dashed line indicates the distribution of durations according to the BATSE catalog.

records (without the loss of episodes) is lower than that for moderate-duration bursts. We therefore estimated the probability of identifying superlong GRBs in the records by the Monte Carlo method. For superlong bursts, we estimated the probability that no less than 90% of the duration of their emission will be seen in the records. The distribution of GRB durations corrected for this probability declines toward the longer durations, which roughly corresponds to a power law $dN/dT \propto T^{-1.5}$.

CONCLUSIONS

We scanned the BATSE continuous all-sky monitoring records in the energy range 25 keV–1 MeV for the entire observing period of 9.1 yr and found ten superlong (>500 s) GRBs. The two longest bursts have a duration of ~1000–1360 s. For four of the ten bursts, their duration is known from the BATSE catalog; for the remaining bursts, we give an estimate of their duration for the first time, including that for one newly detected, nontriggered GRB. The fraction of obvious superlong (>500 s) GRBs among all of the long (>2 s) bursts found in the records is 0.3%, which is slightly higher than the estimate that follows from the BATSE catalog. Superlong bursts do not differ in their main properties from long bursts.

In addition, we detected bursts that could in pairs be episodes of superlong bursts with a duration of 1000–2300 s. With these events, the fraction of superlong bursts in the class of long GRBs reaches 0.5%. The existence of such long bursts (~2000 s) requires confirmation (or disproof) by future experiments with a high GRB localization accuracy. The extension of the GRB emission on time scales >2500 s is unlikely.

The extension of the gamma-ray emission to time scales of ~1000 s and farther from the beginning of a GRB must be explained in terms of existing models and be taken into account when searching for an early X-ray afterglow.

ACKNOWLEDGMENTS

This work was supported by a 2004 grant from the Foundation of Support for Russian Science for young scientists, the Russian Foundation for Basic Research (project no. 04-02-16987), the Leading Scientific School (no. Sh-1653.2003.2) and a NORDITA grant (the Nordic Project in High-Energy Astrophysics in the INTEGRAL Era).

REFERENCES

1. V. Connaughton, Astrophys. J. **567**, 1028 (2002).
2. V. Connaughton, M. Kippen, R. Priece, and K. Hurley, IAU Circ. **6785**, 1 (1997).
3. G. J. Fishman, *The Gamma Ray Observatory Science Workshop*, Ed. by W. N. Johnson (GSFC, Greenbelt, 1989), p. 3.
4. K. Hurley (2004) (private communication).
5. C. Kouveliotou, C. Meegan, G. Fishman, *et al.*, Astrophys. J. Lett. **413**, L101 (1993).
6. E. Mazets, S. Golenetskii, V. Il'Inskii, *et al.*, Astrophys. Space Sci. **80**, 85 (1981).
7. W. Paciesas, C. Meegan, G. Pendleton, *et al.*, Astrophys. J., Suppl. Ser. **122**, 465 (1999).
8. B. E. Stern, Ya. Tikhomirova, D. Kompaneets, *et al.*, Astrophys. J. **563**, 80 (2001).
9. B. E. Stern, Ya. Tikhomirova, M. Stepanov, *et al.*, Astrophys. J. Lett. **540**, L21 (2000).
10. B. E. Stern, Ya. Tikhomirova, and R. Svensson, Astrophys. J. **573**, 75 (2002).
11. J. van Paradijs, C. Kouveliotou, and A. M. J. Wijers, Annu. Rev. Astron. Astrophys. **38**, 379 (2000).

Translated by G. Rudnitskiĭ

Astronomy Letters, Vol. 31, No. 5, 2005, pp. 299–307. Translated from Pis'ma v Astronomicheskiĭ Zhurnal, Vol. 31, No. 5, 2005, pp. 332–341.

Infrared Luminosities of Local-Volume Galaxies

I. D. Karachentsev[1]* and A. M. Kutkin[2]

[1] *Special Astrophysical Observatory, Russian Academy of Sciences, Nizhniĭ Arkhyz, 357147 Karachai-Cherkessian Republic, Russia*

[2] *Sternberg Astronomical Institute, Universitetskiĭ pr. 13, Moscow, 119992 Russia*

Received October 28, 2004

Abstract—Based on data from the Two-Micrometer All-Sky Survey (2MASS), we analyzed the infrared properties of 451 Local-Volume galaxies at distances $D \leq 10$ Mpc. We determined the K-band luminosity function of the galaxies in the range of absolute magnitudes from -25^m to -11^m. The local luminosity density within 8 Mpc is $6.8 \times 10^8 L_\odot$ Mpc^{-3}, a factor of 1.5 ± 0.1 higher than the global mean K-band luminosity density. We determined the ratios of the virial mass to the K-band luminosity for nearby groups and clusters of galaxies. In the luminosity range from 5×10^{10} to $2 \times 10^{13} L_\odot$, the dependence $\log(M/L_K) \propto (0.27 \pm 0.03) \log L_K$ with a dispersion of $\sim$0.1 comparable to the measurement errors of the masses and luminosities of the systems of galaxies holds for the groups and clusters of galaxies. The ensemble-averaged ratio, $\langle M/L_K \rangle \simeq (20\text{–}25) M_\odot/L_\odot$, was found to be much smaller than the expected global ratio, $(80\text{–}90) M_\odot/L_\odot$, in the standard model with $\Omega_m = 0.27$. This discrepancy can be eliminated if the bulk of the dark matter in the Universe is not associated with galaxies and their systems.

Key words: *galaxies, groups and clusters of galaxies, galaxy masses and luminosities, dark matter.*

INTRODUCTION

The recently published catalog of nearby galaxies by Karachentsev *et al.* (2004) contains basic observational data on 451 galaxies within 10 Mpc of our Galaxy. Apart from distances and radial velocities, this catalog includes various optical parameters of galaxies: apparent B magnitudes, angular sizes, morphological types, and H I line fluxes and widths. The data presented in the catalog allow such important properties of the Local Volume as the luminosity function, the local luminosity density, the baryon mass density, or the H I mass to be determined. Being least affected by observational selection, a distance-limited (not flux-limited) sample of galaxies is a suitable standard to be compared with distant samples (like the Hubble Deep Field) when analyzing the various effects of galaxy evolution.

However, a detailed analysis of the evolutionary effects requires photometric data for the Local-Volume galaxies not only in the B band, but also in other photometric bands, particularly in the near infrared. There are two main reasons for this: (1) the variable luminosity of the young stellar population of galaxies, which increases during starbursts, makes a small contribution to the total IR luminosity of the galaxy; and (2) the reduction in the IR luminosity of the galaxy due to the absorption of light in its dust clouds is much smaller than that in the B band. For these reasons, the IR luminosity of a galaxy is a more reliable indicator of its baryon mass than the optical luminosity.

In recent years, the entire northern and southern sky has been surveyed in IR bands: $J(1.11\text{–}1.36)\mu$, $H(1.50\text{–}1.80)\mu$, and $K_s(2.00\text{–}2.32)\mu$ (the 2MASS survey). This survey was used to compile the XSC catalog of extended objects, which numbers about 1.65 million galaxies with apparent magnitudes $K_s < 14^m$ and angular sizes larger than $10''$ (Cutri and Skrutskie 1998; Jarrett 2000). The various photometric and morphological properties of this huge sample of galaxies were described by Jarrett *et al.* (2000, 2003). We used 2MASS data to determine the J, H, K magnitudes for the Local-Volume galaxies.

THE LOCAL-VOLUME GALAXIES SEEN IN THE 2MASS SURVEY

We used the NASA Extragalactic Database (NED) to examine the infrared J, H, K images of all galaxies with distance estimates within 10 Mpc. After excluding several dubious identifications of a distant 2MASS source with a nearby galaxy, we obtained a sample of 122 galaxies for which the 2MASS XSC catalog gives the magnitudes $J_{\rm ext}$, $H_{\rm ext}$, and $K_{\rm ext}$.

*E-mail: ikar@luna.sao.ru

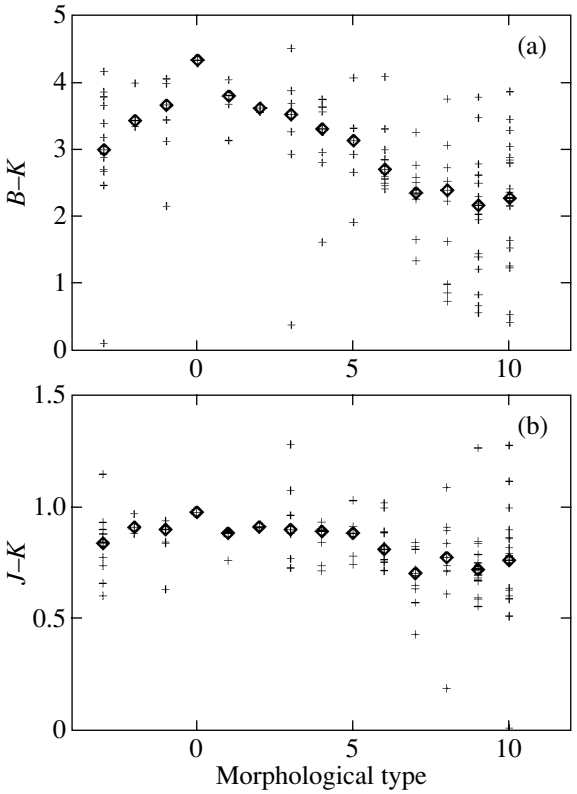

Fig. 1. (a) $B-K$ and (b) $J-K$ color indices for 122 Local-Volume galaxies of various morphological types. The diamond signs indicate the median values. The color indices were corrected for the extinction in our Galaxy.

In contrast to the measured (isophotal) magnitudes, these include the contribution from the faint outer regions of galaxies that was determined by extrapolation using the standard brightness profile. Thus, only 27% of the Local-Volume galaxies were seen in the 2MASS survey. The short integration time ($\sim$8 s per frame), as a result of which the low-surface-brightness galaxies lie below the sensitivity threshold of the survey, $K = 20$, is responsible for the absence of many nearby galaxies in 2MASS. The low detection level in 2MASS is typical of a distance-limited sample. For example, among the flat spiral galaxies of the RFGC catalog with angular sizes larger than $0''.6$, the 2MASS detection level is 71% (Karachentsev *et al.* 2002). The visibility of a galaxy in 2MASS depends on its various characteristics: the morphological type, the absolute magnitude, and the mean surface brightness. To estimate the J, H, K magnitudes for the Local-Volume galaxies that are unseen in 2MASS, we plotted the $B-K$, $J-K$, and $H-K$ color indices for the detected galaxies against their morphological type and other parameters. Figure 1a shows the distribution of 122 nearby galaxies in $B-K$ and de Vaucouleurs morphological type. Each galaxy is represented by a cross, and the median $B-K$ values are indicated by diamonds. All apparent magnitudes were corrected for Galactic extinction: $A_J = 0.209A_B$, $A_H = 0.133A_B$, and $A_K = 0.085A_B$, where A_B is the B-band extinction estimated by Schlegel *et al.* (1998). These data show a systematic trend of the mean color index from $\langle B-K\rangle \simeq +4.0$ for early types to $\langle B-K\rangle \simeq 2.0$–$2.5$ for late types. The $J-K$ color index exhibits a similar trend (Fig. 1b). The derived dependences of the color indices on the morphological type of a galaxy agree satisfactorily with the data presented by Jarett *et al.* (2003) in their Figs. 20 and 23 for a larger sample of galaxies of various types. We used the morphological type–color index correlations from Jarett *et al.* (2003) to determine the J, H, K magnitudes for the nearby galaxies whose B magnitudes are given in the catalog by Karachentsev *et al.* (2004). The results are presented in Table 1.[1] The most commonly used names of the nearby galaxies are listed in the same sequence as in the original catalog. The 2MASS XSC IR magnitudes are given with two decimal figures, while our calculated J, H, K magnitudes are given with one decimal figure. A comparison of the various methods of estimating J, H, K magnitudes (from the morphological type, the absolute magnitude, or the surface brightness of the galaxy) showed that the typical error in the IR magnitudes is about $0^m.5$.

THE K-BAND LUMINOSITY FUNCTION FOR GALAXIES

We used the J, H, K magnitudes from Table 1 and the galaxy distance estimates from the catalog by Karachentsev *et al.* (2004) to determine the absolute magnitudes of all Local-Volume galaxies corrected for the Galactic extinction using data by Schlegel *et al.* (1998). Figure 2 shows the distribution of the sample of the nearest galaxies in J, H, and K absolute magnitudes. The brightest galaxy in the Local Volume, NGC 4594 (the "Sombrero" galaxy), has an absolute magnitude of $M_K = -24^m.91$, while the faintest Ursa Minoris dwarf systems have absolute magnitudes $M_K \sim -11^m$. The luminosity function in the J, H, K bands is at a maximum in the interval $[-15^m, -17^m]$.

Recently, Cole *et al.* (2001) determined the galaxy luminosity function in the J and K bands using the 2MASS photometry for 17 173 galaxies with measured redshifts from the 2dF survey. According to these authors, the K-band luminosity function is well represented by a Schechter function with the

[1] Table 1 is published in electronic form only and is available at ftp cdsarc.u-strasbg.fr/pub/cats/J (130.79.128.5) or http://cdsweb.u-strasbg.fr/pub/cats/J.

Table 2. Mass-to-luminosity ratios for galaxies and systems of galaxies in the K band

Object	$L_K, L_\odot$	$M, M_\odot$	$M/L_K, M_\odot/L_\odot$	Notes
Local-Volume galaxies	1.0×10^7	1.5×10^7	1.5 ± 0.2	M_{25}/L
Local-Volume galaxies	1.0×10^9	1.3×10^9	1.3 ± 0.2	M_{25}/L
Local-Volume galaxies	1.0×10^{11}	1.1×10^{11}	1.1 ± 0.2	M_{25}/L
N 5128 (<80 kpc)	1.1×10^{11}	5.0×10^{11}	4.7	Peng *et al.* (2004)
N 4636 (<35 kpc)	1.6×10^{11}	1.5×10^{12}	9.7	Loewenstein and Mushotzky (2002)
N 1399 (<106 kpc)	2.8×10^{11}	5.2×10^{12}	18.7 ± 5.7	Jones *et al.* (1997)
M 31 group	6.3×10^{10}	8.4×10^{11}	13.4	Karachentsev (2005)
Local group	1.1×10^{11}	1.2×10^{12}	11.2 ± 3.5	Karachentsev (2005)
M 81 group	1.5×10^{11}	1.6×10^{12}	10.6	Karachentsev (2005)
IC 342 group	5.6×10^{10}	7.6×10^{11}	13.5	Karachentsev (2005)
Maffei group	7.2×10^{10}	1.0×10^{12}	14.0	Karachentsev (2005)
M 83 group	6.8×10^{10}	1.0×10^{12}	15.2	Karachentsev (2005)
Cen A group	1.4×10^{11}	3.0×10^{12}	21.3	Karachentsev (2005)
Leo-I group	3.5×10^{11}	7.2×10^{12}	20.5	Karachentsev and Karachentseva (2004)
N 6946 group	6.8×10^{10}	8.0×10^{11}	11.7	Karachentsev *et al.* (2000)
Poor groups	7.6×10^{10}	1.3×10^{12}	17.0 ± 2.9	Guzik and Seljak (2002)
Fornax	1.8×10^{12}	5.9×10^{13}	32	Desai *et al.* (2003)
Virgo (<1.6 Mpc)	8.8×10^{12}	4.2×10^{14}	48 ± 6	McLaughlin (1999)
0024+1654	1.5×10^{13}	6.1×10^{14}	40 ± 7	Kneib *et al.* (2003)
MS0302+17 (<8 Mpc)	8.9×10^{12}	4.4×10^{14}	50 ± 5	Gavazzi *et al.* (2004)
Abell clusters	1.1×10^{13}	5.2×10^{14}	47 ± 3	Lin *et al.* (2003)
Coma (<14 Mpc)	2.7×10^{13}	1.4×10^{15}	54 ± 17	Rines *et al.* (2001)

parameters $M^* = -24.15$ (for the Hubble constant $H_0 = 72$ km s^{-1} Mpc^{-1}) and $\alpha = -0.96$ in the range from -26^m to -18^m. The luminosity functions for the 2MASS/2dF and Local-Volume samples are compared in Fig. 3a. The vertical bars indicate the statistical errors, $\sqrt{N_i}$. The mutual normalization of the two distributions was made near $M_K = -20\overset{m}{.}5$, where the two samples have comparable statistical errors. As might be expected, the luminosity function for the Local-Volume galaxies extends much further (by seven magnitudes) toward the dwarf galaxies. The agreement between the luminosity functions for the two samples may be considered satisfactory in the overlap region, in the interval $M_K = [-25^m, -18^m]$, although the differences reach two or three standard errors in some of the bins. The luminosity function for the 2dF sample is seen to be flatter in the range $M_K = [-19^m, -18^m]$. This is clearly due to the systematic shortage of galaxies in the 2MASS/2dF sample, because many low-luminosity and low-surface-brightness dwarf galaxies are not detectable in the 2MASS survey. Therefore, the luminosity function for the Local-Volume galaxies constructed only from the 122 objects detected in 2MASS (the crosses in Fig. 3a) agrees much better with the sample by Cole *et al.* (2001).

The data on Virgo galaxies that are available at http://goldmine.mib.infn.it/ offer another possibility for comparison. This compilation contains the K magnitudes for bright cluster members. For fainter members, we estimated their K magnitudes from the B magnitudes and the dependence of the mean $\langle B-K \rangle$ color index on the morphological type derived by Jarett *et al.* (2003). As a result, we constructed the luminosity function for 680 Virgo members, which is shown in Fig. 3b. The mutual normalization of the distributions for the Virgo members, the Local-Volume galaxies, and the 2MASS/2dF sample was

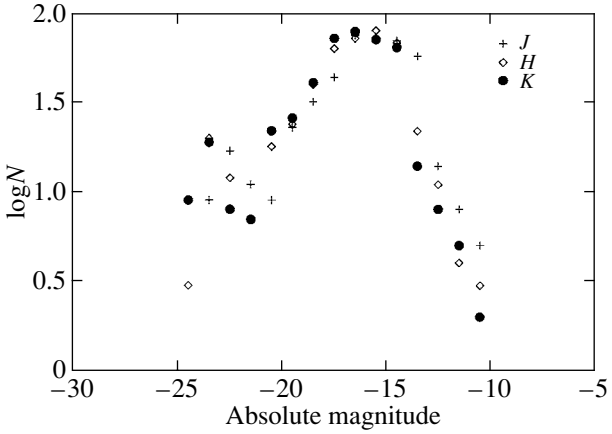

Fig. 2. Distribution of 451 Local-Volume galaxies in J, H, and K absolute magnitudes.

made at $M_K = -20\overset{m}{.}5$. The distance to the Virgo cluster was assumed to be 17.0 Mpc (Tonry *et al.* 2000). As we see from these data, the luminosity function for the Virgo cluster exhibits an excess in the region of supergiant galaxies, which is to be expected in the scenarios for the formation of the most massive galaxies through the mergers of normal and dwarf objects. The faint end of the luminosity function extends to $M_K = -13^m$, i.e., five magnitudes farther that that for the 2MASS/2dF sample. The systematic differences between the Virgo and Local-Volume samples at the faintest absolute magnitudes are clearly attributable to the underestimation of the total number of dwarf cluster members, which have no radial-velocity estimates as yet; therefore, these can be attributed neither to the Virgo members nor to the background.

Based on the distribution of Local-Volume galaxies in absolute magnitudes and distances, we calculated the mean luminosity density as a function of the radius of the sphere around our Galaxy. In Fig. 4, the luminosity density (in units of the solar luminosity per Mpc^3) is plotted against the distance at 0.5-Mpc steps separately for the J, H, and K bands. The mean luminosity density decreases by two orders of magnitude on the scales from 1 to 10 Mpc, reflecting the fractal nature of the distribution of galaxies. Karachentsev *et al.* (2004) estimated the completeness of their catalog within $D = 8$ Mpc in the number of galaxies to be $\sim 70\%$. The catalog may not include dwarf galaxies on the outskirts of the Local Volume ($D \simeq 5$–10 Mpc) and in the zone of strong absorption at Galactic latitudes $|b| \leq 10°$. However, the shortage of dwarf galaxies has virtually no effect on the estimated luminosity density, because more than 90% of the total luminosity is accounted for by the bright galaxies within four magnitudes of the brightest galaxy.

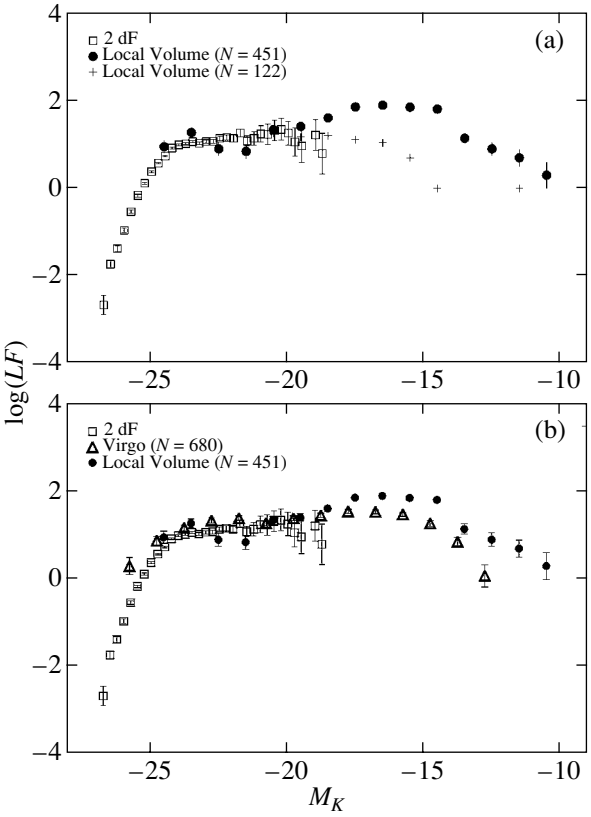

Fig. 3. K-band luminosity function (LF) for 451 Local-Volume galaxies (filled circles) in comparison with the luminosity function for the 2dF galaxies derived by Cole *et al.* (2001). The crosses (a) indicate the distribution for 122 Local-Volume galaxies, and the triangles (b) indicate the luminosity function for 680 Virgo cluster members.

Kochanek *et al.* (2001) and Bell *et al.* (2003) used the 2MASS photometry of galaxies to determine the global mean luminosity density in the K-band, j_K. These authors invoked the redshift data from the Sloan Digital Sky Survey and other sources to obtain $j_K = (5.1 \pm 0.5) \times 10^8$ and $(4.2 \pm 1.3) \times 10^8 L_\odot$ Mpc^{-3}, respectively. These values are shown in Fig. 4 by two horizontal lines. Thus, the mean local K-band luminosity density within 8 Mpc that we estimated, $6.8 \times 10^8 L_\odot /$ Mpc^3, is a factor of 1.4–1.6 higher than the global luminosity density. Note that the ratio of the local and global mean B-band luminosity densities is 1.7–2.0, but contains a significant uncertainty attributable to the different methods of correction for the internal extinction in galaxies.

THE MASS-TO-IR LUMINOSITY RATIO FOR NEARBY GALAXIES

About 2/3 of the Local-Volume galaxies have been detected in the H I line. This allowed their hydrogen

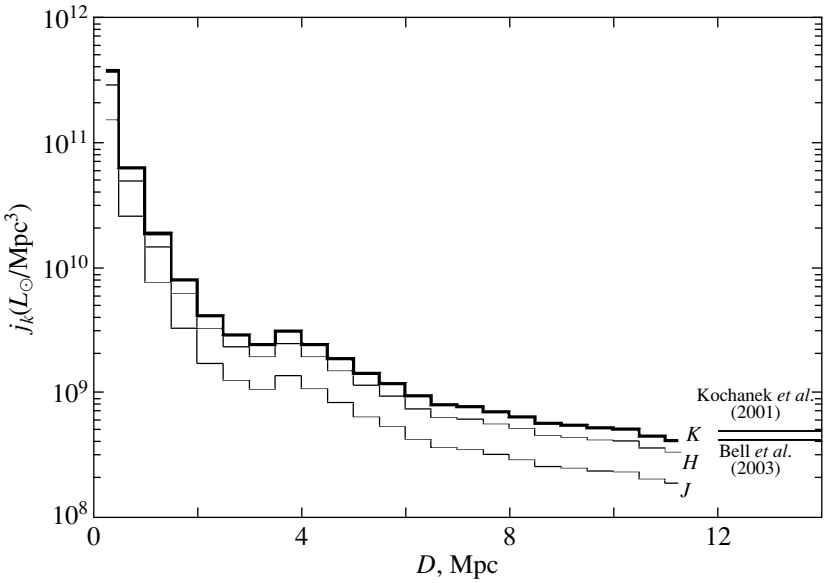

Fig. 4. J, H, and K-band galaxy luminosity density versus distance D in Mpc. The horizontal straight lines on the right indicate the global mean K-band densities from Kochanek *et al.* (2001) and Bell *et al.* (2003).

mass $M(\mathrm{H\,I})$ to be determined from the observed flux in the line and the total mass of the galaxy within the standard radius, M_{25}, from the H I line width and the inclination of the galaxy to the line of sight. The total mass-to-luminosity and hydrogen mass-to-luminosity ratios are important global parameters of a galaxy, which depend on the peculiarities of its evolution: the rate of gas transformation into stars, the merger frequency, etc. Karachentsev *et al.* (2004) discussed the distribution of Local-Volume galaxies in mass-to-blue luminosity ratio. Figure 5a shows the relationship between the calculated values of M_{25}/L in the B and K bands for nearby galaxies. Figure 5b shows a similar relationship for the hydrogen mass-to-luminosity ratios in the B and K bands. As follows from these data, the passage from the optical to IR luminosity of galaxies does not lead to the expected decrease in the dispersion of M_{25}/L and $M(\mathrm{H\,I})/L$. This is clearly attributable to the low accuracy of determining the total IR luminosities for nearby galaxies, which are dominated by low-surface-brightness dwarf systems.

Figure 6 shows the distributions of Local-Volume galaxies in total K-band luminosity and M_{25}/L_K ratio on a logarithmic scale. As follows from these data, the mean mass-to-luminosity ratio remains virtually constant, $(1.5 \pm 0.2)M_\odot/L_\odot$, as the IR luminosity of the galaxy changes by five orders of magnitude.

Based on the ideas of a Salpeter initial stellar mass function, Persic and Salucci (1992), Fukugita *et al.* (1996), Kochanek *et al.* (2001), and Cole *et al.* (2001) estimated the mean stellar mass density in the Universe. According to these authors and Bell *et al.* (2003), stellar mass component accounts for $\Omega_* = (2.8 \pm 0.8) \times 10^{-3}$ of the critical density at $H = 72\ \mathrm{km\ s^{-1}\ Mpc^{-1}}$ or $(M/L_K)_* = 0.95 \pm 0.27$ in units of the solar mass and luminosity. Thus, the mass of the stellar component (plus the gas mass) agrees, within the error limits, with the estimated mean mass of the galaxy within its standard radius. Therefore, the invisible forms of matter (dark halo) give a secondary contribution to the mass of the galaxy within its standard radius, and this applies to both normal and dwarf galaxies in the luminosity interval from 10^{11} to $10^6 L_\odot$.

THE MASS-TO-IR LUMINOSITY RATIO FOR SYSTEMS OF GALAXIES

The mass-to-luminosity ratios for systems of galaxies is known to increase as one goes from binary and triple systems to groups, clusters, and superclusters. The pattern of this dependence at optical wavelengths was discussed by Karachentsev (1966), Bahcall *et al.* (2000), and many other authors. There is reason to believe that in the infrared, this dependence could be more distinct than at optical wavelengths. Recently, Lin *et al.* (2003) analyzed the IR properties of 27 clusters and showed that the relationship between the mass and K-band luminosity of the clusters is given by $M/L_K \propto M^{0.31\pm0.09}$, where the total masses of the clusters were determined from their X-ray fluxes. The M/L_K ratios were also estimated for other systems of galaxies. These data are summarized in Table 2, where we also list the masses and K-band luminosities that we determined for nearby groups of galaxies. Column 1 of

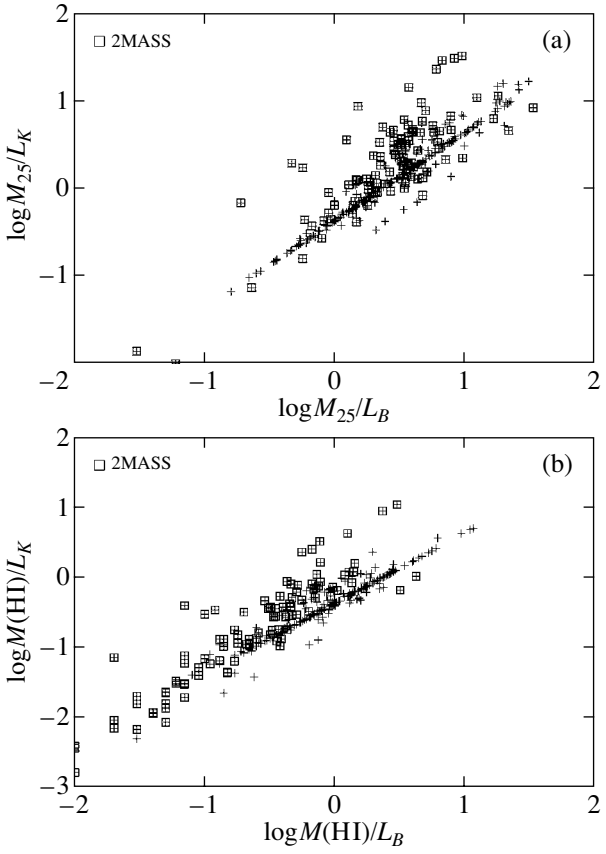

Fig. 5. Total mass (within the standard radius R_{25}) to luminosity (a) and hydrogen mass to luminosity (b) ratios in the B and K bands for the Local-Volume galaxies. The squares indicate the galaxies detected in 2MASS; the crosses indicate the objects whose K-band luminosities were determined from the $B{-}K$ color index and the morphological type.

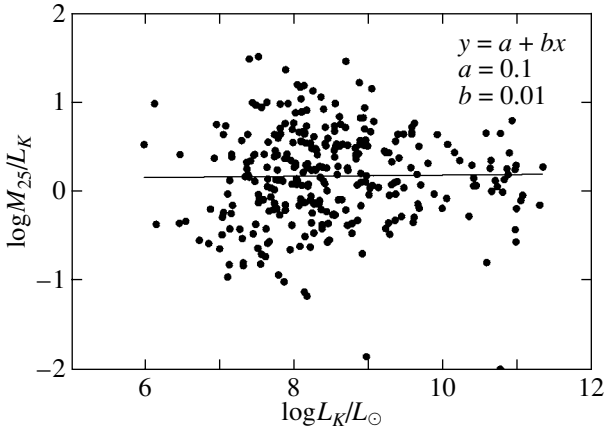

Fig. 6. Ratio of the total mass within the standard radius to the K-band luminosity for Local-Volume galaxies of various luminosities. The straight line indicates the linear regression with the parameters shown in the corner of the figure.

Table 2 gives the object/system name and, in certain cases, the scale on which the mass was estimated. Column 2 gives the total K-band luminosity of the object/system in units of the solar luminosity; columns 3 and 4 list the total mass and mass-to-total K-band luminosity ratio, respectively; and the last column contains references to the sources of the mass estimates. All data in Table 2 correspond to the Hubble constant $H_0 = 72$ km s^{-1} Mpc^{-1} and the absolute magnitude of the Sun, $M_{K,\odot} = 3^m.39$ (Kochanek *et al.* 2001).

Below, comment on the quantities listed in Table 2. The first three rows present the mean masses within the standard radius for the Local-Volume galaxies divided into three luminosity intervals. We determined the mean M_{25}/L_K ratios and their standard errors from the data shown in Fig. 6. The next three rows contain the total masses of the individual galaxies estimated from the radial-velocity dispersion of planetary nebulae in the elliptical galaxy NGC 5128 (on a 80-kpc scale) or from the X-ray flux for the elliptical galaxies NGC 4636 (in Virgo) and NGC 1399 (in Fornax). We took the K magnitudes of these galaxies from 2MASS.

The next seven rows in Table 2 contain the masses and luminosities of the nearest groups around the brightest galaxies: M 31, M 81, IC 342, Maffei 1, M 83, Cen A = NGC 5128, and the Local Group. The composition and dynamics of these groups was discussed by Karachentsev (2005). The masses of these groups listed in the table correspond to the means of the two estimates obtained using the virial theorem and the orbital motions of satellites. We estimated the total mass of the Local Group as a whole from the relation $M_t = (\pi^2/8G) \times R_0^3/T_0^2$, where R_0 is the observed radius of the zero-velocity sphere, T is the age of the Universe, and G is the gravitational constant. Two Local-Volume groups, Leo-I and NGC 6946, whose virial masses were determined by Karachentsev and Karachentseva (2004) and Karachentsev *et al.* (2000), respectively, with supplements by Makarov *et al.* (2003), were also added to the above groups.

Guzik and Seljak (2002) и Hoekstra *et al.* (2004) analyzed the effects of the weak gravitational lensing produced by single high-luminosity galaxies in the SDSS and RCS surveys. Such galaxies are usually the centers of poor (open) groups of galaxies. According to these authors, the lensing galaxies with a mean optical luminosity $L_B = 1.9 \times 10^{10} L_\odot$ have a typical mass of $(1.3 \pm 0.2) \times 10^{12} M_\odot$ on a scale $R \leq 260$ kpc. Assuming the mean color index to be $\langle B{-}K \rangle = 3.5$ for the field galaxies, we estimated their mean mass-to-K-band luminosity ratio to be

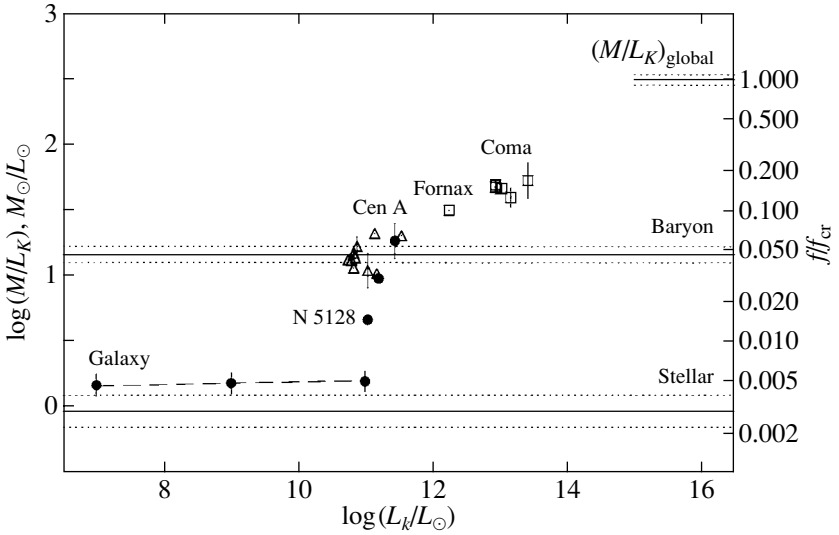

Fig. 7. Mass–K-band luminosity relation for galaxies and systems of galaxies. The three horizontal bands indicate the contributions of the stellar component (below) and the baryon mass as well as the global $(M/L_K)_{\rm global}$ value as the critical density-to-luminosity ratio (above). The right-hand scale corresponds to the mean matter density in units of the critical density.

$(17 \pm 3)M_\odot/L_\odot$, in good agreement with the data for nearby groups of galaxies.

The last six rows in Table 2 pertain to clusters and superclusters of galaxies. According to Tonry *et al.* (2001) and Jerjen (2003), the poor southern Fornax cluster is 20 ± 2 Mpc away. Ferguson (1989) published a catalog of 2678 galaxies in this cluster. At a radial-velocity dispersion of $\sim$400 km s^{-1} for the cluster members, the virial mass of Fornax is $5.9 \times 10^{13} M_\odot$ (Desai *et al.* 2004). We determined the IR luminosity of this cluster given in Table 2 from 2MASS data.

In a similar way, we estimated the total K-band luminosity of the other neares cluster of galaxies in Virgo. At the assumed Virgo distance of $D = 17$ Mpc, we obtained $L_K(\text{Virgo}) = 8.8 \times 10^{12} L_\odot$ for the virialized region of the cluster within 6° of its center. McLaughlin (1999) determined the virial mass of the cluster from the velocity dispersion of its member galaxies and the X-ray flux from the hot virialized gas. The mass of Virgo within 1.6 Mpc is $(4.2 \pm 0.5) \times 10^{14} M_\odot$, which yields $M/L_K = (48 \pm 6)M_\odot/L_\odot$. Note that Tully and Shaya (1984) and Tonry *et al.* (2000) obtained the cluster mass of $7 \times 10^{14} M_\odot$ in the model for the motion of galaxies around Virgo as an attractor. However, this estimate refers to a much larger volume with a radius of $\sim$8 Mpc, within which the total galaxy luminosity has not yet been found.

Recently, Kneib *et al.* (2003) and Gavazzi *et al.* (2004) used the effects of gravitational lensing to determine the masses of two rich clusters: 0024+1654 and MS0302+17. Their results are listed in Table 2. These authors measured the K-band luminosity for the former cluster. We estimated the K-band luminosity for the second cluster from its known B-band luminosity by assuming that the cluster is populated by early-type galaxies with the color index $\langle B-K \rangle = 4.0$.

The last two rows in Table 2 give the mean masses and K-band luminosities for the 27 clusters studied by Lin *et al.* (2003) and for the Coma supercluster (Rines *et al.* 2001). In the latter case, the M/L_K ratio was measured using the redshift survey for 1779 galaxies and their 2MASS photometry. Rines *et al.* (2001) pointed out that the derived mass-to-luminosity ratio remains approximately constant when going from the central virialized region with a radius of $\sim$3.5 Mpc to a scale of $\sim$14 Mpc, which characterizes the zone of motion of the surrounding galaxies toward Coma as an attractor.

Figure 7 shows the data on the masses and K-band luminosities of the galaxies and systems of galaxies collected in Table 2. The circles, triangles, and squares indicate the M/L_K estimates for individual galaxies, groups, and clusters/superclusters, respectively. Dividing the critical density of the Universe $\rho_c = (3H_0^2/8\pi G)$, which is $1.43 \times 10^{11} M_\odot/\text{Mpc}^3$ for $H_0 = 72$ km s^{-1} Mpc^{-1}, by the mean K-band density, j_K, yields a global value of $(M/L_K)_{\rm global}$ that characterizes fairly large (larger than 100 Mpc) volumes of the Universe. Using the above j_K estimates by Kochanek *et al.* (2001) and Bell *et al.* (2003), we obtain $(M/L_K)_{\rm global} = 287$ and $345 M_\odot/L_\odot$, respectively. These values are shown by

the dotted straight lines in the upper right corner of Fig. 7. We took their mean, $(316 \pm 29)M_\odot/L_\odot$, to calibrate the density scale in units of the critical density, which is shown on the right-hand side of the figure.

The horizontal line in the lower part of Fig. 7 indicates the mean stellar mass density, $(0.95 \pm 0.27)M_\odot/L_\odot$, from Bell *et al.* (2003). The other horizontal line corresponds to the mean baryon mass density, $\Omega_\mathrm{b} = 0.047 \pm 0.006$ or $\langle M/L_K\rangle_\mathrm{b} = (14.8 \pm 1.9)M_\odot/L_\odot$, from Spergel *et al.* (2003). The dashed line with a small slope in the lower left corner of the figure indicates the trend of the mean mass (within the standard radius) to luminosity ratio for the Local-Volume galaxies. Analysis of the presented data leads us to several general conclusions.

(1) The density of the stellar mass and gas per unit luminosity is high enough to explain the mean mass-to-luminosity ratio within the standard radius for giant, normal, and dwarf galaxies. It should be borne in mind that the contribution of the gaseous component, which is given by the $M(\mathrm{H\,I})/M_{25}$ ratio, increases with decreasing luminosity of the galaxy, reaching ~1–3 for the smallest dwarf systems (see Fig. 10c from Karachentsev *et al.* 2004).

(2) The passage from visible galaxy regions 1–30 kpc in size to groups dominated by a single galaxy (50–300-kpc scales) is accompanied by an increase in the mass by about an order of magnitude at an almost constant luminosity. The mean M/L_K ratio for groups of galaxies is virtually equal to the mean ratio for the baryon mass, $(14.8 \pm 1.9)M_\odot/L_\odot$.

(3) In the range of IR luminosities from 5×10^{10} to $2 \times 10^{13}L_\odot$, the groups, clusters, and superclusters follow the relation $\log(M/L_K) \propto (0.27 \pm 0.03)\log L_K$ with a characteristic dispersion of ~0.1 comparable to the measurement errors of the total luminosity and mass of the system. The mutual differences between the masses estimated from the virial motions, the X-ray flux, or the lensing prove to be insignificant.

(4) The largest-scale and most populous systems of galaxies, rich clusters/superclusters, are characterized by mass-to-luminosity ratios $M/L_K \sim 50M_\odot/L_\odot$, which accounts for only 16% of the global value of $(M/L_K)_\mathrm{global} = (316 \pm 29)M_\odot/L_\odot$. Since such supersystems include only a small fraction of all galaxies, ~10–20% the mass-to-luminosity ratio averaged over the ensemble of systems of galaxies, $\langle M/L_K\rangle \simeq (20\text{–}25)M_\odot/L_\odot$, is definitely lower than the value of $\langle M/L_K\rangle_m = (80\text{–}90)M_\odot/L_\odot$ expected for the standard cosmological model with $\Omega_m = 0.27$ and $\Omega_\lambda = 0.73$ (Spergel *et al.* 2003). To reconcile the mean matter density averaged over the ensemble of systems of galaxies, $\Omega_{DM} \sim 0.07$, with the global value of $\Omega_m = 0.27$, we must assume that the bulk of the dark matter in the Universe is not associated with galaxies and their systems (Karachentsev 2005).

CONCLUSIONS

The data presented above show that the IR luminosities of nearby galaxies play an important role in studying the dynamical conditions and evolution of systems of galaxies. The all-sky survey in the J, H, K bands and the XSC 2MASS catalog allowed us to investigate the various properties of large galaxy samples in the same photometric system. It is important to determine the IR properties for a distance- rather than flux-limited sample of nearby galaxies. The parameters of such a sample are least affected by various selection effects, which make it difficult to interpret the initial observational data. Unfortunately, only a small fraction (27%) of the 450 Local-Volume galaxies with distances $D < 10$ Mpc is seen in 2MASS due to their low luminosity, surface brightness, or blue color. Therefore, it seems of great importance to measure the J, H, K magnitudes for all northern and southern Local-Volume galaxies to compile a reference photometric sample that could serve as a standard to be compared with deeper samples at various redshifts.

ACKNOWLEDGMENTS

This work was supported in part by the Russian Foundation for Basic Research (project nos. 04-02-16115 and DFG-02-02-04012).

REFERENCES

1. N. A. Bahcall, R. Cen, R. Dave, *et al.*, Astrophys. J. **541**, 1 (2000).
2. E. F. Bell, D. H. McIntosh, N. Katz, *et al.*, Astrophys. J., Suppl. Ser. **149**, 289 (2003).
3. S. Cole, P. Norberg, C. M. Baugh, *et al.*, Mon. Not. R. Astron. Soc. **326**, 255 (2001).
4. R. M. Cutri and M. F. Skrutskie, Bull. Am. Astron. Soc. **30**, 1374 (1998).
5. V. Desai, J. J. Dalcanton, L. Mayer, *et al.*, Mon. Not. R. Astron. Soc. **351**, 265 (2004).
6. H. C. Ferguson, Astron. J. **98**, 367 (1989).
7. M. Fukugita, T. Ichikawa, J. Gunn, *et al.*, Astron. J. **111**, 1748 (1996).
8. R. Gavazzi, Y. Mellier, B. Fort, *et al.*, Astron. Astrophys. **422**, 407 (2004).
9. J. Guzik and U. Seljak, Mon. Not. R. Astron. Soc. **335**, 311 (2002).
10. H. Hoekstra, H. K. Yee, and M. D. Gladders, Astrophys. J. **606**, 67 (2004).
11. T. H. Jarrett, Publ. Astron. Soc. Pac. **112**, 1008 (2000).

12. T. H. Jarrett, T. Chester, R. Cutri, *et al.*, Astron. J. **119**, 2498 (2000).
13. T. H. Jarrett, T. Chester, R. Cutri, *et al.*, Astron. J. **125**, 525 (2003).
14. H. Jerjen, Astron. Astrophys. **398**, 63 (2003).
15. C. Jones, C. Stern, W. Forman, *et al.*, Astrophys. J. **482**, 143 (1997).
16. I. D. Karachentsev, Astrofiz. **2**, 81 (1966).
17. I. D. Karachentsev, Astron. J. **129** (1) (2005).
18. I. D. Karachentsev and E. V. Karachentseva, Astron. Zh. **81**, 298 (2004) [Astron. Rep. **48**, 267 (2004)].
19. I. D. Karachentsev, V. E. Karachentseva, W. K. Huchtmeier, *et al.*, Astron. J. **127**, 2031 (2004).
20. I. D. Karachentsev, S. N. Mitronova, V. E. Karachentseva, *et al.*, Astron. Astrophys. **396**, 431 (2002).
21. I. D. Karachentsev, M. E. Sharina, and W. K. Huchtmeier, Astron. Astrophys. **362**, 544 (2000).
22. J. P. Kneib, P. Hudelot, R. S. Ellis, *et al.*, Astrophys. J. **598**, 804 (2003).
23. C. S. Kochanek, M. A. Pahre, E. E. Falco, *et al.*, Astrophys. J. **560**, 566 (2001).
24. Y. T. Lin, J. J. Mohr, and S. A. Stanford, Astrophys. J. **582**, 574 (2003).
25. M. Loewenstein and R. Mushotzky, astro-ph/0208090 (2002).
26. D. I. Makarov, I. D. Karachentsev, and A. N. Burenkov, Astron. Astrophys. **405**, 951 (2003).
27. D. E. McLaughlin, Astrophys. J. Lett. **512**, L9 (1999).
28. E. W. Peng, H. C. Ford, and K. C. Freeman, Astrophys. J. **602**, 685 (2004).
29. M. Persic and P. Salucci, Mon. Not. R. Astron. Soc. **258**, 14 (1992).
30. K. Rines, M. J. Geller, M. J. Kurtz, *et al.*, Astrophys. J. Lett. **561**, L41 (2001).
31. D. J. Schlegel, D. P. Finkbeiner, and M. Davis, Astrophys. J. **500**, 525 (1998).
32. D. N. Spergel, L. Verde, H. V. Peiris, *et al.*, Astrophys. J., Suppl. Ser. **148**, 175 (2003).
33. J. L. Tonry, J. P. Blakeslee, E. A. Ajhar, *et al.*, Astrophys. J. **530**, 625 (2000).
34. J. L. Tonry, A. Dressler, J. P. Blakeslee, *et al.*, Astrophys. J. **546**, 681 (2001).
35. R. B. Tully and E. J. Shaya, Astrophys. J. **281**, 31 (1984).

Translated by A. Dambis

Astronomy Letters, Vol. 31, No. 5, 2005, pp. 308–314. Translated from Pis'ma v Astronomicheskiĭ Zhurnal, Vol. 31, No. 5, 2005, pp. 342–349.

Numerical Simulations of the Hyades Dynamics and the Nature of the Moving Hyades Cluster

Ya. O. Chumak[1*], A. S. Rastorguev[1,2], and S. J. Aarseth[3]

[1] *Moscow State University, Vorob'evy gory, Moscow, 119992 Russia*

[2] *Sternberg Astronomical Institute, Universitetskiĭ pr. 13, Moscow, 119992 Russia*

[3] *Institute of Astronomy, Cambridge University, Madingley Road, Cambridge CB3 0HA, England, UK*

Received December 14, 2004

Abstract—We present our numerical simulations of the dynamical evolution of the Hyades open cluster. The simulations were performed using a modified NBODY6 algorithm that included tidal forces and a realistic orbit of the cluster in a gravitational field described by the Miyamoto–Nagai potential. Our goal was to study the nature of moving clusters. We show that the stars that were earlier cluster members could be later identified within a sphere of 50 pc in diameter around the Sun. The number of such stars for the chosen initial mass and virial radius of the cluster does not exceed ten. The maximum space velocity of these stars relative to the core of the current cluster does not exceed 3 km s^{-1}. Our numerical simulations confirm the assumption that some of the moving clusters near the Sun could consist of stars that have escaped from open clusters in the course of their dynamical evolution. © *2005 Pleiades Publishing, Inc.*

Key words: *N-body simulations, moving clusters, dynamical evolution, Hyades open cluster.*

INTRODUCTION

Our goal was to test the hypothesis about the formation of moving clusters of stars that escaped through the breakup of open star clusters using the Hyades as an example. We performed numerical simulations using a modified NBODY6 code (Aarseth 2003).

Investigating Moving Clusters

The term "moving clusters" first appeared in the 19th century. At this time, Bessel (1841) determined the proper motions of many stars for the first time. A comparison the stellar coordinates determined by Bessel with Bradley's observations performed in the 18th century made this possible. Bessel was the first to notice that the motions of Pleiades stars are similar. Subsequently, while analyzing the proper motions of stars, Proctor (1872) found that five bright stars of the Big Dipper in Ursa Major move almost identically. Thus, Proctor proved that these stars form a single system, a moving cluster.

Hertzsprung (1909) found the proper motion of Sirius, 2.5 pc away, to be surprisingly similar to the proper motion of the Ursae Majoris cluster stars. Hertzsprung was the first to show that the sizes of moving clusters could reach dozens of parsecs. Many researchers have searched for and continue to search for groups of stars with similar space velocities in the solar neighborhood, irrespective of the separations between the stars, since that time.

However, as Eddington (1914) pointed out, such a close similarity between the stellar velocities could be coincidental, and a good statistical analysis of the structure of the stellar space velocity field is required to reach a conclusion about the reality of these stellar groupings.

When the astrometric data and the stellar space velocities were refined, some of the moving clusters proved to be illusory. Thus, for example, having determined the coordinates of the points of convergence of the proper motions and the space velocities of stars, Rasmuson (1921) concluded that several moving clusters are illusory, thereby proving that the commonness of their velocities just reflects the solar motion in space.

In the 1950s, Eggen (1958, 1965) began a systematic study of moving clusters. He investigated previously discovered groups, starting from the classical Hyades, Sirius, and Ursae Majoris groups. Studying the stars belonging to the Hyades moving group, Eggen also included the Praesepe cluster, which moves with a space velocity close to the Hyades

*E-mail: chyo@mail.ru

1063-7737/05/3105-0308$26.00

velocity, in this group. Eggen investigated both well-known and new stellar groups. He identified about two dozen stellar groups by considering not only the similarity of the stellar space velocities as a commonness criterion, but also an additional criterion, the [Fe/H] ratio.

Eggen showed that the differences between the motions of group members in the direction perpendicular to the Galactic plane (the W velocity components) can be ignored when identifying the members of moving groups by the U and V velocity components. The W velocity dispersion for a group depends not only on the initial velocity dispersion, but also on the sizes of the initial cloud and its location relative to the Galactic plane, since, as can be easily shown, the frequency of the stellar oscillations in z coordinate is much higher than the angular frequency of the disk and the epicyclic frequency. Therefore, in identifying the members of moving clusters, Eggen proposed ignoring the W velocity components and taking into consideration only the similarity of the U and V components. Using these selection criteria, Eggen managed to identify about two dozen moving clusters known in the literature as Eggen's groups.

Agekyan and Belozerova (1979) showed that during the evolution of an open cluster, the stars that escaped from the cluster form a huge halo around it. The halo stars have similar space velocities and actually form a moving cluster. Although the halo as well as the core of the cluster are rapidly dispersed in space under external factors (differential rotation and tidal forces), the halo stars can retain their similar space velocities long after the cluster breakup. Thus, the entire Galactic disk can be imagined as an interpenetrating system of moving clusters. However, as was pointed out by Kholopov (1981), this hypothesis is applicable only to moving clusters whose members have similar space velocities and does not account for the existence of Eggen's stellar groups.

In one of the papers on the identification of moving clusters in the solar neighborhood (Orlov *et al.* 1995), the authors used the Catalogue of Nearby Stars by Gliese and Jahreiss (1991) as a data source. The Catalogue by Gliese and Jahreiss numbered 1947 single and multiple stars with measured space velocities at that time. Data on stars within $R = 25$ pc of the Sun were used in the paper. Using the centroid version of the hierarchical clustering method in velocity space, the authors managed to reliably identify five moving clusters with a space velocity difference of no more than 6 km s^{-1} from the central value with ~30–40 members. In particular, the identification of a Hyades cluster group that numbers 31 stars was confirmed.

The Hyades Open Cluster

The Hyades cluster played a major role in the history of developing the methods of stellar astronomy. Before the completion of the Hipparcos Space Mission (ESA 1997), the distance scale of open clusters (and, hence, Cepheids) was actually based on only one star cluster, the Hyades. The fairly short distance to the Hyades and its high space velocity relative to the Sun had been the reasons for this unique role of the cluster for many years. This allowed the method of group parallaxes, a reliable direct method of distance measurements, to be applied to this cluster (Kulikovskiĭ 1985).

It is safe to say that the Hyades is one of the best studied open clusters. A large number of works are devoted to the determination of particular cluster parameters. The most recent and comprehensive study of its characteristics was performed by Perryman *et al.* (1998). These authors gave a complete bibliography of papers on this subject. To determine the distances of individual stars, the authors used Hipparcos trigonometric parallaxes, thereby deriving a three-dimensional structure of the cluster. Hipparcos parallaxes and proper motions as well as radial velocities were used to identify cluster members. Thirteen new candidate cluster members were identified within 20 pc of the cluster center, while simple estimates of the tidal radii for open clusters of such a mass in the solar neighborhood yield 8–10 pc (Rastorguev 2003). The space velocity vectors of the cluster stars were shown to have a dispersion of ~0.3 km s^{-1}. The age of the cluster was estimated to be 625 ± 50 Myr. The distance to the center of mass of the cluster (taking into consideration only Hipparcos data) was estimated to be 46.3 ± 0.3 pc, which corresponds to the true distance modulus $(m - M) = 3^m.23$. The authors determined the shape of the cluster with a cluster core axial ratio of 1.6 : 1.2 : 1; stars within 20 pc were taken into account. The major axis is inclined to the X axis, which is directed toward the Galactic center at an angle of about 16 degrees; thus, the ellipsoid of the cluster is oriented almost exactly along the principal Galactic directions. The half-mass radius and the total mass were estimated to be $r_h = 5.7$ pc and $400 M_\odot$ solar masses, respectively. In our opinion, these structure–mass characteristics of the Hyades are currently most complete and reliable. Below, these were used for comparison with our simulations.

We used the well-known NBODY6 numerical simulation code (Aarseth 2003) to simulate the dynamical evolution of the Hyades star cluster; this code has gained recognition worldwide and is commonly used to simulate the dynamic evolution of star clusters. Aarseth's algorithm reproduces most faithfully the actual physical processes in stellar systems. Not

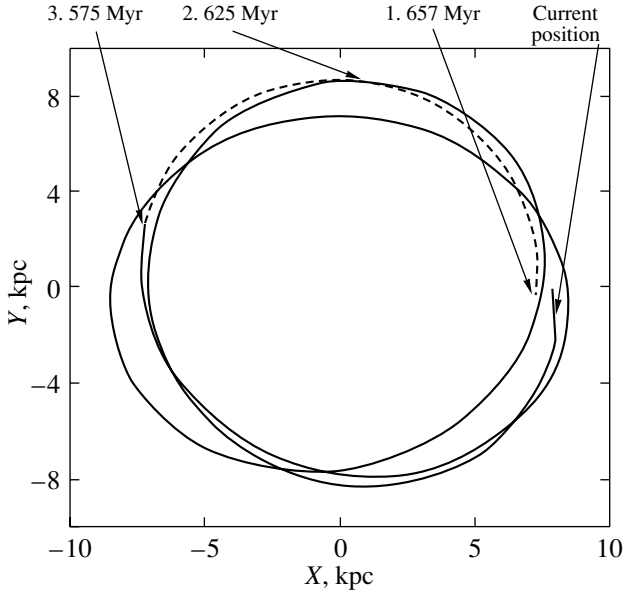

Fig. 1. Orbit of the Hyades. The positions of the cluster at different times used as the initial integration conditions are marked.

only close encounters between stars and the related mass loss by the cluster, but also the external tidal field, the interaction of the cluster with molecular clouds, and the physical evolution of cluster members are taken into account in simulations. The dynamics of binary, triple, and multiple systems is computed in the code separately and more accurately. A description of the algorithm and its various implementations in the NBODY1-6 codes can be found in the papers by Aarseth (1973, 1977, 1999). The most complete description of the code and its capabilities can be found in a new book by Aarseth (2003).

The NBODY6 code and previous implementations of Aarseth's algorithm have been repeatedly used to numerically simulate the evolution of the Hyades. Thus, for example, Oort (1979) attempted to detect a flattening of the core in the direction perpendicular to the Galactic disk by comparing the observational data with the simulations of Aarseth (1973). Aarseth (1992) studied the influence of binary stars on the evolution rate of the cluster by numerical simulations. Kroupa (1995) found good agreement between the luminosity functions of the Hyades and the simulated cluster. In this way, he chose initial simulation conditions by estimating the initial mass of the Hyades to be $1300 M_\odot$. Von Hippel (1998) studied the influence of a population of white dwarfs on the evolution of the cluster by numerical simulations. Portigies Zwart *et al.* 2001 found initial conditions for simulations of several open clusters, including the Hyades. Madsen (2003) analyzed the kinematics of the Hyades core by comparing Hipparcos observational data with NBODY6 simulations.

NUMERICAL SIMULATIONS OF THE HYADES

Initial Conditions and Simulation Parameters

Using the NBODY6 code, we numerically simulated the dynamical evolution of the Hyades open cluster in the Galactic tidal field. Let us describe the chosen initial conditions for our computations.

The positions and masses of the stars were specified using a random number generator in accordance with the specified density distribution and the adopted mass function. Plummer's distribution (Plummer 1915; Spitzer 1987) was used as the initial density distribution. The initial mass function was taken from the paper by Kroupa *et al.* (1993). The initial equilibrium value of $Q = 0.5$ was taken for the virial coefficient. The initial virial radius R_v is a free simulation parameters.

The three-dimensional analytical model of the Galactic potential by Miyamoto and Nagai (1975) was used to compute the orbit of the cluster and the external tidal perturbation. In contrast to previous works in which a circular orbit of the cluster around the Galactic center with a constant angular velocity, $\Omega = 26.4$ km s^{-1} kpc^{-1}, was assumed (Madsen 2003), we simulated the stellar evolution of the Hyades with the NBODY6 code for the more realistic case of motion along an eccentric orbit. Accordingly, the structure of the tidal force field is also more complex and changes with time.

The simulation time interval was taken to be equal to the age of the Hyades, which is 625 ± 50 Myr (Perryman *et al.* 1998). To find the initial position of the Hyades in the Galaxy near the time of its formation and the initial velocity vector of the cluster, it was necessary to reconstruct the orbit of the cluster. For this purpose, we computed the orbits of the cluster and the Sun in the past. The current relative positions and the total space velocities of the Hyades and the Sun (including the sense of Galactic rotation) served as the initial conditions. The dynamic evolution of the cluster was simulated over a time interval close to its age, 675 Myr, taking into account the uncertainty of its determination. Thus, for the times of 575, 625, and 675 Myr ago, we found the Galactic coordinates and velocity components of the cluster, which were subsequently used as the initial simulation conditions for the Hyades orbit.

Figure 1 shows a projection of the reconstructed Hyades orbit onto the Galactic XY plane. Over its lifetime, the cluster has made about three turns around the Galactic center. The part of the orbit

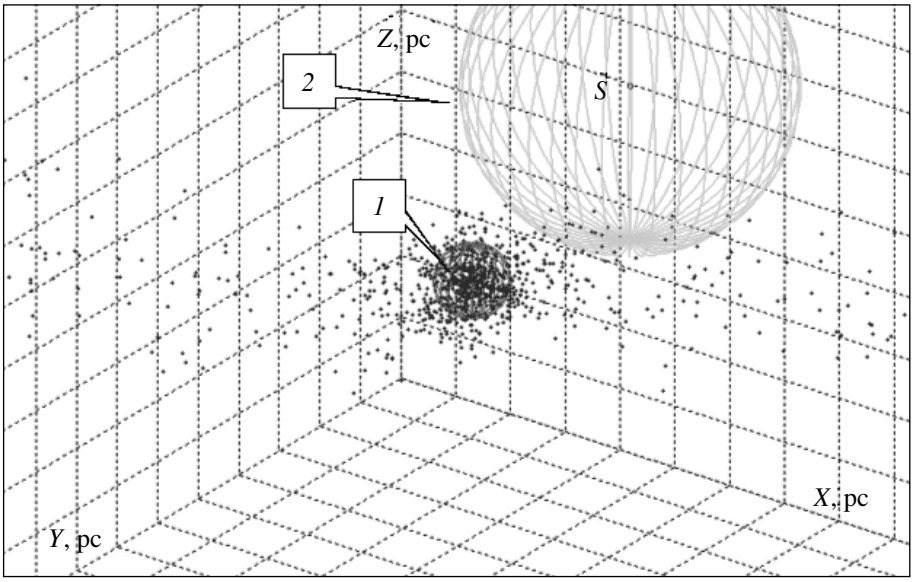

Fig. 2. Final simulation picture in the *XYZ* coordinate system. Sphere *1* is the cluster core, and sphere *2* is the solar neighborhood within 25 pc.

from −675 to −575 Myr is indicated by the dashed line. This segment of the orbit corresponds to the uncertainty in the cluster formation time.

The NBODY6 code can work in two different modes, with and without the recession of stars, when computing the stars that went beyond twice the virial radius of the cluster. We traced the dynamics of the stars escaped from the cluster, since one of our goals was to study the moving groups whose origin is associated with the breakup of open clusters. Therefore, we actually traced the individual orbits of the stars escaped from the cluster. However, the original version of the code did not envisage this possibility for a fairly long integration time. Therefore, we made changes to the computational algorithm. In the tracing mode, the integration of the equations of motion for the escaped stars continues, but with the inclusion of only the external Galactic field. The forces exerted on these stars from cluster members were disregarded. These changes gave rise to several new modules of the NBODY6 code and to a partial modification of the existing modules.

The observed number of binary stars in open clusters is known to be difficult to explain solely by the formation of binaries in triple or multiple encounters between stars during the dynamical evolution. Their number can be explained only by the presence of primordial binaries, i.e., binary stars formed during the cluster fragmentation from a protostellar cloud. In addition, as Aarseth (1992) showed, the presence of primordial binaries in a cluster can affect significantly the pattern of its dynamical evolution. Therefore, great attention is devoted to the presence of a primordial population of binary stars in some of the works on the numerical simulation of the dynamical evolution of clusters. Different authors assume different fractions of primordial binaries in the total number of stars. Thus, for example, Portigies Zwart *et al.* (2001), Kroupa (1995), and Madsen (2003) assumed that $F_{\rm bin} = 50$, 100, and 86%, respectively. There are papers in which primordial binaries are completely disregarded (see, e.g., Terlevich 1987). Here, we do not set the goal of studying the influence of primordial binaries of the pattern of evolution of the cluster, since this question has already been widely discussed in the papers listed above. Accordingly, we took 20% for the binary fraction $F_{\rm bin}$ based on the results of Aarseth (1992) to make the simulations most realistic.

The NBODY6 code allows us to consider the physical evolution of stars whose main dynamical effect is the escape of stars due to an asymmetric kick during supernova explosions. The algorithm of allowance for stellar evolution is described in detail in the book by Aarseth (2003). Since the simulation time is long enough (about 600 Myr), this effect can affect the dynamical evolution of the cluster. For this reason, it was included in our simulations.

The Simulation Technique

As an example, Fig. 2 shows the spatial distribution of stars at the final stage of our numerical simulations in a rectangular XYZ coordinate system in which the X axis is directed away from the Galactic center, the Y axis lies in the plane of the Galactic

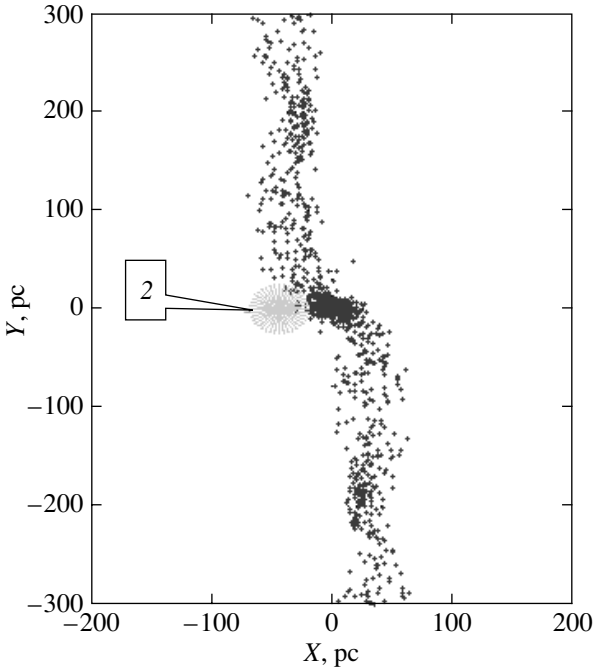

Fig. 3. Projection of the final simulation picture onto the XY plane. The cluster core lies at the coordinate origin. Sphere *2* is the solar neighborhood within 25 pc.

disk and is directed in the sense of Galactic rotation, and the Z axis is directed toward the Galactic north pole. The coordinate origin coincides with the center of mass of the cluster core. The dots indicate the stars that still belong to the Hyades and those that have gone beyond the tidal radius of the cluster. Sphere *1* around the cluster center has a radius of 10.3 pc, which corresponds to the tidal radius of the current Hyades (Perryman 1998).

Knowing the current distance and coordinates of the Hyades center of mass, we can easily determine the position of the Sun in this coordinate system. According to Perryman *et al.* (1998), the coordinates of the Sun are $X = -43.1$ pc, $Y = -0.3$ pc, and $Z = 17.1$ pc. The position of the Sun in Fig. 2 is marked by the letter S. Sphere *2* around the Sun has a radius of 25 pc. In the sphere of this radius, Orlov *et al.* (1995) detected 31 stars that presumably belong to the moving Hyades cluster. We see from the figure that some of the stars that have escaped from the Hyades fall into this sphere.

Figure 3 shows a projection of the spatial positions of Hyades stars onto the XY plane in the rectangular XYZ coordinate system associated with the cluster. Figure 3 is a projection of Fig. 2 on a smaller scale.

As we see from the figure, a central region with an enhanced concentration of stars and two stellar "tails" elongated along the Y axis, i.e., in the sense of orbital rotation, and slightly bent can be identified. The dense central region is the current cluster core, and the stellar tails consists of the stars that escaped from the cluster at various stages of its evolution and that still accompany it as they move in the orbit.

RESULTS

The initial conditions described in the Section "Initial Conditions and Simulation Parameters" were rigidly specified for the entire series of our numerical simulations. The initial mass M_0 and the initial virial radius R_v were taken as free parameters. The radius R_v varied over the range from 1 to 7.5 pc, while the initial mass varied over the range from 600 to $1700 M_\odot$.

To estimate the true values of M_0 and R_v, we performed a series of numerical simulations with various combinations of these parameters. We assumed that, to be consistent with the actual observational data for the Hyades, the parameters M_0 and R_v must be chosen in such a way that the stars whose total mass is close to the current mass of the Hyades core fall into the central region of the core. According to Perryman *et al.* (1998), the Hyades mass is about $400 M_\odot$ within a radius of 10.3 pc. It should be noted that the estimates by other authors are similar to Perryman's estimate. Thus, for example, Madsen (2003) estimated the Hyades mass to be $460 M_\odot$, while Reid (1993) gave an estimate of 410–480 $M_\odot$.

In Fig. 4, the final mass of the cluster core obtained through our simulations, M_C, is plotted against the initial mass of the entire cluster, M_0, for various initial virial radii R_v. We clearly see that the dependence of the final cluster core mass on the initial mass for the chosen initial virial radius is nearly linear. We also clearly see that for each present initial virial radius, the initial mass M_0 can be chosen in such a way that the resulting cluster core mass M_C agrees with the current value. The results of our calculations for cases 1–3 are similar.

To investigate the formed simulated moving cluster, we considered the solar neighborhood, sphere *2*. If the velocity dispersion of the stars that escaped from the cluster and fell into this sphere does not exceed the value of the criterion for the similarity between the space velocities used in the papers on the identification of moving cluster members (see. e.g., Orlov *et al.* 1995), then this could serve as an important argument for the hypothesis about the origin of moving clusters under consideration.

As a result of more than 30 numerical simulations, it became clear that in all of the simulations that satisfied the final core mass criterion described above, a certain number of stars actually fall into sphere *2*. Their number varies between 1 and 11. This can serve as an argument that there are actually stars among

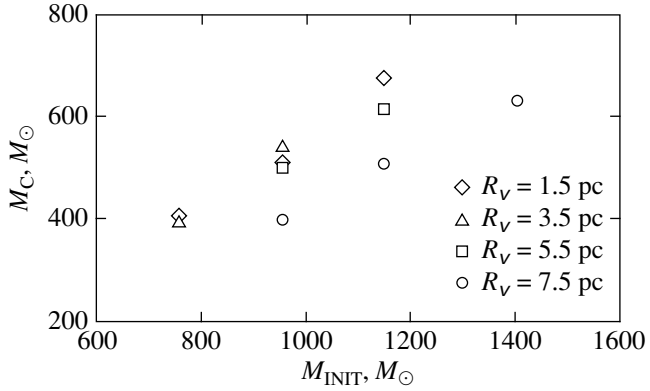

Fig. 4. Current mass of the Hyades core M_C versus initial mass M_{INIT} for various initial virial radii R_v. The results are almost identical for virial radii within the range 1.5–5.5 pc.

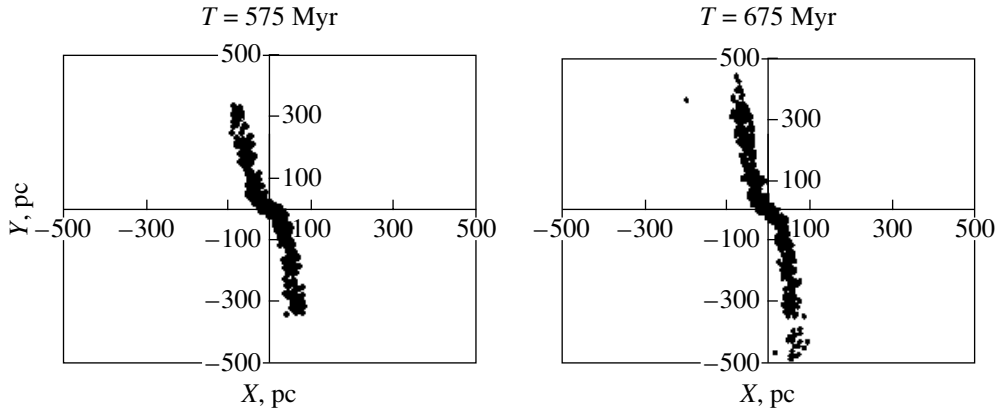

Fig. 5. Projections of the final configurations for simulations times of $T = 575$ and 675 Myr onto the XY plane. The cluster core is at the coordinate origin.

the members of the moving Hyades cluster that have previously belonged to the Hyades. Their number is relatively small, on average, 5 to 7 stars as inferred from all our simulations. Their masses lie within the range from 0.3 to $2M_\odot$. The mean and maximum "distances" in velocity space from the velocity vector of the cluster core are 1.4 and 3 km s^{-1}. Note also that binary stars fell into sphere *2* in several cases.

We performed a series of simulations with $T = 575$ and 675 Myr. The results obtained are compared in Fig. 5.

We see from the figure that the lengths of the stellar tails change over a period of 100 Myr, but the overall picture remains unchanged. During this period, the stars continue to escape from the cluster core, passing into the tails, while the tails themselves continue to stretch along the cluster motion. The core mass over a period of ∼100 Myr for a cluster with an initial mass of $1000M_\odot$ solar masses and an initial virial radius of $R_V = 3.5$ pc decreases by about $50M_\odot$. However, the thickness of the tails remains virtually unchanged. Accordingly, the number of stars in sphere *2* does not change either.

CONCLUSIONS

Our numerical simulations have revealed that the stars that have previously belonged to the Hyades and escaped from this cluster during its dynamical evolution can be observed in the solar neighborhood. The maximum space velocity of these stars relative to the cluster core is $C = 3$ km s^{-1}. This value of C suggests that the moving clusters can actually be formed from the stars that escaped from certain open clusters. Since the method of identifying moving clusters used by Orlov *et al.* (1995) is actually based on a comparison of the stellar space velocities in the solar neighborhood with the velocity of the cluster itself, the derived distance C should be taken into account when choosing the maximum space velocity difference used to identify the members of moving clusters. In our opinion, choosing a value of the velocity similarity criterion lower than that in the paper by Orlov *et*

al. (1995) would lead to a decrease in the number of potential members of the moving Hyades cluster and to an improvement of the agreement with our numerical simulations.

In addition, other factors, such as the errors in the radial velocities and proper motions of the stars, should also be considered when choosing C.

ACKNOWLEDGMENTS

This work was supported in part by the Russian Foundation for Basic Research (project no. 02-02-16667) and a Presidential grant for Support of Leading Scientific Schools (no. NSh-389-2003-2).

REFERENCES

1. S. J. Aarseth, Vistas Astron. **15**, 13 (1973).
2. S. J. Aarseth, Rev. Mex. Astron. Astrofis. **3**, 199 (1977).
3. S. J. Aarseth, Publ. Astron. Soc. Pac. **111**, 1333 (1999).
4. S. J. Aarseth, *Gravitational N-Body Simulations* (Cambridge Univ. Press, Cambridge, 2003).
5. S. J. Aarseth, Mon. Not. R. Astron. Soc. **257**, 513 (1992).
6. T. A. Agekyan and M. A. Belozerova, Astron. Zh. **56**, 9 (1979) [Sov. Artson. **23**, 4 (1979)].
7. F. W. Bessel, Konigsberg: Im Verlage der Gebruder Bortrager **1**, 209 (1841).
8. O. J. Eggen, Mon. Not. R. Astron. Soc. **118**, 65 (1958).
9. O. J. Eggen, *Stars and Stellar Systems* (Chicago Univ. Press, London, 1965).
10. A. S. Eddington, *Stellar Movements and the Structure of the Universe* (Mac Millan and Co., London, 1914), Vol. 12, p. 266.
11. ESA, The HIPPARCOS and TYCHO Catalogues, ESA SP-1200 (ESA, Nordwijk, 1997).
12. W. Gliese and H. Jahreiss, *Preliminary Version of the Third Catalogue of Nearby Stars. The Astronomical Data Center CD-ROM: Selected Astronomical Catalogs,* Ed. by L. E. Brotzmann and S. E. Gesser, NASA/Astronomical Data Center, Goddard Space Flight Center, Greenbelt, MD (1991), Vol. 1.
13. E. Hertzsprung, Astrophys. J. **30**, 135 (1909).
14. P. N. Kholopov, *Star Clusters* (Nauka, Moscow, 1981).
15. P. Kroupa, Mon. Not. R. Astron. Soc. **277**, 1522 (1995).
16. P. Kroupa, C. Tout, and G. Gilmore, Mon. Not. R. Astron. Soc. **262**, 545 (1993).
17. P. G. Kulikovskiĭ, *Stellar Astronomy* (Nauka, Moscow, 1985), p. 272.
18. S. Madsen, Astron. Astrophys. **401**, 565 (2003).
19. M. Miyamoto and R. Nagai, Publ. Astron. Soc. Jpn. **27**, 533 (1975).
20. J. H. Oort, Astron. Astrophys. **78**, 312 (1979).
21. V. V. Orlov, I. E. Panchenko, A. S. Rastorguev, and A. V. Yatseich, Astron. Zh. **72**, 495 (1995) [Astron. Rep. **39**, 437 (1995)].
22. M. A. C. Perryman, A. G. A. Brown, Y. Lebreton, *et al.*, Astron. Astrophys. **331**, 81 (1998).
23. H. C. Plummer, Mon. Not. R. Astron. Soc. **76**, 107 (1915).
24. S. F. Portigies Zwart, S. L. W. McMillan, P. Hut, and J. Makino, Mon. Not. R. Astron. Soc. **321**, 199 (2001).
25. R. A. Proctor, Mon. Not. R. Astron. Soc. **33**, 105 (1872).
26. N. H. Rasmuson, Medd. Lunds Astron. Observ. **26**, 62 (1921).
27. A. S. Rastorguev, *Abstract of Lectures "Elements of Dynamics of Stellar Systems"* (Gos. Astron. Inst. Shternberga, Mosk. Gos. Univ., Moscow, 2003).
28. I. N. Reid, Mon. Not. R. Astron. Soc. **265**, 785 (1993).
29. L. Spitzer, *Dynamical Evolution of Globular Clusters* (Princeton Univ. Press, Princeton, 1987).
30. E. Terlevich, Mon. Not. R. Astron. Soc. **224**, 193 (1987).
31. T. von Hippel, Astron. J. **115**, 1536 (1998).

Translated by V. Astakhov

Astronomy Letters, Vol. 31, No. 5, 2005, pp. 315–326. Translated from Pis'ma v Astronomicheskiĭ Zhurnal, Vol. 31, No. 5, 2005, pp. 350–362.

Flares of the H_2O Maser in W31(2)

E. E. Lekht[1*], V. A. Munitsyn[2], and A. M. Tolmachev[3]

[1] *Instituto Nacional de Astrofísica, Óptica y Electrónica, Luis Enrique Erro No. 1, Apdo Postal 51 y 216, 72840 Tonantzintla, Puebla, México*

[2] *Space Research Institute, Russian Academy of Sciences, Profsoyuznaya ul. 84/32, Moscow, 117997 Russia*

[3] *Pushchino Radio Astronomy Observatory, Astrospace Center, Lebedev Physical Institute, Russian Academy of Sciences, Pushchino, Moscow oblast, 142292 Russia*

Received October 4, 2004

Abstract—We analyze our monitoring data for the water-vapor maser in the source W31(2), associated with a region of vigorous star formation, a cluster of OB stars. The monitoring was performed with the 22-m radio telescope at Pushchino Radio Astronomy Observatory during 1981–2004. The variability of the H_2O maser in W31(2) was found to be cyclic, with a mean period of 1.9 yr. Two flares were most intense (superflares): in 1985–1986 and 1998–1999. In each activity cycle, we observed up to several short flares, subpeaks. The fluxes of many emission features during the flares were correlated. We also observed successive activation of individual emission features in order of increasing or decreasing radial velocity, suggesting an ordered structure and, hence, a radial-velocity gradient of the medium. There is a clear correlation of the emission peaks of the main components in the spectra at radial velocities of -1.7, -1.3, 0.5, and 1.3 km s^{-1} with activity cycles and of the emission at $V_{\rm LSR} < -8$ km s^{-1} with short flares. During the superflares, the emission in the low-velocity part of the H_2O spectrum and a number of other phenomena related to coherent maser-emission properties were suppressed. The maser spots are assumed to form a compact structure, to have a common pumping source, and to be associated with an accretion flow onto the cluster of OB stars. © *2005 Pleiades Publishing, Inc.*

Key words: *star formation, water-vapor maser emission.*

INTRODUCTION

The H_2O maser source W31(2) is associated with the region of vigorous star formation, which is located near the center of our Galaxy and has a complex structure (Ho and Haschick 1981; Ho *et al.* 1986). The infrared source IRS7 lies at the center of this region (Wright *et al.* 1977). A collapsing molecular core with rotation (Ho and Haschick 1986; Keto *et al.* 1987) is taken as a model of the source. A cluster of forming massive OB stars is located inside the core (Ho *et al.* 1986). The core is embedded within a slowly rotating envelope with a velocity gradient of $\sim$1 km s^{-1} pc^{-1}. The fragments of the core with a redshift of $\sim$5 km s^{-1} relative to its centroid could be the regions that collapse toward the OB stars. Some of the maser spots may be associated with these fragments (Lekht *et al.* 2004). This association can strongly affect the parameters of the H_2O maser emission and the pattern of its variability.

In this paper, based on our 1981–2004 monitoring data (Lekht *et al.* 2004), we investigate the flaring activity of the H_2O maser emission in W31(2).

OBSERVATIONS AND DATA PRESENTATION

The H_2O maser source W31(2) ($\alpha_{1950} = 18^{\rm h}07^{\rm m}30\overset{\rm s}{.}3$, $\delta_{1950} = -19°56'38''$) was monitored in the 1.35-cm line with the 22-m RT-22 radio telescope at Pushchino Radio Astronomy Observatory. The monitoring was performed in the period 1981–2004. The spectral resolution was 0.101 km s^{-1}.

A system of highly stable heterodyne frequencies ensured its relative instability of $\pm 1.7 \times 10^{-8}$, which is ± 0.005 km s^{-1} for $\lambda = 1.35$ cm. In observations with a spectral resolution of 0.1 km s^{-1}, the maximum fluctuations of the line velocity did not exceed 0.1 of the width of one spectral channel due to the heterodyne frequency instability. The possible random errors in the heterodyne frequency in each series of observations were revealed by the set of observations of all the sources from our long-term monitoring program that exhibited intense emission features at that time.

The radio telescope was aligned in each series of observations using strong maser sources. In addition, as necessary, the position of the radio telescope was additionally refined in each series, particularly

*E-mail: lekht@inaoep.mx

1063-7737/05/3105-0315$26.00

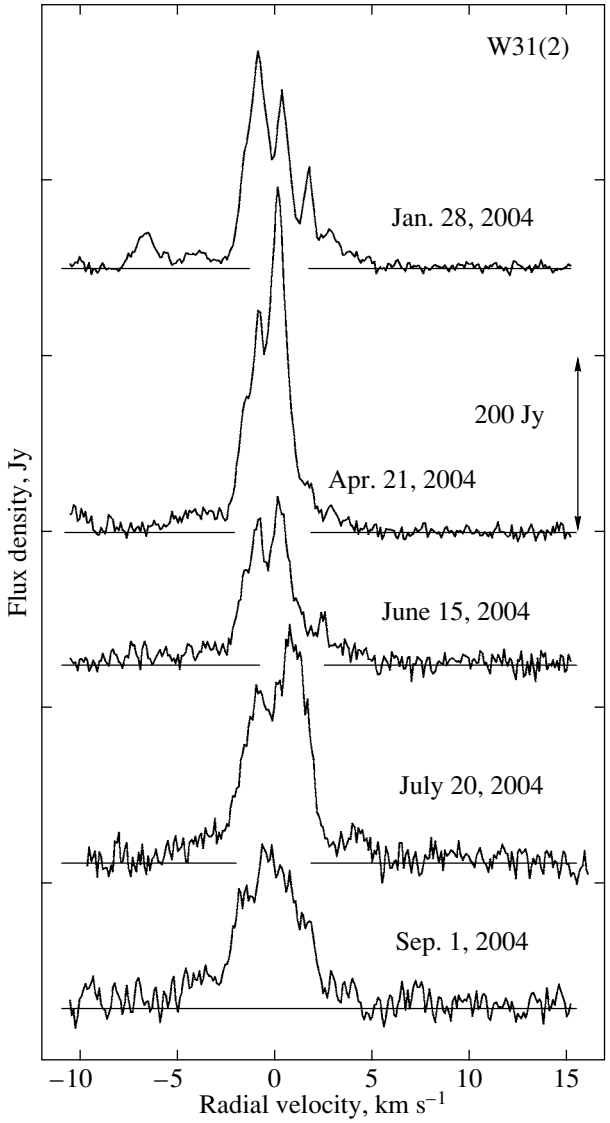

Fig. 1. H_2O spectra toward W31(2) in 2004.

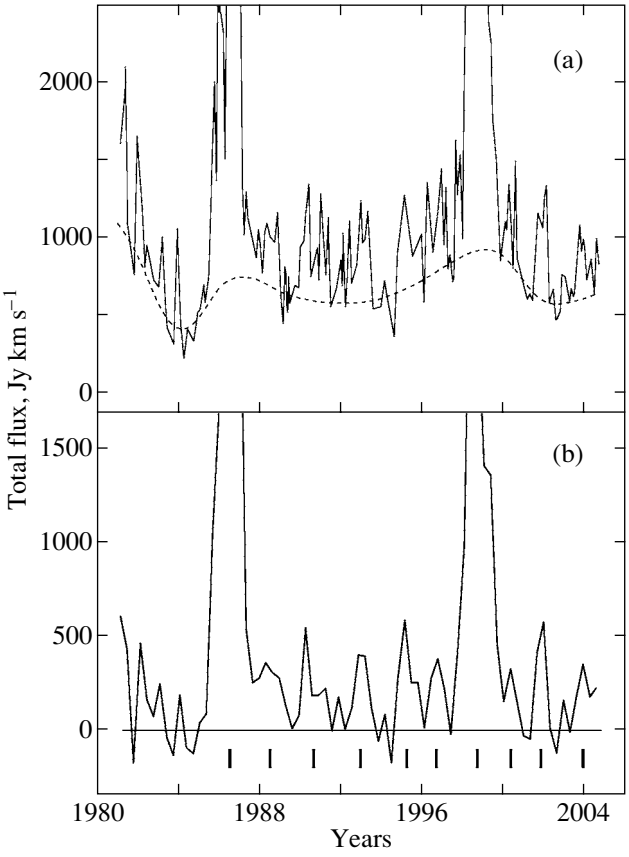

Fig. 2. (a) Variability of the total H_2O flux toward W31(2); (b) the same as panel (a), but after the subtraction of the dashed line and the smoothing; the dashed line represents the smooth fitting curve that reflects slow flux variations, and the bars at the bottom indicate the positions of the peaks.

in summer during the daytime, when the dish was nonuniformly heated by the Sun.

A complete catalog of H_2O spectra for the period 1981–2003 and some of our monitoring results were published previously (Lekht *et al.* 2004). All H_2O spectra were corrected for the absorption of emission in the Earth's atmosphere.

Figure 1 presents H_2O spectra for 2004. Figure 2a shows a plot of the total flux variability from our previous paper (Lekht *et al.* 2004), but in modified form. In addition, we added data for January–August 2004. The dashed line represents the fitting curve that reflects slow flux variations. In Fig. 2b, the total flux variability is shown after the subtraction of the dashed line and the smoothing of the residual curve. We clearly see a cyclic pattern of total flux variability with a time scale of 1.5–2.5 yr. The vertical bars at the bottom indicate the positions of the peaks.

The interval 1981–1984 was more complex—we failed to distinguish any cycles of maser activity. For this reason, we divided this interval into two segments: the periods of maximum and minimum activity. June 1983 was chosen as the dividing line. For all of the time intervals reflecting the cyclic H_2O maser activity and for the first two intervals, we constructed average spectra. The results are presented in Fig. 3. The horizontal bars indicate the zero levels of the average spectra. The dotted line represents the average spectrum for the stable and prolonged minimum observed during 1989.

To analyze the pattern of flux variability in the period 1981–1983 and the two strongest flares (superflares) occurred in 1985–1986 and 1998–1999, we decomposed the central parts of the spectra (from −4 to 5 km s^{-1}) into individual components (emission

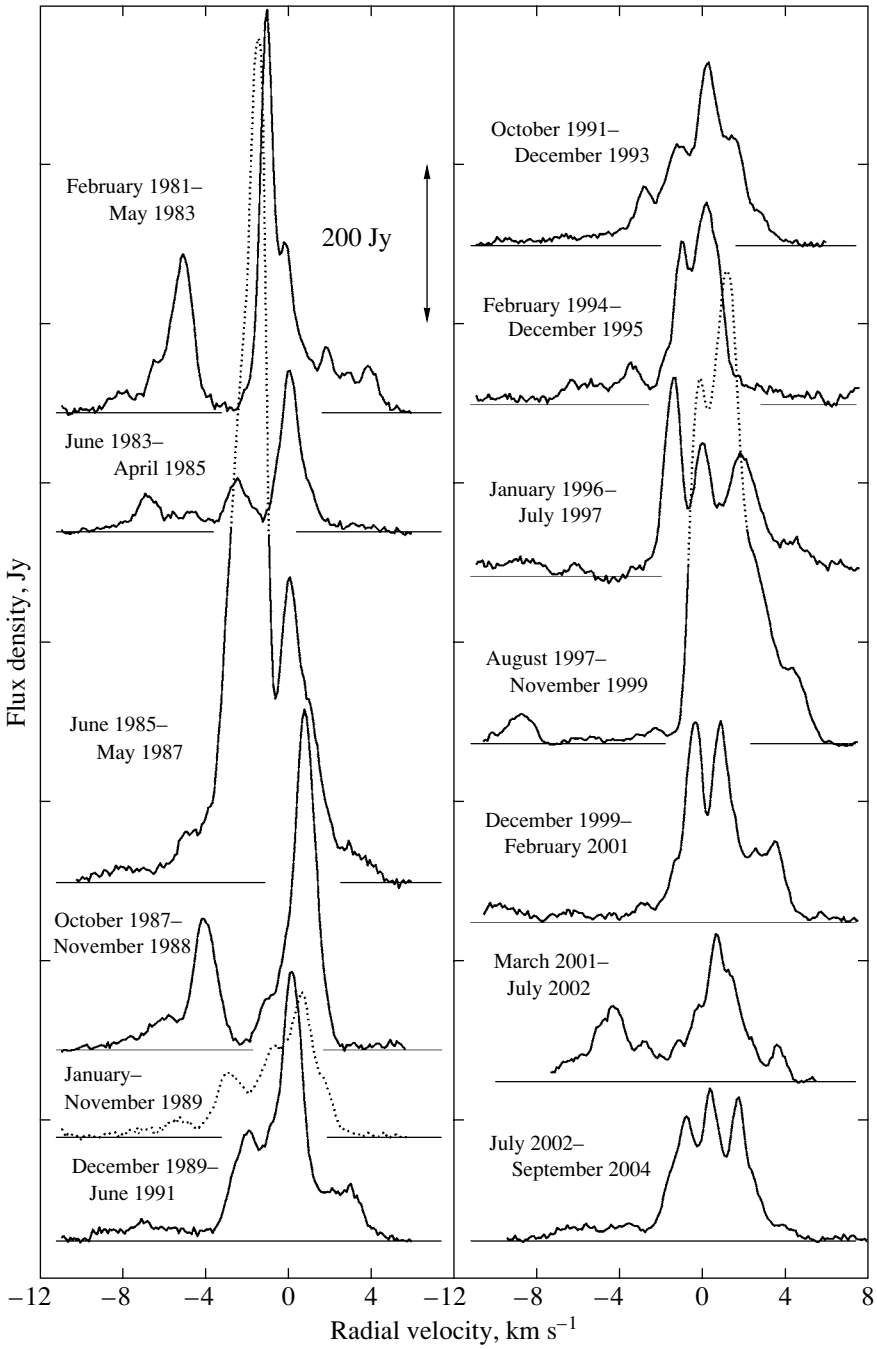

Fig. 3. Average spectra for various time intervals.

features). However, this was not easy to do, since the spectra exhibited a large number of closely spaced emission features. We realized that at certain times some of the features in the spectra dominated significantly over the features closest to them and their blending was marginal. For such features, we determined the radial velocities, flux densities, and even line widths with a high accuracy. These were reference emission features for us. Once the parameters of the reference components were determined, we fitted Gaussians into the H_2O spectra, which allowed us to determine the parameters of the remaining spectral components. The existence of a small number of weak components that we could not distinguish due to the complex structure of the spectra and strong blending cannot be ruled out.

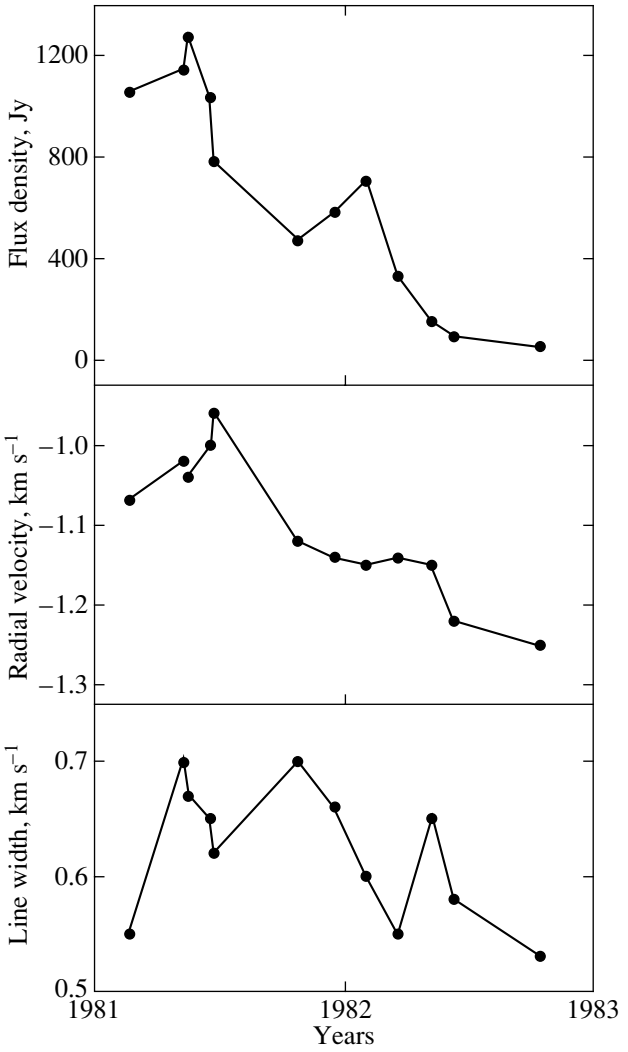

Fig. 4. Variability of the H_2O emission from the main component in W31(2) for the period 1981–1982.

We also found that, although the flux densities of a considerable number of emission features varied significantly with time, their radial velocities varied only slightly over the entire period of flare development. The widths of the isolated emission features were essentially identical, 0.6–0.8 km s ^{1}. The variations in the flux density, radial velocity, and line width of the main component for the period 1981–1982 are shown in Fig. 4.

We took a time interval of about two years to analyze the maser emission of the first flare. The small velocity and line width variations facilitated significantly the decomposition of the spectra into individual components. The results of this analysis are shown in Fig. 5a. For convenience, we fitted rectilinear segments and numbered all of the distinguished components in order of increasing radial velocity. The large and open circles represent the points that correspond to flux densities higher than 1000 Jy and $600 < F <$ 1000 Jy, respectively. The crosses mark the flux density peaks of the components with $300 < F < 600$ Jy. The flux density variability for some of the emission features is shown in Figs. 5b and 5c.

Figure 6a shows H_2O spectra at the epochs of the total flux subpeaks in the period 1990–1995. The vertical bars mark the emission features whose peaks coincided in time with the subpeaks. The right panels show the radial velocity drift for some of the emission peaks obtained (Figs. 6b, 6c) from all 1987–1993 H_2O spectra and (6d) from all average 1987–2001 spectra. The dashed lines represent the straight-line and polynomial fits.

The results from our analysis of the spectra for the 1998–1999 flare are presented in Fig. 7. For our data analysis, we chose an interval (1996–1999) wider than the duration of the flare itself. We included the activity cycle that preceded this flare. Some of the emission features exhibited a complex pattern of radial velocity drift (Fig. 7a). In such cases, the velocity variations were fitted by several rectilinear segments. The large and open circles represent the points with flux densities higher than 800 Jy and in the range 200–600 Jy, respectively. Figures 7b and 7c show flux density variations for some of the features.

DISCUSSION

The maser source W31(2) differs significantly from most of the water-vapor masers that are associated with single protostellar objects. Of greatest importance here is that there is a cluster of OB stars in the W31(2) region (Ho *et al.* 1986) and mass accretion toward this cluster (Keto *et al.* 1988). The absence of interferometric measurements for W31(2) only allowed us to make an assumption about the localization of H_2O maser spots (Lekht *et al.* 2004). The H_2O maser is most likely associated not with a single star of the OB cluster, but with several stars, although the influence of one of them could be dominant. All of this has a strong effect on the properties of the H_2O maser emission in W31(2). To investigate the maser properties, we analyzed the maser emission as a whole (the total flux, activity cycles, average spectra) and individual emission features during the strongest flares.

The Total Flux

Analyzing the total H_2O maser flux is of great importance in assessing the state of activity of the masing source in W31(2). Previously (Lekht *et al.* 2004), we showed that there is a pedestal in the total H_2O flux that reflects its slow variations. These variations

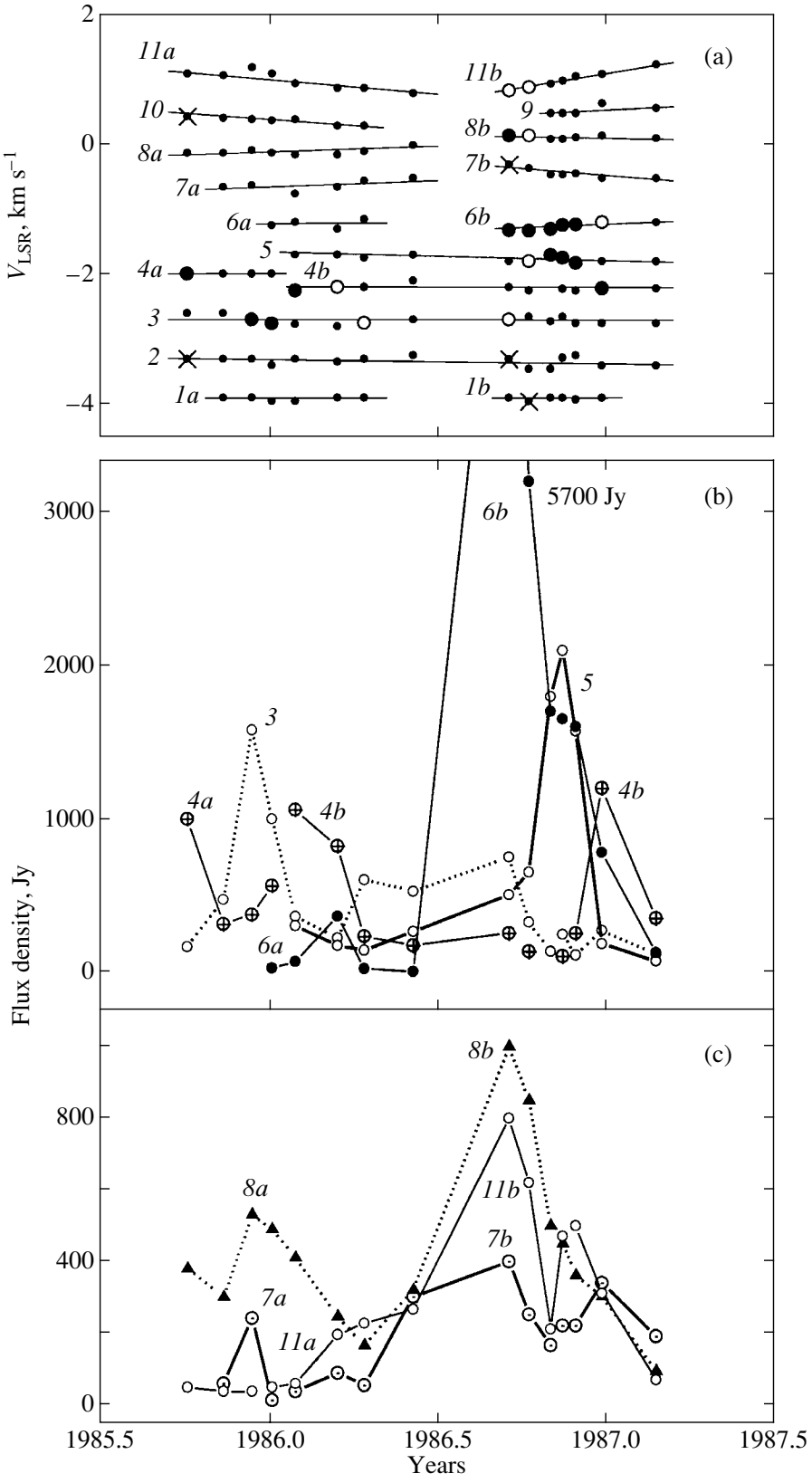

Fig. 5. Decomposition of the central parts of the H_2O spectra for the 1985–1986 flare in W31(2) into individual components.

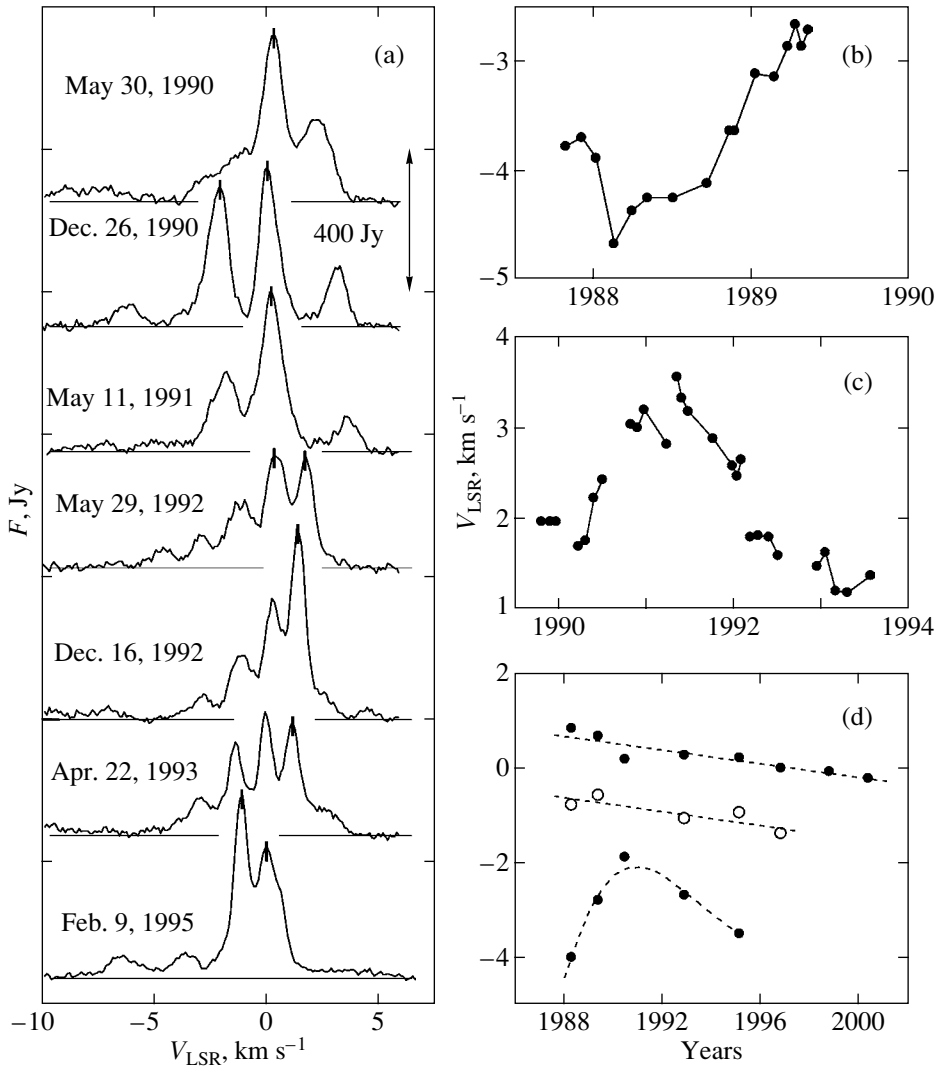

Fig. 6. (a) H_2O spectra at the epochs of the total flux subpeaks in the period 1990–1995; (b–c) V_{LSR} drift for some of the H_2O emission peaks in the period 1987–1995; (d) V_{LSR} drift for peaks of the average spectra in 1987–2001.

have no periodic component with a period shorter than the duration of our monitoring of W31(2), i.e., 22 yr (see Fig. 2a). After the subtraction of the slowly varying component, we obtained a component that could be characterized as the flaring H_2O maser activity (Fig. 2b). It had exhibited a more or less cyclic pattern since 1985. The cycle duration varied within the interval 1.5–2.5 yr, and the mean value was about 1.9 yr. The interval 1981–1985 is characterized by a fairly high intensity level at the beginning and an absolute minimum at the end for the entire 23-yr period of our observations of W31(2).

Two activity cycles were strongest (superflares): in 1985–1986 and 1998–1999. Can the interval of 12 years between them be taken as the period of the long-period flux variability? There is no unique answer to this question. The main objection is the absence of any correlation between the flux variability and the velocity centroid whose variability period was estimated to be within 31–33 yr (Lekht *et al.* 2004), although the nature of the centroid drift is not yet clear.

The absence of a distinct long-period component in the total flux variability, the nonuniform cyclicity, and the wide variety of flaring H_2O maser activity forms suggest that the maser spots in the region under consideration could have several pumping sources simultaneously (the cluster of OB stars) and the observed pattern of the total flux is a dynamic superposition of the emissions from the region of this cluster. An abundance of stars presumably leads to a blurring of the long-period variability component, which can exist separately in each star at an early stage of its evolution. In contrast, the flaring activity

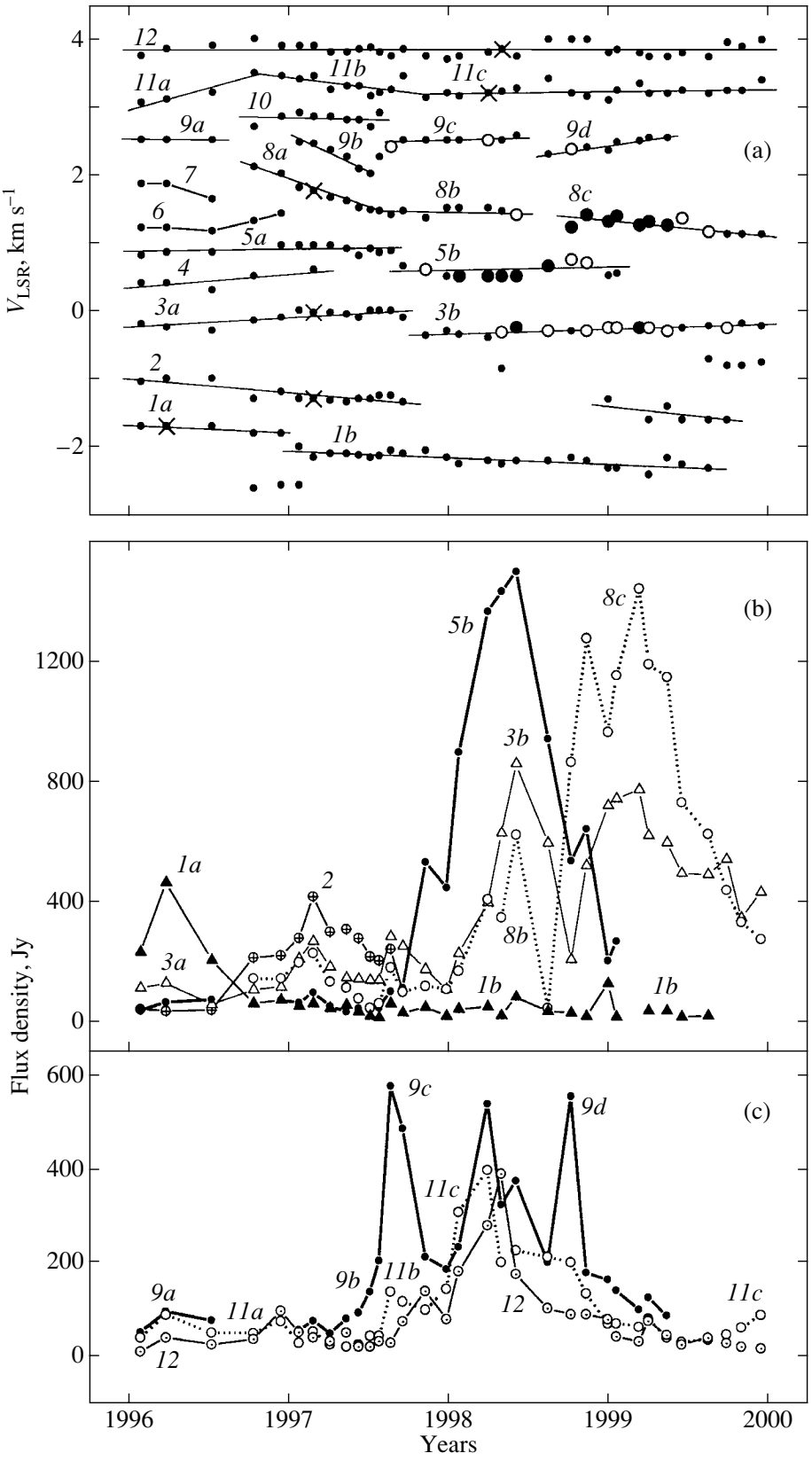

Fig. 7. Same as Fig. 5 for the 1998–1999 flare.

of a group of stars can lead to the observed pattern where flares continuously follow one another. The two strong flares with an interval of about 12 years could be a manifestation of the activity of the one nearest star in the OB cluster.

Below, we analyze the two strongest H_2O maser flares in W31(2). For the remaining activity cycles and for the 1989 minimum, we present the most interesting and important results.

The 1985–1986 Superflare

The 1985–1986 superflare was the most intense H_2O maser flare in W31(2) over the entire period of our observations of this source. It was preceded by the period from February 1981 through May 1983 that is characterized by high maser activity and the presence of two separate groups of features in the spectrum with a dividing line at -3 km s^{-1} (see Fig. 3). The entire radial velocity range for the H_2O emission is from -10 to 5 km s^{-1} and extended to -15 km s^{-1} in early 1982. The highest flux density was observed at $V_{LSR} \approx -1.1$ km s^{-1}. The evolution of this emission was very dynamic over a fairly short period (Fig. 4a). The pattern of V_{LSR} and line width variability suggests that the structure of the emission line is complex—the feature was not single at certain epochs of observations. Since the beginning of 1982, V_{LSR} decreased, while the line narrowed. At the end of this year, the velocity of the feature decreased to -1.25 km s^{-1}, and, subsequently, its emission disappeared. It was at this velocity that weak emission appeared for a short time in early 1986 and the most intense flare (superflare) occurred in the second half of this year.

At the initial stage of this flare (late 1985–early 1986), the H_2O emission extended from -10 to 4.5 km s^{-1}. At the maximum of the flare, the radial velocity range in which the maser emission was observed was at a minimum, from -5 to $+2.5$ km s^{-1}. On the descending branch of the flare evolution, the velocity range gradually broadened in 0.5 yr, and the emission was observed from -10 to $+5$ km s^{-1}.

Almost all of the emission features were distributed in the H_2O spectrum more or less uniformly. The mean separation between them was about 0.5 km s^{-1}. The line widths of the individual features were fairly large and approximately identical, from 0.6 to 0.8 km s^{-1}. The mean velocity centroid in this period was -1.5 km s^{-1}, and its changes relative to this value were insignificant (Lekht *et al.* 2004).

There was a correlation between the flux density variations for most of the emission features. Thus, the emission peaks at -2.7, -0.3, 0.2, and 1 km s^{-1} coincide with the peak of the main feature at $V_{LSR} = -1.3$ km s^{-1}. The emission peaks of the three most intense emission peaks (-1.3, -1.7, and -2.2 km s^{-1}) do not coincide in time. The delays of the peaks of the second and third features relative to the first feature were, respectively, about 0.18 and 0.12 yr (see Fig. 5b). The delays may be attributable to the successive excitation of emission in maser spots at $V_{LSR} = -1.3$, -1.7, and -2.2 km s^{-1}. The successive decrease in radial velocity could be an argument for the existence of a radial velocity gradient in the H_2O masing region.

Emission drift was observed only at radial velocities >-2 km s^{-1}, i.e., in the velocity range from -1.8 to $+1.5$ km s^{-1}. These velocities are slightly higher than the velocity of the molecular cloud. The emission features approached one another in the spectrum before the maximum of the flare and moved apart after the maximum. In general, the main features *6* and *5* had radial velocities of -1.3 and -1.7 km s^{-1} over the entire period 1985–1986. However, on the descending branch of the flare evolution, when their flux densities were more or less identical (1600–2100 Jy), there was a radial velocity drift of the features for two months. The drift rate was high, 0.14 and -0.22 km s^{-1} per month, respectively (see Fig. 5a). It should be noted that the features initially approached one another and then moved apart. This phenomenon was explained previously (Lekht *et al.* 1996) for the source S252A.

The correlated radial velocity and flux density variations suggest that the emission features in the velocity range from -1.3 to $+1.5$ km s^{-1} and the feature at -2.7 km s^{-1} have a direct bearing on the flare. All of them appear to be arranged in W31(2) as a compact group and to be associated with an accretion flow onto the cluster of OB stars (Ho *et al.* 1986).

The activity cycle from November 1987 through May 1989, which followed the superflare, is characterized by the presence of two separate groups of emission features in the H_2O spectra. A significant drift of the emission peak within $-4.7 \ldots -2.7$ km s^{-1} (Fig. 6b) was observed in the first group. This resulted from the successive appearance of emission of the components in order of increasing radial velocity. The initial period when the feature at -4.7 km s^{-1} appeared was an exception. The drift of the peak of the second group was much smaller (0.5 km s^{-1}) and in the opposite direction. It resulted from the change in the intensity ratio of two spectrally close components with radial velocities of 1.2 and 0.7 km s^{-1}.

The successive appearance of emission in order of increasing radial velocity may be indicative of a velocity gradient in the medium where the H_2O maser spots are localized.

Evolution of the H_2O Emission in the Period 1989–1995

The two cycles of flaring activity in W31(2) in the period from December 1989 through December 1993 are intermediate between the superflares and lie between the two most stable and prolonged minima of the total flux.

In the first cycle (December 1989–June 1991), the most intense features formed a compact group in the velocity range from −2 to 2.5 km s^{-1}. The weak emission extended up to −10 km s^{-1}. Subsequently, the velocity range of the strongest emission broadened, with individual, isolated features being clearly seen. Such a structure was observed during almost the entire next cycle (October 1991–December 1993).

Subsequently, during 1995, the emission was observed over a wide velocity range, from −11 to 10 km s^{-1}. However, as previously, the main emission features were arranged in the spectrum as a compact group from −2 to +2 km s^{-1}. This is also clearly seen in the average spectrum (Fig. 3).

Note that the emission in the activity cycles themselves was flaring in nature with subpeaks (Fig. 2a). Seventeen subpeaks were observed over the entire monitoring, except the period of high maser activity 1980–1982. There were seven subpeaks from 1990 until 1995; their total fluxes were close and lay within the range 1100–1350 Jy km s^{-1}. We compared the H_2O spectra themselves at the epochs of these subpeaks 1990–1995 (Fig. 6a). It turned out that at these epochs, one or two emission features also had emission peaks. These are marked by the vertical bars. Despite the large differences in spectral structure, the emission of some of the components at close radial velocities was repeated. This suggests the existence of stable structures responsible for the H_2O maser emission and, apparently, a complex pumping source.

The interval 1989–1995 is characterized by a drift of the emission peak of the group of features with velocities in the range $1 < V_{LSR} < 4$ km s^{-1} (Fig. 6c). The curves have breaks that suggest that there were not one but several emission features. The maser emission was successively excited in them, suggesting the existence of an ordered structure of the maser emission region in the velocity range 1–4 km s^{-1}.

The 1998–1999 Superflare

Although the 1998–1999 flare was weaker than the preceding flare, it may also be reckoned to be a superflare, since the distance to W31(2) is ≈6 kpc. To get a more complete picture of the evolution of this flare, we included the activity cycle in 1996–1997.

The flare was longer in duration, and there was no such sharp emission peak as that during the 1985–1986 flare. It is important that the velocity centroid of the spectra shifted by +2.5 km s^{-1} relative to the centroid in 1985–1986. The strongest emission was observed at velocities from −1 to 4 km s^{-1}.

The H_2O line profiles were very complex and more extended than those in 1985–1986. These contained a large number of emission features. At certain epochs of observations, the overlapping of features in the spectra was significant, which severely complicated the decomposition of the spectra into individual components. The line widths of the emission features lay within the range 0.6–0.8 km s^{-1}.

During the 1998–1999 flare (see Fig. 7), there was no component that would dominate significantly over the remaining components. The emission at 0.5 and 1.3 km s^{-1} with peak flux densities of about 1500 Jy was most intense; the shift in time between the peaks was nine months. At the peak of the total flux (early 1998–mid-1999), there was absolutely no emission at velocities of −1.7 and −1.3 km s^{-1} that was strongest during the 1985–1986 flare. Before this time, it was present in the H_2O spectra (features *1* and *2* in Fig. 7). In contrast to the 1985–1986 superflare, there was a reverse sequence of emission peaks—first the emission peak at −1.7 km s^{-1} with a flux density of 460 Jy and then a peak at −1.3 km s^{-1} with a flux density of 420 Jy were observed. The delay was ten months, i.e, much longer than that in 1985–1986.

The radial velocities of the individual emission features varied over the entire interval 1996–1999 (Fig. 7a). The largest spread in velocities could arise from the influence of the weak components that we failed to distinguish due to the complex structure of the spectra at certain epochs of observations. Features *8a* and *9b* had the highest rate of change in their velocity: −0.8 and −1.1 km s^{-1}, respectively (see Fig. 7a). It occurred at the activity cycle that preceded the 1998–1999 flare. We failed to find any correlation between the flux density and radial velocity variations. However, there is a clear correlation between the flux densities of the features both in the 1997 activity cycle and during the strong 1998–1999 flare. Feature *9* constituted an exception. Its three peaks did not correlate in any way with the main peaks of the 1998–1999 flare.

The Flares after 1999

The flare with a peak flux density of about 600 Jy at $V_{LSR} = -0.67$ km s^{-1} formed the basis for the flaring activity from December 1999 through March 2001. The strongest emission was observed in a slightly

different velocity range than that before the 1998–1999 superflare, from −2 to 5 km s^{-1}, and the weak emission was observed from −10 to −7.5 km s^{-1}. At the end of 2000, we clearly distinguished peaks that were uniformly distributed in the spectrum over the velocity range from −11 to +5 km s^{-1}. All of this was accompanied by a decrease in the intensity of the strongest features and led to a reduction in the total flux.

Subsequently, from mid-2001 until mid-2002, there was a short burst of H_2O maser activity against the background of the minimum total flux, ~600 Jy km s^{-1}. It was characterized by a high intensity level in a wide velocity range: from −7.5 to +5 km s^{-1}.

The last activity cycle, which began in mid-2002, resembles the 1989–1993 evolution period of the emission. The difference lies only in the fact that the main group of features was more compact, from −2 to +4 km s^{-1}, while the weak emission occasionally extended from −8 to 12 km s^{-1}.

Average Spectra

The average spectra obtained for all time intervals differ in structure. Only the 1987–1989 and 2001–2002 average spectra are more or less similar. The velocity ranges of the emission in most average spectra are close and extend from −10 to +6 and, for the interval 1994–1997, up to +8 km s^{-1}. For the individual H_2O spectra, the radial velocity range of the emission differed and was alternately narrower and wider, from −15 to +15 km s^{-1}. The emission at the edges of the spectra was generally weak and fast-variable, and it did not correlate with the velocity centroid. This implies that the emission of the central part of the H_2O spectrum is mainly responsible for the oscillations of the velocity centroid with a period of 30–32 yr and an amplitude of 1.1 km s^{-1} (Lekht *et al.* 2004).

A comparison of the 1987–2001 average spectra indicates that, despite the complex dynamics of the individual spectra, there was a regular drift of the three main emission peaks (Fig. 6d). As we showed above, the drift of the isolated features is small, and it cannot be responsible for the observed phenomenon for the emission at $V_{LSR} < 0$. The drift of the peak was caused by the successive appearance of emission of the features in order of increasing or decreasing radial velocity. The drift arose immediately after the 1985–1986 superflare. There seems to be a common factor that is responsible for the superflare and the successive excitation of emission in maser spots. This is possible when a radial velocity gradient exists in the medium where maser emission emerges.

Individual Emission Features

The absence of a large radial velocity drift for the main emission features made it possible to trace the evolution of the emission from stable maser spots, although their emission was repeatedly interrupted. This was done for the emission features at −1.7, −1.3, 0.5, and 1.3 km s^{-1} that dominated during the superflares.

The emission feature at −1.3 km s^{-1} was most active. We observed it from late 1982 through August 2004 with breaks. In addition to the main 1986 flare, there were seven emission peaks of this feature in the period 1987–2000. Each such peak lies in one of the seven consecutive activity cycles, except the cycle of the 1998–1999 superflare when the emission at velocities from −2 to −1 km s^{-1} was completely suppressed. Thus, including the 1986 superflare, we can assert that there was a clear correlation between the variability of the emission at −1.3 km s^{-1} and the cycles of maser activity from 1986 until 2000, except the period 1998–1999. After 2000, weak emission occasionally appeared at −1.3 km s^{-1}. Since it was sometimes strongly blended with the emission at close velocities, we could not reliably determine the times of the peaks. Nevertheless, we also clearly see a correlation with the two succeeding activity cycles.

We observed the emission feature at −1.7 km s^{-1} from the very beginning of our monitoring of W31(2): from February 1982 until late 2003 with frequent and prolonged breaks. The strongest emission after the first superflare was in the period 1989–1996. In these years, the emissions at −1.7 and −1.3 km s^{-1} competed between themselves, i.e., the emission of one of the features alternately dominated significantly over the emission of the other feature. The flux density peaks at −1.7 km s^{-1} generally coincided with the minima of the total flux. In contrast to 1986, when the delay between the flux density peaks was 0.18 yr, we cannot introduce the concept of delay for the period 1988–2000 due to the complex pattern of the flux density variability. Where the positions of the peaks were nevertheless determined, the delays exceeded one year. These apparently were of a different nature than those in 1986. The observed anticorrelation between the flux densities can most likely be explained in terms of the competition between the spatial emission modes for pumping in a partially saturated maser (see, e.g., Cesaroni 1990).

The search for the features at 0.5 and 1.3 km s^{-1} was complicated by the fact that the H_2O spectra were complex and there was strong blending, particularly from the emission near zero velocities. Sometimes, we could not decompose the spectra into individual components in the velocity range under consideration. The emission in the velocity range 0.5 ±

0.2 km s^{-1} was observed with breaks during the entire monitoring. Here, we mean the position of the line peak in the velocity range under consideration. The line itself had a width of 0.5–0.6 km s^{-1}. The duration of each series of the active emission phase did not exceed two years. Two emission features located at the edges of the velocity range under consideration were most commonly observed in turn. The 1998 superflare occurred at the middle velocity, i.e., at 0.5 km s^{-1}.

The emission near 1.3 km s^{-1} (1.2–1.5 km s^{-1}) was clearly observed since 1986. All seven recorded emission peaks occurred at seven different cycles of maser activity.

At $V_{LSR} < -8$ km s^{-1}, the emission was generally weak, 5–15 Jy. The strongest emission at these velocities, 40–120 Jy, was observed during 1996–2000. There was a clear correlation with the components of the total flux that we called subpeaks (see the Section "Evolution of the H_2O Emission in the Period 1989–1995" and Fig. 2a).

Thus, there are radial velocities or narrow ranges of velocities at which the most intense water-vapor maser emission was regularly observed. The variability of this emission clearly correlates with the cycles of maser activity in W31(2), while the short-duration and weaker emission at $V_{LSR} < -8$ km s^{-1} correlates rather well with the subpeaks. We can assume the existence of a common pumping source, a cluster of OB stars, with a flaring nature of its activity. The maser spots responsible for the emission of the central part of the spectrum can form a compact group with an ordered structure.

CONCLUSIONS

Our main results are listed below:

(1) Analyzing our monitoring data for W31(2) in the 1.35-cm water-vapor line, we conclude that the maser emission and the spectral structure are very dynamic and highly variable, although the main features were traceable throughout our 23-year monitoring of W31(2).

(2) The variability of the H_2O maser in W31(2) exhibits a cyclic pattern with a mean period of about 1.9 yr. Several short flares, subpeaks, were observed in each activity cycle. During strong flares, there was a correlation between the flux densities of the spectral components with close radial velocities.

(3) There was a clear correlation between the emission peaks of the four main components (−1.7, −1.3, 0.5, and 1.3 km s^{-1}) with the detected activity cycles.

(4) The radial velocity drift of the individual features was small, which clearly distinguishes W31(2) from most of the water-vapor maser sources.

(5) The emission of the individual features was excited successively in order of increasing or decreasing radial velocity, which is indicative of an ordered structure of the region where the maser spots are localized. This was observed for several groups of features located in different regions of the H_2O spectrum. There is apparently a radial velocity gradient in the medium where the maser source is located.

(6) The shift in the velocity centroid with a period of 31–33 yr is attributable to the variability of the emission in the central part of the H_2O spectrum and could be related to variations in the accretion flow onto the cluster of OB stars in the source W31(2).

(7) The emission of one of the spectral components with close radial velocities (0.5 and 1.3 km s^{-1}) and the low-velocity emission were suppressed during the 1985–1986 and 1998–1999 superflares; this occurs in a partially saturated maser when the spatial emission modes compete for pumping. The above could be an argument for a compact arrangement of maser spots in W31(2).

(8) We observed the influence of two strong emission features at −1.7 and −1.3 km s^{-1} on one another (their approach and subsequent separation). This is most likely attributable to the manifestation of coherent properties of the emission where the maser spots are arranged almost along the line of sight and have close radial velocities within the Doppler and turbulent line width.

(9) The absence of VLA H_2O maps does not allow a definite model of the water-vapor maser in W31(2) to be constructed. We can only assume that the maser spots form a compact structure, have a common pumping source, and are associated with an accretion flow onto the cluster of OB stars.

Studying the dynamics of the water-vapor maser and its individual spectral components allows us to refine the model of the water-vapor maser in W31(2). The results of such studies will be presented in our ensuing publications.

ACKNOWLEDGMENTS

This work was supported by the State Science and Technology Committee on the RT-22 facility (registration no. 01-10). We are grateful to the staff of the Pushchino Radio Astronomy Observatory, Russian Academy of Sciences, for their great help with the observations.

REFERENCES

1. R. Cesaroni, Astron. Astrophys. **233**, 513 (1990).
2. P. T. P. Ho and A. D. Haschick, Astrophys. J. **248**, 622 (1981).
3. P. T. P. Ho and A. D. Haschick, Astrophys. J. **304**, 501 (1986).
4. P. T. P. Ho, R. I. Klein, and A. D. Haschick, Astrophys. J. **305**, 714 (1986).
5. E. R. Keto, P. T. P. Ho, and A. D. Haschick, Astrophys. J. **324**, 920 (1988).
6. E. R. Keto, P. T. P. Ho, and M. J. Reid, Astrophys. J. Lett. **323**, L117 (1987).
7. E. E. Lekht, I. I. Berulis, and J. E. Mendosa-Torres, Astron. Zh. **73**, 844 (1996) [Astron. Rep. **40**, 768 (1996)].
8. E. E. Lekht, V. A. Munitsyn, and A. M. Tolmachev, Astron. Zh. **81**, 224 (2004) [Astron. Rep. **48**, 200 (2004)].
9. E. J. Wright, G. G. Fazio, and F. J. Low, Astrophys. J. **217**, 724 (1977).

Translated by V. Astakhov

Astronomy Letters, Vol. 31, No. 5, 2005, pp. 327–334. Translated from Pis'ma v Astronomicheskiĭ Zhurnal, Vol. 31, No. 5, 2005, pp. 363–371.

Magnetic Field and Chemical Composition of the Peculiar Star HD 10221

Yu. V. Glagolevskii[1]*, T. A. Ryabchikova[2], and G. A. Chountonov[1]

[1] *Special Astrophysical Observatory, Russian Academy of Sciences, Nizhniĭ Arkhyz, 357147 Karachaĭ-Cherkessian Republic, Russia*

[2] *Institute of Astronomy, Russian Academy of Sciences, ul. Pyatnitskaya 48, Moscow, 119017 Russia*

Received December 20, 2004

Abstract—We analyzed the chemical composition of the chemically peculiar (CP) star HD 10221=43 Cas using spectra taken with the NES spectrograph of the 6-m telescope with a spectral resolution of 45 000. The Hβ line profile corresponds most closely to $T_{\rm eff} = 11\,900$ K and $\log g = 3.9$. The rotational velocity is $v_{\rm e} \sin i = 27 \pm 2$ km s^{-1}, and the microturbulence is $\xi_{\rm t} = 1$ km s^{-1}. The results of our abundance determination by the method of synthetic spectra show that the star has chemical anomalies typical of SrCrEu stars, although its effective magnetic field is weak, $B_{\rm e} < 100$ G. For silicon, we obtained an abundance distribution in atmospheric depth with a sharp jump of 1.5 dex at an optical depth of $\log \tau_{5000} = -0.3$ and with silicon concentration in deep atmospheric layers. Similar distributions were found in the atmospheres of cooler stars with strong and weak magnetic fields. A comparison of the chemical peculiarities in HD 10221 with known CP stars with magnetic fields of various strengths leads us to conclude that a low rotational velocity rather than a magnetic field is the determining factor in the formation mechanism of chemical anomalies in the atmospheres of CP stars. © *2005 Pleiades Publishing, Inc.*

Key words: *stars—variable and peculiar, stellar chemical composition.*

INTRODUCTION

HD 10221=43 Cas is a representative of the chemically peculiar (CP) SiSrCrEu stars. According to preliminary data (Glagolevskii *et al.* 1986), this star has a very weak magnetic field ($B_{\rm e} < 100$ G). The chemical peculiarity per se by no means suggests that a global magnetic field is necessarily present, but the reverse is true: no magnetic star with a normal chemical composition has been found. A small percentage of the He-rich, He-weak, Si, and SrCrEu CP stars that are known for the presence of strong global magnetic fields reveal no field, probably because it is weak. At present, the accuracy of magnetic field measurements has increased significantly through the use of CCD arrays, but no field has been detected in many CP stars (Glagolevskii and Chuntonov 2002). A magnetic field is assumed to stabilize the stellar atmospheres, facilitating the diffusion of chemical elements under light pressure and gravity. In stars with weak magnetic fields, such stabilization cannot be achieved in full measure, but the diffusion of chemical elements still takes place, producing typical chemical anomalies. What is the actual influence of a magnetic field on the diffusion processes? How is the diffusion effect related to the rotational velocity? What distinguishes He-rich, He-weak, Si, and SrCrEu stars with weak magnetic fields from nonmagnetic PGa, HgMn, and Am stars? All these questions require an answer.

A detailed study of stars with weak magnetic fields is of great importance for the following reasons. Magnetic stars exhibit characteristic chemical and other anomalies, and a magnetic field is generally believed to be a factor that affects the appearance of the anomalies. Studying the chemical anomalies in stars with global magnetic fields over a wide range of strengths will undoubtedly make it possible to improve the theory for the diffusion of chemical elements. Another important problem is the slow rotation of CP stars. The loss of angular momentum is generally believed to involve a magnetic field at early evolutionary stages (Stępień 2000). However, "fieldless" stars do not satisfy this hypothesis. Therefore, finding the true cause of the slow rotation of CP stars is of great importance in refining the origin and evolution of this class of stars.

Here, we investigate the magnetic field and chemical composition of HD 10221, a slowly rotating CP star with a weak magnetic field.

OBSERVATIONS AND DATA REDUCTION

To measure the magnetic field, we obtained observational data on January 18/19, 2003, with the

*E-mail: glagol@sao.ru

main stellar spectrograph of the 6-m telescope (JD = 2452658.1) using a 2K×2K CCD array and the DINA code created in the Advanced Design Laboratory at Special Astrophysical Observatory (SAO). The spectral resolution was 15 000, and the wavelength range on the 2K×2K CCD array was 4360–4600 Å. We processed the spectra and measured the magnetic field using a code written by Kudryavtsev (2000). To reduce the effect of nonuniform pixel sensitivity, we successively took 10-min exposures in turn at two positions of an achromatic quarter-wave phase plate at angles of 0° and 90°. All the individual exposures at 0° and 90° were added separately. In this way, we obtained two pairs of spectra at the end of the exposures with opposite polarizations, but recorded on the same pixels. For this reason, the Zeeman shift $\Delta\lambda$ between them does not depend on the pixel sensitivity. The longitudinal magnetic field component B_e, which is also called an effective magnetic field, was determined from the relation

$$\Delta\lambda = \lambda_R - \lambda_L = 2.34 \times 10^{-13} g_{eff} \lambda^2 B_e.$$

The mean Lande factor (g_{eff}) for all spectral lines was taken to be 1.23. A total of 16 Zeeman spectra were obtained.

To determine the chemical composition of HD 10221, we used two echellè spectra obtained with the NES spectrograph of the 6-m telescope on January 11/12, 2004 (JD = 2453017.3). The covered spectral range is 4030–5453 Å, the resolution is 45 000, and the signal-to-noise ratio is ~150–200. The echellè spectra were also processed using the software package by Kudryavtsev (2000).

THE MAGNETIC FIELD

The effective magnetic field B_e was measured with a Zeeman analyzer by Glagolevskii and Chountonov (2002) and Aurière *et al.* (2005). All these measurements showed that the strength of the effective magnetic field is probably less than 100 G. We increased the accuracy of our measurements by using good-quality spectra and by increasing the signal accumulation time. Based on the spectra presented here, we obtained $B_e = -42 \pm 15$ G. The measurements were performed by the standard differential method using 794 lines from 16 individual exposures. When only symmetric nonblended lines were selected, the field was found to be -80 ± 20 G. For a check, we measured the magnetic field of the star HD 30466, 1160 G. All the available measurements for HD 10221 and the check star are given in Table 1.

Unfortunately, the rotation period HD 10221 is not accurate enough (see the Section "Surface Nonuniformity of the Chemical Composition"). Therefore, we cannot say whether the field reversal is associated with rotation or this is the result of observational errors. However, we can take the maximum longitudinal magnetic field in HD 10221 to be about 100 G with a high probability.

ATMOSPHERIC PARAMETERS

Based on the total spectral energy distribution, we determined the atmospheric parameters for HD 10221, $T_{eff} = 10\,730$ K and $\log g = 3.8$, previously (Glagolevskii 2002). However, these parameters do not correspond to the observed Hβ line profile. Therefore, we attempted to redetermine the atmospheric parameters using various calibrations of the photometric indices in Strömgren's system. These indices were taken from the catalog by Hauck and Mermilliod (1998). The TempLogg code, which was developed at the Institute of Astronomy of the Vienna University (Kaiser 2005), was used to determine the parameters. The effective temperatures and surface gravities derived from various calibrations are listed in Table 2.

We see from this table that, whereas all calibrations yield the same surface gravity, $\log g \approx 3.9$, the effective temperatures can be broken down into two groups that differ by about 1000 K. We have the Hβ line profile at our disposal, which was used to test the atmospheric parameters of the star. We computed several atmospheric models using the ATLAS9 code by Kurucz (1993) with effective temperatures in the range 10 700–12 000 K and with surface gravities in the range 3.5–4.0. Since our chemical abundance analysis (see the next section) showed that the abundances of many elements, including iron, were much higher than their solar values, we computed the models with metallicities of $M = +0.5$ and $+1.0$. The calculations of the Hβ line profile, along with all our synthetic-spectrum calculations, were performed using the SYNTH3 code, which was written by Piskunov (1992) and modified by O. Kochukhov to speed up the calculations. The code uses an improved hydrogen-line broadening theory (Barklem *et al.* 2000). Good agreement between the computed and observed profiles was obtained for the model with $T_{eff} = 11\,900$ K, $\log g = 3.9$, and $M = +0.5$, which, within the standard error limits ±200–300 K and ±0.1–0.2 K, agrees with the photometric calibrations by Moon and Dworetsky (1985), Balona (1994), Ribas *et al.* (1997), and Castelli *et al.* (1997) (Fig. 1). To represent the observed Hβ line profile with a lower temperature, $T_{eff} = 11\,000$ K, the surface gravity must be reduced to 3.5 or event lower. However, in this case, the region of the profile near the Hβ core is represented much worse than that with the 11900g39 model. For the final choice to be made between the

Table 1. Magnetic fields of HD 10221 and the standard star HD 30466

JD 2400000+	B_e, G	σ, G	Reference
		HD 10221	
52 250.29	+24	30	Glagolevskii and Chountonov (2002)
52 251.12	+34	38	Glagolevskii and Chountonov (2002)
52 298.21	−14	52	Glagolevskii and Chountonov (2002)
	+93	32	Aurière *et al.* (2005)
52 658.1	−80	20	This paper
		HD 30466	
Nov. 12, 1956	+2320	340	Babcock (1958)
Dec. 21, 1956	+1890	132	Babcock (1958)
44 659.233	+1690	540	Glagolevskii *et al.* (1982)
44 661.300	+250	320	Glagolevskii *et al.* (1982)
52 658.229	+1160	80	This paper

two models, we must have the profiles of other hydrogen lines, for example, Hα, and the spectral energy distribution. In this paper, we use two models, 11900g39 and 11000g35, for our abundance analysis (these values virtually span the temperature range in Table 2).

THE CHEMICAL COMPOSITION

We determined the atmospheric chemical composition of HD 10221 from the equivalent widths of nonblended lines using the WIDTH9 code (Kurucz 1993) modified by V. Tsymbal and by computing the synthetic spectra of partially blended lines using the SYNTH3 code. The ROTATE code, written by N. Piskunov in the IDL language, was used to convolve the synthetic spectrum with the instrumental profile and the rotation profile. The rotational velocity was finally determined by minimizing the root-mean-square deviation of the synthetic profile from the observed profile. We took the atomic parameters of spectral lines for our abundance calculations mainly from the Vienna Atomic Line Database (VALD) (Kupka *et al.* 1999; Ryabchikova *et al.* 1999). For several chemical elements, we used the following sources of oscillator strengths: Raassen and Uylings (1998) for Cr II and Fe II, Ryabtsev (2004) for Pr III and Tb III, and Zhang *et al.* (2002) for Dy III. The microturbulence determined from the absence of a dependence of the iron and chromium abundances on the equivalent widths of individual lines is slightly smaller than 1 km s^{-1}. In all our subsequent calculations, we used $\xi_t = 1$ km s^{-1}. The rotational velocity was found from nonblended Cr II and Fe II lines to be $v_e \sin i = 27 \pm 2$ km s^{-1}. There are three published estimates of the stellar rotational velocity: $v_e \sin i = 10$ km s^{-1} (Abt and Morrell 1995), $v_e \sin i = 25$ km s^{-1} (Uesugi and Fukuda 1982), and $v_e \sin i = 18$ km s^{-1} (Royer *et al.* 2002). Our value corresponds most closely to that obtained by Uesugi and Fukuda (1982). The observed and synthetic spectra of HD 10221 near the Fe I, II, and III lines are compared in Fig. 2 for two atmospheric models, 11900g39 and 11000g35.

The chemical composition of the star HD 10221 computed in two versions (columns 2 and 3) is

Table 2. Atmospheric parameters for HD 10221

T_{eff}, K	log g	Reference
11 890	3.87	Moon and Dworetsky (1985)
11 030	3.94	Napiwotzki *et al.* (1993)
11 780	4.12	Balona (1994)
11 730	3.95	Ribas *et al.* (1997)
11 780	3.90	Castelli *et al.* (1997)
10 730	3.80	Glagolevskii (2002)

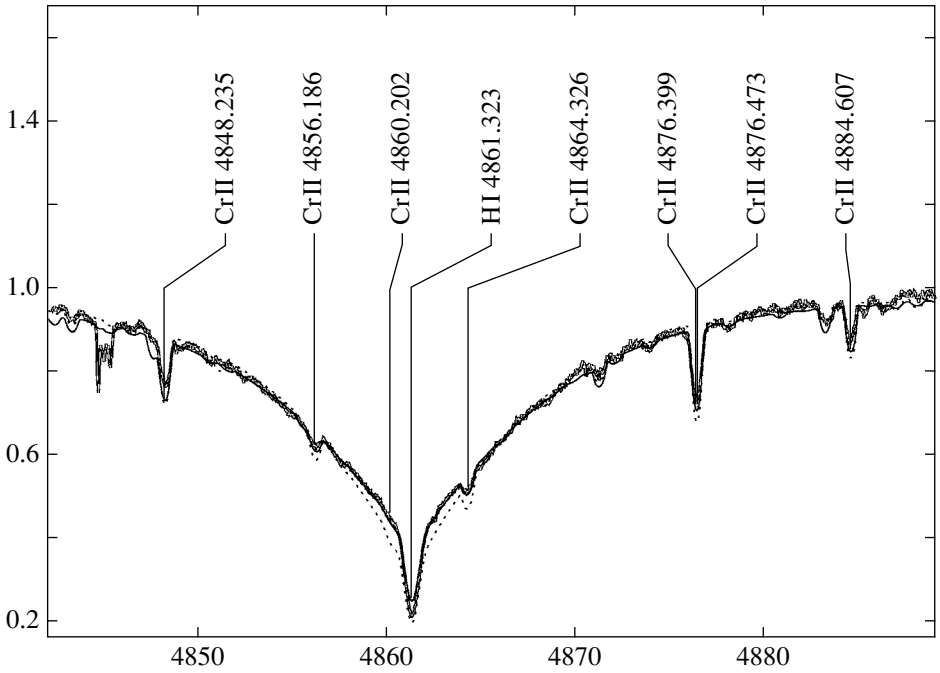

Fig. 1. Comparison of the observed (double line) and synthetic Hβ line profiles computed for two atmospheric models: 11900g39 (solid line) and 11000g35 (dotted line). Wavelengths in Å and residual intensities are along the coordinate axes.

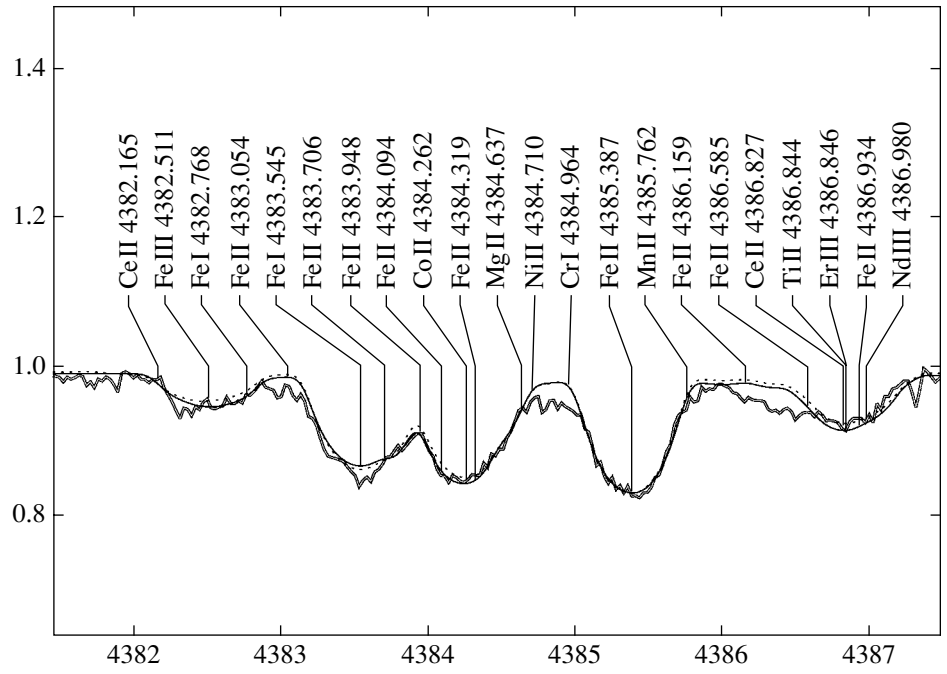

Fig. 2. Same as Fig. 1 for the 4385 Å region.

given in Table 3. For comparison, we also give the chemical compositions of another typical CP star, HD 43819 (Lopez-Garcia and Adelman 1994), and the Sun (Grevesse and Sauval 1998; Holweger 2001) (columns 4 and 5, respectively). We see clearly that HD 10221 exhibits a large overabundance of Si, Cr, Fe, Sr, Eu, and other rare-earth elements; their overabundance is larger than that in HD 43819. We see an underabundance of the light elements C and Al and an order of magnitude or larger underabundance

Table 3. Atmospheric chemical composition of HD 10 221. The chemical compositions of the AP star HD 43819 and the Sun are given for comparison

Species	11900g39 $\log(N/N_{\rm tot})$	11000g35 $\log(N/N_{\rm tot})$	Number of lines, n	HD 43819 $\log(N/N_{\rm tot})$	Sun $\log(N/N_{\rm tot})$
He I	<-2.0	<-2.0	3		-1.05
C II	-4.10	-4.10	1	-3.78	-3.45
O I	-2.9	-3.0	1		-3.30
Mg II	-5.50	-5.50	1	-4.72	-4.50
Al II	-6.07	-6.10	1		-5.57
Si II	-3.55 ± 0.15	-3.48 ± 0.15	3	-3.88	-4.50
Si III	-2.60 ± 0.27	-2.45 ± 0.27	2		-4.50
S I	-4.96	-4.92	1	-5.46	-4.71
Ti II	-6.37 ± 0.25	-6.47 ± 0.25	10	-5.81	-7.02
V II	-6.85	-7.30	1		-8.04
Cr I	-4.06 ± 0.07	-4.39 ± 0.15	2	-4.69	-6.37
Cr II	-4.43 ± 0.32	-4.66 ± 0.33	27	-5.02	-6.37
Mn II	-4.94 ± 0.31	-5.12 ± 0.29	8	-5.55	-6.65
Fe I	-3.14 ± 0.39	-3.41 ± 0.37	8	-3.48	-4.54
Fe II	-3.36 ± 0.24	-3.49 ± 0.29	57	-3.66	-4.54
Fe III	-3.07 ± 0.43	-2.94 ± 0.81	3	-3.70	-4.54
Sr II	-6.00 ± 0.2	-6.30 ± 0.2	3	-5.63	-9.07
Y II	-7.35 ± 0.2	-7.77 ± 0.2	2		-9.80
Zr II	-7.50	-7.70	synth	-7.81	-9.44
Pr III	-7.48	-7.77	1	$-6.69*$	-11.33
Nd III	-6.84 ± 0.35	-7.10 ± 0.34	4	$-7.34*$	-10.54
Eu II	-7.45 ± 0.15	-7.8 ± 0.2	3	-8.15	-11.53
Tb III	-8.0	-8.2	1		-12.14
Dy III	-7.35 ± 0.15	-7.55 ± 0.15	3		-10.94
Er III	-8.05 ± 0.25	-8.30 ± 0.25	3		-11.11
$T_{\rm eff}$	11 900	11 000		11 300	
$\log g$	3.90	3.50		3.20	

* The Pr and Nd abundances in HD 43819 were derived from Pr II and Nd II lines.

of He and Mg, which is typical of magnetic peculiar stars. Thus, despite its weak magnetic field, the chemical anomalies in HD 10221 are significant.

ATMOSPHERIC STRATIFICATION OF CHEMICAL ELEMENTS

The abundance data in Table 3 show that, in general, the spectrum of HD 10221 can be satisfactorily described in terms of models with uniform chemical composition, except for silicon. For both models, we cannot describe the Si II and Si III lines by the same silicon abundance. Of course, the uncertainties in the oscillator strengths play a significant role, but we noticed that the Si II lines with different excitation potentials also require different silicon abundances. That the cores and Stark wings of the strong Si II lines cannot be described in terms of a model with uniform chemical composition is of greatest importance. The observed features of the line profiles suggest the presence of an abundance gradient in the

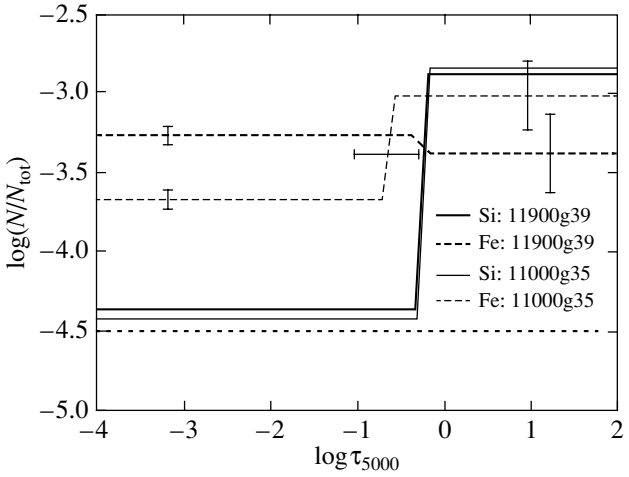

Fig. 3. Silicon (solid lines) and iron (dashed lines) distributions in the atmosphere of HD 10221 for the two atmospheric models under consideration. The errors are shown only for iron (see the text). The solar abundances of both elements are indicated by the dotted line.

atmosphere, abundance stratification (Ryabchikova *et al.* 2003). We computed the stratification of two elements, Si and Fe, in the atmosphere of HD 10221 for both atmospheric models. The distribution of the element was fitted by a step function where the elemental abundance before and after the jump and the position and width of the jump in the atmosphere were varied (see Ryabchikova *et al.* 2005).

In our calculations, we used the profiles of seven Si II lines, two Si III lines, four Fe I lines, eleven Fe II lines, and one Fe III line. The Si II and Fe II lines have lower-level excitation potentials in the ranges 9.8–13.5 (Si II) and 2.7–10.5 eV (Fe II). For the hot 11900g39 model, we obtained an almost uniform iron distribution, at least in the layers where the overwhelming majority of lines originate. For the cooler model, we formally obtained a jump in the iron distribution at a depth of $\log \tau_{5000} = -0.6$. However, the jump is only 0.6 dex, and this is probably attributable to inadequacies in the atmospheric model. For silicon, the jump in the distribution of this element is one and a half orders of magnitude for both models. The silicon and iron distributions in the atmosphere of HD 10221 for both models are shown in Fig. 3. This figure also shows the formal errors in the parameters of the stratification model for iron. The corresponding errors for Si are much smaller; they do not exceed 0.02 dex both for the abundances in the upper and lower atmospheric layers and for the depth of the jump. Our calculations indicate that the jump in the elemental abundance occurs in a narrow range of optical depths near $\log \tau_{5000} = -0.3$; the abundance decreases sharply in the upper atmospheric layers and increases with depth. For the 11900g39 model, Fig. 4 compares the observed Si II and Si III line profiles with the profiles computed for a uniform abundance of $\log(\mathrm{Si}/N_{\mathrm{tot}}) = -3.8$ and for the silicon distribution shown in Fig. 3.

The stratification of chemical elements in the atmospheres of peculiar stars was empirically studied previously by Wade *et al.* (2001) for β CrB (8000g40), Ryabchikova *et al.* (2002) for γ Equ (7700g42), and Ryabchikova *et al.* (2004) for HD 204411 (8400g35), HD 188041 (8800g40), and HD 133792 (9200g36). The jump in the iron abundance decreases in these stars from 3.4 to 1.0 dex with rising effective temperature, and our results for an even hotter star probably confirm this empirical dependence. There is no such dependence for silicon, the jump in the abundance varies within the range 1.5–3 dex, and our derived Si distribution in the atmosphere of HD 10221 also agrees with the empirical stratification for cooler CP stars. It should be noted that HD 204411 and HD 133792, just as HD 10221, are stars with extremely weak magnetic fields, while β CrB and γ Equ have surface magnetic fields of 5400 and 4000 G, respectively. However, all these stars share a common property, slow rotation. Clearly, a magnetic field plays a secondary role in the formation of chemical anomalies, compared to slow rotation.

SURFACE NONUNIFORMITY OF THE CHEMICAL COMPOSITION

HD 10221 exhibits a large photometric variability (Hildebrandt 1975), suggesting a possible nonuniform distribution of chemical elements over the stellar surface. We emphasize that during observations with a high resolution and a high signal-to-noise ratio, certain conclusions about the variability of spectral lines can be reached even if only one spectrum is available. For example, almost all of the rare earth lines are shifted in wavelength with respect to the iron lines, while the chromium lines are slightly narrower than the iron lines.

The rare earth elements in CP stars are known from observational data to concentrate usually near the magnetic poles. Therefore, the presence of photometric variability can serve as evidence for the existence of a dipole magnetic field in the star. Hildebrandt (1975) constructed the photometric dependences using the ephemeris

$$\mathrm{JD(minimum\ light)} = 2\,440\,973.30 + 3.16E.$$

Unfortunately, the rotation period is not accurate enough to calculate the phase of the period at which the magnetic field and the chemical composition were estimated.

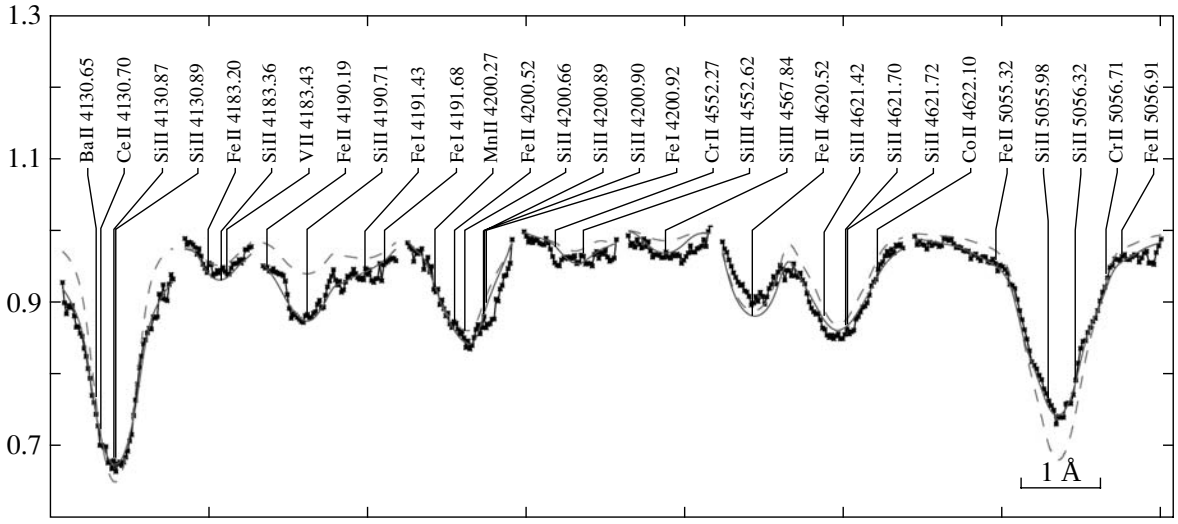

Fig. 4. Comparison of the observed (dots) and synthetic Si II and Si III line profiles computed for the 11900g39 atmospheric model for a uniform silicon abundance (dashed line) and the silicon distribution shown in Fig. 3 (solid line). The axes are the same as those in Fig. 1.

Based on the two assumed temperatures $T_{eff} = 11\,000$ and $11\,900$ K and the absolute magnitude $M_V = -0.2$ (Gomez *et al.* 1998) estimated from the Hipparcos parallax using bolometric corrections from Straizis and Kuriliene (1981), we determined the bolometric absolute magnitudes, $M_{bol} = -0.7 \ldots -0.9$, which yields the stellar radii of $3.3R_\odot$ and $3.1R_\odot$, respectively. The mean inclination of the rotation axis to the line of sight was found from the standard formula for the equatorial velocity $v = 50.6R/P$ (P is the rotation period) and $v_e \sin i = 27 \pm 2$ km s^{-1} to be $i = 32^\circ \pm 5^\circ$.

CONCLUSIONS

Our abundance analysis for HD 10221 has shown that this star have anomalies typical of SrCrEu stars, although its effective magnetic field is weak, $B_e < 100$ G. The chemically peculiar star HD 43819, in which the magnetic field is at least an order of magnitude stronger, have similar chemical anomalies. The atmosphere of HD 10221 also exhibits a stratification of certain chemical elements, for example, silicon, which may be considered as evidence for the stability of the atmosphere, irrespective of the presence of a strong magnetic field. Consequently, the magnetic-field strength is not a determining factor in the formation mechanism of chemical anomalies in the atmospheres of CP stars. This has already been noted in our previous paper (Glagolevskii and Chountonov 2002), where we showed that there is no clear correlation between the strength of chemical anomalies and the magnetic field. We can speak with certainty only about the following trend: on average, the stronger the magnetic field, the stronger the chemical anomalies.

The star that we studied is no exception (see Glagolevskii and Chountonov 2002; Aurière *et al.* 2005). In any case, it is important that CP stars with weak magnetic fields have low rotational velocities and typical chemical anomalies and photometric variability. This is a problem for the theories that attempt to explain the origin of chemically peculiar stars.

ACKNOWLEDGMENTS

This work was supported in part by the Russian Foundation for Basic Research (project no. 03-02-16342), the federal Astronomy science and technology program, and a grant for support of leading scientific schools (no. NSh-162.2003.2)

REFERENCES

1. H. A. Abt and N. I. Morrell, Astrophys. J., Suppl. Ser. **99**, 135 (1995).
2. R. Aurière, J. Silvester, G. A. Wade, *et al.*, in *Proc. of Stellar Magnetic Fields* (Spec. Astrophys. Obs., 2005) (in press).
3. H. W. Babcock, Astrophys. J., Suppl. Ser. **3**, 141 (1958).
4. L. A. Balona, Mon. Not. R. Astron. Soc. **268**, 119 (1994).
5. P. S. Barklem, N. Piskunov, and O'Mara, Astron. Astrophys. **363**, 1091 (2000).
6. F. Castelli, R. G. Gratton, and R. L. Kurucz, Astron. Astrophys. **318**, 841 (1997).

7. Yu. V. Glagolevskii, V. D. Bychkov, I. Kh. Iliev, *et al.*, Pis'ma Astron. Zh. **8**, 26 (1982) [Sov. Astron. Lett. **8**, 12 (1982)].
8. Yu. V. Glagolevskii, I. I. Romanyuk, N. M. Chunakova, and V. G. Shtol', Astrofiz. Issled., Izv. Spets. Astrofiz. Obs. **23**, 37 (1986).
9. Yu. V. Glagolevskii, Bull. Spec. Astrophys. Obs. **53**, 33 (2002).
10. Yu. V. Glagolevskii and G. A. Chuntonov, Astrofiz. **45**, 499 (2002) [Astrophys. **45**, 408 (2002)].
11. A. E. Gomez, X. Luri, S. Grenier, *et al.*, Astron. Astrophys. **336**, 953 (1998).
12. N. Grevesse and A. J. Sauval, Space. Sci. Rev. **85**, 161 (1998).
13. B. Hauck and M. Mermilliod, Astron. Astrophys., Suppl. Ser. **129**, 431 (1998).
14. G. Hildebrandt, Astron. Nachr. **296**, 277 (1975).
15. H. Holweger, AIP Conf. Proc. **598**, 23 (2001).
16. A. Kaiser, Commun. Asteroseismol. (2005) (in press).
17. D. O. Kudryavtsev, *Magnetic Fields of Chemically Peculiar and Related Stars*, in *Proc. Int. Conf.,* Ed. by Yu. V. Glagolevskii and I. I. Romanyuk (Russ. Acad. Sci., Moscow, 2000), p. 84.
18. F. Kupka, N. Piskunov, T. A. Ryabchikova, *et al.*, Astron. Astrophys., Suppl. Ser. **138**, 119 (1999).
19. R. L. Kurucz, CD-ROM's 18–23 (1993).
20. Z. Lopez-Garcia and S. J. Adelman, Astron. Astrophys., Suppl. Ser. **107**, 353 (1994).
21. T. Moon and M. Dworetsky, Mon. Not. R. Astron. Soc. **217**, 305 (1985).
22. R. Napiwotzki, D. Schönberner, and V. Wenske, Astron. Astrophys. **268**, 653 (1993).
23. N. Piskunov, *Stellar Magnetism*, Ed. by Yu. V. Glagolevskij and I. I. Romanyuk (Nauka, St. Petersburg, 1992), p. 92.
24. A. J. J. Raassen and P. H. M. Uylings, Astron. Astrophys. **340**, 300 (1998).
25. I. Ribas, C. Jordi, J. Torra, and A. Gimenez, Astron. Astrophys. **327**, 207 (1997).
26. F. Royer, S. Grenier, M.-O. Baylac, *et al.*, Astron. Astrophys. **393**, 897 (2002).
27. T. A. Ryabchikova, N. Piskunov, H. C. Stempels, *et al.*, Phys. Scr., T **83**, 1962 (1999).
28. T. Ryabchikova, N. Piskunov, O. Kochukhov, *et al.*, Astron. Astrophys. **384**, 545 (2002).
29. T. Ryabchikova, G. A. Wade, and F. LeBlanc, *IAU Symp. No. 210: Modelling of Stellar Atmospheres* Ed. by N. Piskunov, W. W. Weiss, and D. F. Gray, (Publ. Astron. Soc. Pac., 2003), p. 301.
30. T. Ryabchikova, F. Leone, O. Kochukhov, and S. Bagnulo, *Proc. IAU Symp. No. 224: The A-Star Puzzle*, Ed. by J. Zverko, W. W. Weiss, J. Žižňovský, and S. J. Adelman (Cambridge Univ. Press, 2004) (in press).
31. T. Ryabchikova, F. Leone, and O. Kochukhov, Astron. Astrophys. (2005) (in press).
32. K. Stępień, Astron. Astrophys. **353**, 227 (2000).
33. V. Straizis and G. Kuriliene, Astrophys. Space Sci. **80**, 353 (1981).
34. A. Uesugi and I. Fukuda, *Revised Catalogue of Stellar Rotational Velocities* (Univ. Kyoto, Kyoto, 1982).
35. G. A. Wade, T. A. Ryabchikova, S. Bagnulo, and N. Piskunov, Astron. Soc. Pac. Conf. Ser. **248**, 341 (2001).
36. Z. G. Zhang, S. Svanberg, P. Palmeri, *et al.*, Mon. Not. R. Astron. Soc. **334**, 1 (2002).

Translated by V. Astakhov

Astronomy Letters, Vol. 31, No. 5, 2005, pp. 335–339. Translated from Pis'ma v Astronomicheskiĭ Zhurnal, Vol. 31, No. 5, 2005, pp. 372–377.

Analysis of Magnetic Field Measurements for T Tau

D. A. Smirnov[1]*, M. M. Romanova[2], and S. A. Lamzin[1]

[1] *Sternberg Astronomical Institute, Universitetskiĭ pr. 13, Moscow, 119992 Russia*

[2] *Department of Astronomy, Cornell University, 410 Space Sciences Building, Ithaca, NY 14853-680, USA*

Received October 29, 2004

Abstract—The presence of hot spots on the surface of T Tau attributable to mass accretion from the protoplanetary disk is shown to have virtually no effect on the accuracy of estimating the magnetic field strength for this star. By comparing the magnetic field strengths for T Tau at the photospheric level measured by various methods, we found that if the angle i at which we see T Tau does not exceed 10°, then the magnetic field of the star could be dipolar with the angle between the dipole axis and the rotation axis of the star $\simeq 85°$. If, however, it later emerges that $i > 10°$, its magnetic field is essentially nondipolar and/or nonstationary. © *2005 Pleiades Publishing, Inc.*

Key words: *individual stars: T Tau, T Tau stars, magnetic field—disk accretion.*

INTRODUCTION

T Tauri stars (TTSs) are young ($t < 10^7$ yr) low-mass ($M \leq 2M_\odot$) stars that are at the stage of gravitational contraction toward the main sequence. T Tau belongs to the so-called classical T Tauri stars (CTTSs), whose activity is attributable to mass accretion from the (protoplanetary) disk. The magnetic field of young stars not only determines the pattern of TTS activity, but also plays a crucial role in the evolution of the angular momentum of the star. Therefore, the strength and topology of the magnetic field is one of the main questions in the physics of young stars. At present, the magnetic field strength is known for less than ten TTSs, because the field is difficult to measure for these objects.

Since the magnetic field changes the equivalent widths of spectral lines depending on the Landè factor, Guenther *et al.* (1999) and Johns-Krull *et al.* (2001) found, in particular, that the surface-averaged magnetic field strength of T Tau is $B >$ 2 kG. On the other hand, Smirnov *et al.* (2003, 2004) inferred from spectropolarimetric observations that the surface-averaged longitudinal (i.e., along the line of sight) magnetic field component of T Tau was $B_{||} \simeq +150 \pm 50$ G in 1996 and 2002 and $\simeq +50 \pm 30$ G in 2003, i.e., it was smaller than B by more than an order of magnitude. The possible causes of such a large discrepancy are considered below.

*E-mail: danila@sai.msu.ru

THE EFFECT OF ACCRETION ON THE ACCURACY OF ESTIMATING THE OBSERVED B AND $B_{||}$

The calculations by Romanova *et al.* (2003) have confirmed that in the case of disk accretion onto a young star with a dipole magnetic field, matter falls mainly near the magnetic poles, i.e., to the region with the strongest magnetic field. The accreted matter heats up the stellar surface, and if the contribution of hot regions to the formation of a spectral line is small, then the mean values of B and $B_{||}$ obtained by analyzing this line will be underestimated. Let us estimate the magnitude of this effect.

The effective temperature $T_{\rm eff}$ of a star in the accretion zone can be estimated from the relation

$$\sigma T_*^4 + \frac{\rho V^3}{2} \simeq \sigma T_{\rm eff}^4, \qquad (1)$$

where T_* is the effective temperature of the star without accretion, and ρ and V are the density and velocity of the infalling matter, respectively. The regions with $T > T_*$ yield a spectrum different from that of the star, and, below, to take into account this fact, we assume that the absorption lines of interest are not formed in these regions at all.

The distributions of the parameters $\rho = \rho(\theta, \varphi)$ and $V = V(\theta, \varphi)$ on the stellar surface within the accretion zone were taken from the paper by Romanova *et al.* (2003) and were used to estimate the dependence $T_{\rm eff}(\theta, \varphi)$ by means of formula (1), where we set $T_* = 5250$ K (White and Ghez 2001). Romanova *et al.* (2003) performed their three-dimensional MHD

1063-7737/05/3105-0335$26.00

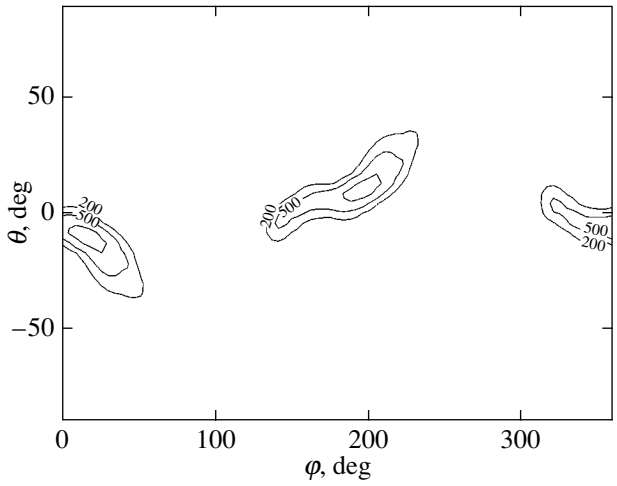

Fig. 1. Distribution of the temperature excess ΔT over the surface of a star with a dipole magnetic field whose axis is inclined at $\alpha = 75^\circ$ to the rotation axis (for details, see the text). The innermost isoline corresponds to $\Delta T = 1000$ K. The longitude and latitude are plotted along the horizontal and vertical axes, respectively.

calculations for various angles α between the magnetic and rotation axes of the star[1]; Fig. 1 shows the temperature distribution in the accretion zone for $\alpha = 75^\circ$. More precisely, this figure shows the $\Delta T(\theta, \varphi) = T_{\rm eff} - T_*$ isolines that characterize the excess heating in the accretion zone. Similar dependences for other angles α can be easily constructed from the data given in the paper by Romanova *et al.* (2004).

The observed $B_{||}$ and B inferred from photospheric lines are the values averaged over the visible stellar hemisphere:

$$B = \frac{1}{2\pi R_*^2}\int\limits_{S_*} B(\theta,\varphi)\cos\beta dS, \qquad (2)$$

$$B_{||} = \frac{1}{2\pi R_*^2}\int\limits_{S_*} B(\theta,\varphi)\cos\beta\cos\gamma dS.$$

Let us introduce a spherical coordinate system whose center coincides with the center of the star, the $\theta = 0$ axis is the rotation axis of the star characterized by the unit vector ω, and the plane passing through the vector ω and the unit vector **l** directed from the stellar center to the Earth serves as the $\varphi = 0$ plane. Let **n** be a unit vector along the normal to the stellar surface at a given point, and **B** be the magnetic field vector at this point. Then, in relations (2), $R_*^{-2}dS = \sin\theta d\theta d\varphi$, β is the angle between the vectors **n** and **l**, and γ is the angle between the vectors **l** and **B**, with

$$\cos\beta = \sin i\sin\theta\cos\varphi + \cos i\cos\theta,$$

$$\cos\gamma = \mathbf{l}\cdot\frac{\mathbf{B}}{B},$$

where i is the angle between the rotation axis of the star and the line of sight.

In this coordinate system, the quantity $\mathbf{B}(\theta,\varphi)$ varies with time t due to the rotation of the star. Let us assume that the star has a dipole magnetic field, i.e.,

$$\frac{\mathbf{B}}{B_0} = \frac{3\mathbf{n}(\boldsymbol{\mu}\mathbf{n}) - \boldsymbol{\mu}}{2},$$

where B_0 is the magnetic field strength *at the pole* of the dipole, and $\boldsymbol{\mu}$ is a unit vector along the magnetic axis. One parameter, the phase ψ ($0 \le \psi < 1$) that characterizes the displacement of the magnetic pole with respect to the $\varphi = 0$ plane, will then suffice to describe the dependence $\mathbf{B}(t)$ at each point. Accretion distorts the initial (dipole) magnetic field of the star, but the resulting field near the stellar surface differs from the initial field by no more than 1% (Romanova *et al.* 2003).

To estimate the effect of spots on the measured $B_{||}$ and B, we calculated the observed $B_{||}$ and B using formula (2) for three cases: (1) ignoring hot spots (i.e., over the entire visible surface); (2) without the part of the stellar surface occupied by the accretion zone with $\Delta T > 200$ K; and (3) without the region with $\Delta T > 1000$ K.

As an example, Fig. 2 shows how $B_{||}/B_0$ varies with rotation phase of the star ψ in each of these cases for $\alpha = 75^\circ$ and four angles i: 10°, 30°, 60°, and 90°. Figure 3 shows a similar dependence of B/B_0 on ψ for the same values of α and i. We see from these figures that the difference between the curves does not exceed 10–15% for all values of i. A similar result is also obtained for other values of α. This means that, when hot spots are disregarded, the errors in B and $B_{||}$ do not exceed 15%, which is smaller than the current accuracy of measuring these parameters for young stars. The relatively small (~10%) fraction of the stellar surface within which the bulk of the accretion energy is released is responsible for such a small effect (Romanova *et al.* 2003, 2004).

ESTIMATING THE PARAMETERS OF THE MAGNETIC FIELD OF T TAU UNDER THE ASSUMPTION OF ITS DIPOLE PATTERN

If the magnetic field of T Tau is dipolar and stationary, then the difference between the observed $B_{||}$ and B by more than an order of magnitude can be explained by the fact that the angle δ between the dipole

[1] In addition, Romanova *et al.* (2003) assumed the magnetic field strength at the pole of the star and the accretion rate to be $B_0 \simeq 2.1$ kG and $\dot{M}_{\rm ac} \simeq 2\times10^{-7}\ M_\odot\ {\rm yr}^{-1}$, respectively.

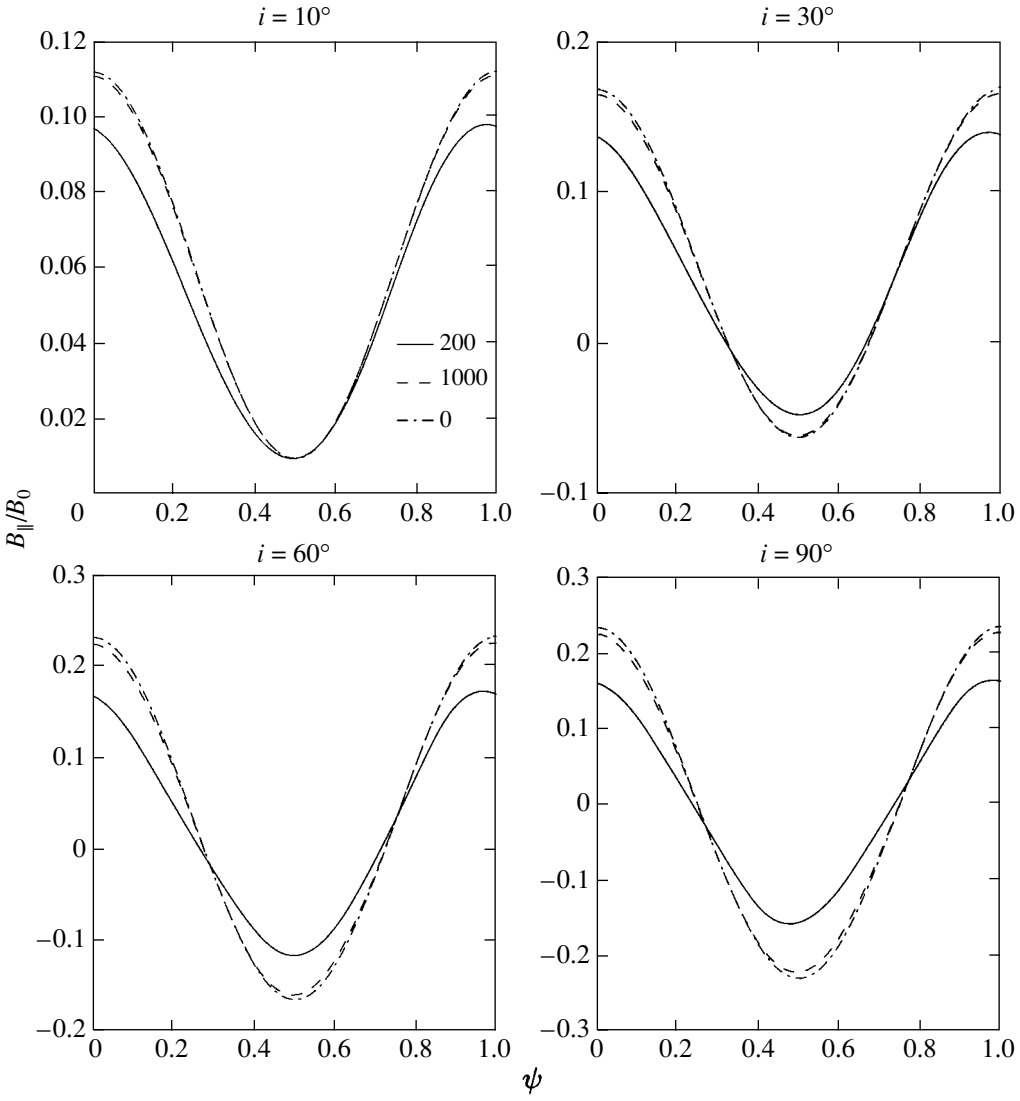

Fig. 2. Mean longitudinal magnetic field component $B_{||}$ versus rotation phase ψ of the star for $\alpha = 75°$ and various angles i. The dashed line corresponds to the case where the entire stellar surface is considered (there are no hot spots). The solid and dash–dotted lines correspond to the stellar surface without regions with $\Delta T > 200$ K and $\Delta T > 1000$ K, respectively.

axis and the line of sight was close to 90° during our observations. At $\delta = 90°$, the field components $B_{||}$ directed toward and away from the observer cancel each other out; therefore, the observed $B_{||}$ must be equal to zero in this case. Let us consider this question from a quantitative point of view based on the results of our observations.

Let us assume that the magnetic field of the star is dipolar and specify three parameters that characterize it: B_0, i, and α. At fixed values of these parameters, the observed B and $B_{||}$ vary with ψ, as, for example, in Figs. 2 and 3. For a given set of parameters, the probability p of finding B from the interval $B^{\rm obs} \pm 3\sigma$ at an arbitrary time is equal to the length of the phase interval in which $|B - B^{\rm obs}| < 3\sigma$, where σ is the observational error. The probability of finding $B_{||}$ in the interval $|B_{||} - B_{||}^{\rm obs}| < 3\sigma$ can be determined in a similar way.

Guenther *et al.* (1999) and Johns-Krull *et al.* (2001) obtained $B = 2.3 \pm 0.15$ kG for T Tau, whereas our observations yielded the following $B_{||}$ estimates: $+150 \pm 50$ in 1996 and 2002 and $+50 \pm 30$ G in 2003. If the parameters B_0 and α did not change with time (i.e., the magnetic field of the star was stationary), then the difference between the measured B and $B_{||}$ should be attributed to the fact that the measurements were made at different phases ψ. For each triple of parameters B_0, i, and α, we can then determine the probability $P = p_1 p_2 p_3 p_4 p_5$ that the

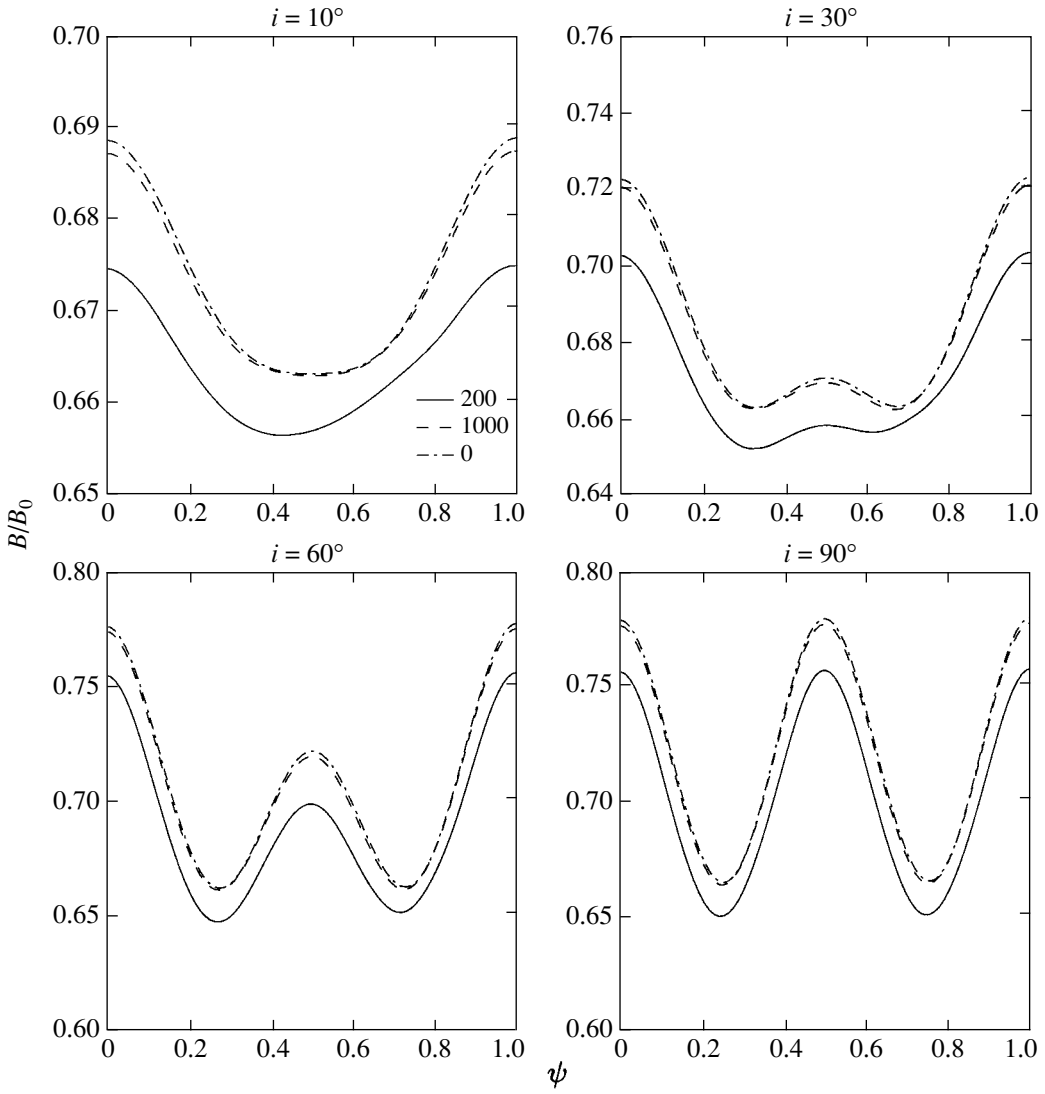

Fig. 3. Same as Fig. 2 for the mean magnetic field strength B.

above values were obtained for two measurements of B and three measurements of $B_{||}$.

We performed such calculations for the following ranges of parameters: B_0 from 1.5 to 5 kG, $0° \le \alpha \le 90°$, and $0° \le i \le 60°$. In choosing the i range, we took into account that $i = 29°^{+10°}_{-15°}$ for T Tau (Akeson *et al.* 2002). Our calculations showed the following:

(1) For any α and i from the ranges under consideration, the probability P is nonzero only for 3 kG $< B_0 <$ 4.3 kG. This is a natural result, since the strength of a dipole magnetic field on the stellar surface changes from B_0 at the pole to $B_0/2$ on the equator. Therefore, the mean B must also lie within the range $(B_0/2, B_0)$ for any orientation of the dipole with respect to the observer.

(2) The pattern of the dependence $P = P(\alpha, i)$ is essentially identical for all B_0 from the admissible range. As an example, Fig. 4 shows the dependence $P = P(\alpha, i)$ calculated for $B_0 = 3.5$ kG (the lines of equal probability consist of rectilinear segments, because $P(\alpha, i)$ was calculated for the angles α and i at 5°) steps.

We see from the figure that for $\alpha < 80°$ and/or $i > 10°$, the probability of obtaining the magnetic field strengths for T Tau that we found is less than 0.2; i.e., such values of the parameters seem unlikely. We emphasize once again that this result is virtually independent of the actual value of B_0 for this star. Thus, the following two assertions can be made:

(1) If future (e.g., VLTI) observations show that the rotation axis of T Tau is inclined at more than 10° to the line of sight, then the measured B and $B_{||}$ imply that the magnetic field of this star near its surface differs significantly from the dipole field.

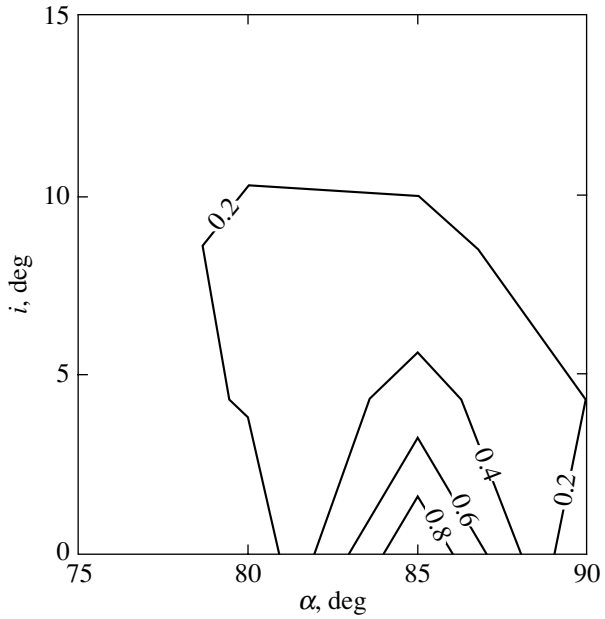

Fig. 4. Lines of equal probability $P(\alpha, i) = \text{const}$ in the case where $B_0 = 3.5$ kG. For details, see the text.

It is pertinent to recall that Dudorov (1995) argued theoretically that the TTS magnetic field must have a nearly quadrupole configuration.

(2) If the inclination proves to be $i < 10°$, then the observations are consistent with the hypothesis that T Tau has a dipole magnetic field with the dipole axis inclined at $\simeq 85°$ to the rotation axis.

Note once again that these assertions are valid only in terms of the hypothesis that the magnetic field of the star is stationary: otherwise, comparing B and $B_{||}$ measured nonsimultaneously makes no sense at all.

CONCLUSIONS

The calculations by Romanova *et al.* (2003) show that in the case of disk accretion onto an inclined dipole with B_0 and $\dot{M}_{\rm ac}$ typical of CTTSs, the difference between the resulting field and the dipole field near the stellar surface is negligible. On the other hand, we showed above that if the magnetic field of the star is dipolar, then the excess heating of the stellar surface in the accretion zone has virtually no effect on the accuracy of estimating the mean B and $B_{||}$ obtained from observations.

This implies that a comparison of the observed B and $B_{||}$ at the photospheric level can yield information about the magnetic field configuration of young stars: whether it is dipolar or more complex. We showed above that the available B and $B_{||}$ estimates for T Tau could be reconciled in terms of the following alternative: either the star's magnetic field is essentially nondipolar or it is dipolar, but the dipole axis is inclined at about 85° to the line of sight. It will be possible to make the final choice between these alternatives once it is established from (interferometric) observations whether the inclination of the rotation axis of T Tau to the line of sight exceeds 10°. More precisely, this alternative follows from observations only if the magnetic field of the star is stationary. The question as to whether the magnetic fields of young stars are stationary is of interest per se and requires further observational tests.

ACKNOWLEDGMENTS

This work was performed as part of the research on young stars supported by the Russian Foundation for Basic Research (project no. 02-02-16070), INTAS (grant no. 03-51-6311), NASA (grant nos. NAG5-13220 and NAG5-13060), and NSF (grant no. AST-0307817).

REFERENCES

1. R. L. Akeson, D. R. Ciardi, G. T. van Belle, and M. J. Creech-Eakman, Astrophys. J. **566**, 1124 (2002).
2. A. E. Dudorov, Astron. Zh. **72**, 884 (1995) [Astron. Rep. **39**, 790 (1995)].
3. E. Guenther, H. Lehmann, J. P. Emerson, and J. Staude, Astron. Astrophys. **341**, 768 (1999).
4. C. M. Johns-Krull, J. Valenti, S. H. Saar, and A. P. Hatzes, ASP Conf. Ser. **223**, 521 (2001).
5. M. M. Romanova, G. V. Ustyugova, A. V. Koldoba, *et al.*, Astrophys. J. **595**, 1009 (2003).
6. M. M. Romanova, G. V. Ustyugova, A. V. Koldoba, and R. V. E. Lovelace, Astrophys. J. **610**, 920 (2004).
7. D. A. Smirnov, S. N. Fabrika, S. A. Lamzin, and G. G. Valyavin, Astron. Astrophys. **401**, 1057 (2003).
8. D. A. Smirnov, S. A. Lamzin, S. N. Fabrika, and G. A. Chuntonov, Pis'ma Astron. Zh. **30**, 506 (2004) [Astron. Lett. **30**, 456 (2004)].
9. R. J. White and A. M. Ghez, Astrophys. J. **556**, 265 (2001).

Translated by A. Dambis

Astronomy Letters, Vol. 31, No. 5, 2005, pp. 340–349. Translated from Pis'ma v Astronomicheskiĭ Zhurnal, Vol. 31, No. 5, 2005, pp. 378–387.

Relativistic Effects and Solar Oblateness from Radar Observations of Planets and Spacecraft

E. V. Pitjeva*

Institute of Applied Astronomy, Russian Academy of Sciences, nab. Kutuzova 10, St. Petersburg, 191187 Russia

Received September 3, 2004

Abstract—We used more than 250 000 high-precision American and Russian radar observations of the inner planets and spacecraft obtained in the period 1961–2003 to test the relativistic parameters and to estimate the solar oblateness. Our analysis of the observations was based on the EPM ephemerides of the Institute of Applied Astronomy, Russian Academy of Sciences, constructed by the simultaneous numerical integration of the equations of motion for the nine major planets, the Sun, and the Moon in the post-Newtonian approximation. The gravitational noise introduced by asteroids into the orbits of the inner planets was reduced significantly by including 301 large asteroids and the perturbations from the massive ring of small asteroids in the simultaneous integration of the equations of motion. Since the post-Newtonian parameters and the solar oblateness produce various secular and periodic effects in the orbital elements of all planets, these were estimated from the simultaneous solution: the post-Newtonian parameters are $\beta = 1.0000 \pm 0.0001$ and $\gamma = 0.9999 \pm 0.0002$, the gravitational quadrupole moment of the Sun is $J_2 = (1.9 \pm 0.3) \times 10^{-7}$, and the variation of the gravitational constant is $\dot{G}/G = (-2 \pm 5) \times 10^{-14}$ yr^{-1}. The results obtained show a remarkable correspondence of the planetary motions and the propagation of light to General Relativity and narrow significantly the range of possible values for alternative theories of gravitation. © *2005 Pleiades Publishing, Inc.*

Key words: *celestial mechanics, cosmology, Sun.*

INTRODUCTION

Radar observations of planets began in 1961 and have been widely used in astronomical practice ever since. High-precision radar measurements spanning a time interval of more than forty years allow not only the orbital elements of the planets, but also other constants of the planetary theory, including the relativistic parameters, to be determined with a high accuracy.

Of the three main tests of General Relativity in the Solar system (the secular motions of the planetary perihelia, the signal delay, and the deflection of light in a gravitational field), the first two tests have been performed using radar observations of planets and spacecraft.

The main and best determined relativistic effect in the Solar system is the secular motion of Mercury's perihelion that was discovered by Le Verrier in 1859. For him, this was a major problem of the discrepancy between theoretical predictions and observations, and it was explained in 1915 by Einstein's theory of General Relativity. However, the secular motion of Mercury's perihelion is known to depend on a linear combination of the post-Newtonian parameters (β, γ) and the gravitational quadrupole moment of the Sun (J_2). Papers (see, e.g., Pireaux and Rozelot 2003) arguing that only this combination rather than the three parameters themselves could be determined from current observations have appeared in recent years. However, the post-Newtonian parameters and the solar oblateness cause different secular and periodic perturbations both for different orbital elements (and not just for the perihelia) and for different planets. In addition, the parameter γ can also be determined from Shapiro's effect, which allows all three parameters to be estimated. Since these parameters can in most cases be obtained by analyzing the secular variations of orbital elements, the errors of their determination decrease with increasing time interval of observations. At the same time, the errors in the secular variation of the gravitational constant ($\dot{G}/G$), one of the most interesting parameters, decrease even faster: as the square of the time interval. This allows $\dot{G}/G$ to be estimated, thereby basically verifying the strong equivalence principle, since many theories of gravitation predict a variation of the locally measured Newtonian gravitational constant with time on the evolutionary scale of the Universe.

Some of the recent post-Newtonian-parameter

*E-mail: evp@quasar.ipa.nw.ru

determinations, e.g., $\gamma = 1.000021 \pm 0.000023$, from Cassini radar observations (Bertotti *et al.* 2003) reach a high accuracy. However, the improvement in quality and the increase in the number of current radar observations of planets and spacecraft as well as the increase in the time interval of observations have allowed not only γ, but also β, $\dot{G}/G$, and the gravitational quadrupole moment of the Sun to be estimated independently and from other data.

THE METHOD, EPM EPHEMERIDES

We used the following method to calculate the relativistic parameters and the solar oblateness. First, we constructed a numerical theory for the motion of the planets and the Moon, EPM2004—Ephemerides of Planets and the Moon (Pitjeva 2004, 2005), by using more than 317 000 observations (1913–2003) of various types. These included radiometric measurements of planets and spacecraft, astrometric CCD observations of the outer planets and their satellites, and meridian and photographic observations. Apart from the planetary ephemerides, we also constructed the ephemerides of the orbital and rotational motion of the Moon that were improved by processing the 1970–2003 LLR observations (Krasinsky 2002). The ephemerides of the planets and the Moon were constructed by the simultaneous numerical integration of the equations of motion for all planets, the Sun, the Moon, 301 largest asteroids, rotation of the Earth and the Moon, including the perturbations from the solar oblateness and the asteroid ring that lies in the plane of the ecliptic and consists of the remaining smaller asteroids. The equations of motion for bodies were taken in the post-Newtonian approximation in the Schwarzschild gravitational field described by a three-parameter (α, β, γ) metric in a harmonic coordinate system with $\alpha = 0$; all versions of the ephemerides were constructed for General Relativity: $\beta = \gamma = 1$. The general equations of motion for bodies in a nonrotating barycentric coordinate system are

$$\ddot{\mathbf{r}}_i = A + B + C + D,$$

where A are the Newtonian gravitational accelerations, B are the relativistic terms (Newhall *et al.* 1983), C are the terms attributable to the solar oblateness, and D are the terms attributable to the asteroid ring (Krasinsky *et al.* 2002).

Below, we provide brief information about the EPM2004 theory and its construction (Pitjeva 2005).

First, a physical model that includes all of the significant factors and that adequately reflects the actual planetary motions underlies this theory. In particular, including the perturbations from the several largest asteroids, as was done in previous versions of our EPM or Jet Propulsion Laboratory (JPL) DE ephemerides, was shown (Krasinsky *et al.* 2001; Standish and Fienga 2002) to be insufficient. In EPM2004, the gravitational perturbations that are introduced into the orbits of the inner planets by asteroids and that make it difficult to determine the parameters were reduced significantly by including 301 large asteroids and the perturbations from the massive ring of small asteroids in the simultaneous integration of the equations of motion and by estimating their masses when processing the observations.

Second, the accuracy of the numerical integration itself was checked by comparing the results of the forth and back integrations on a hundred-year time interval. The emerging errors were at least an order of magnitude smaller than the observational errors. Thus, the accuracy of the ephemerides is determined mainly by the accuracy of the observations and their reductions.

Third, producing the ephemerides is an iterative process of comparing the constructed ephemerides with observations, improving the parameters by the least-squares method (LSM), introducing these in the theory, and constructing a new version of the ephemerides.

In the main improvement of the planetary part of the EPM2004 ephemerides, we determined about 200 parameters: the orbital elements of all planets and the 13 satellites of the outer planets the observations of which were used to improve the orbits of these planets; the astronomical unit in kilometers; three orientation angles of the ephemerides relative to the International Celestial Reference Frame (ICRF); the rotation parameters of Mars (two orientation angles of the equator of Mars relative to its orbit and their secular variations, the velocity, and eight coefficients of the seasonal rotation terms of the Martian axis) and the coordinates of three landers on the Martian surface; the masses of the bodies (Jupiter and the six asteroids that perturb Mars most strongly), the mean densities for three taxonomic classes of asteroids (C, S, M), the mass and radius of the asteroid ring, the ratio of the Earth's and Moon's masses; the gravitational quadrupole moment of the Sun (J_2) and twelve parameters of the solar corona for different conjunctions with the Sun; eight coefficients of Mercury's topography and the corrections to the level surfaces of Venus and Mars relative to which the topographies of these planets were calculated; five parameters for calculating the additional phase effect in the optical observations of the outer planets; and the constant shifts for six groups of observations that were interpreted as systematic errors or calibration errors of the instrumentation.

Once the EPM2004 ephemerides were constructed from all radar observations of the inner planets, spacecraft passing by or orbiting these planets, and

Martian landers, we improved the parameters, including the relativistic ones (β, γ, $\dot{G}/G$, the secular motions of the planetary perihelia), by the LSM.

The partial derivatives of the observed quantities (e.g., the delay time τ) with respect to the parameters being improved, $\frac{\partial\tau(t)}{\partial q(t_0)}$, must be known to determine the parameters of the theory by the LSM. In this case, the expression $\frac{\partial\tau(t)}{\partial s(t)}\frac{\partial s(t)}{\partial q(t_0)}$ is commonly used, since calculating the derivatives of the observed quantities with respect to the coordinates and velocities or orbital elements of the object $s(t)$ using the analytical formulas of the two-body problem involves no difficulty. At the same time, the derivatives $\frac{\partial s(t)}{\partial q(t_0)}$ are calculated either analytically or by integrating the variational equations. The derivative $\frac{\partial\tau(t)}{\partial\dot{G}/G}$ is calculated via the partial derivatives of τ with respect to the differences and sums of the mean longitudes of the observed object and the Earth. We derived expressions for the partial derivatives of the orbital elements with respect to the post-Newtonian parameters (β and γ) using the analytical formulas for the relativistic perturbations of the elements, including the secular and principal periodic terms, given in the monograph by Brumberg (1972). The derivative $\frac{\partial\tau(t)}{\partial\gamma}$ calculated from Shapiro's effect should also be added for γ.

Thus, improving the parameters can be reduced to the following:

(1) Numerical integration of the equations of motion for the planets and some of the partial derivatives;

(2) Computing the model observations (time delays) from the produced ephemerides for each time of observations, calculating the residuals and the required partial derivatives;

(3) Obtaining the values of the parameters being determined and deriving the residuals of the observations after the improvement.

As experience shows, the formal accuracy of determining the parameters by the LSM is overly optimistic. The actual accuracy could be an order of magnitude lower due to the deviation of the distribution of observations from a Gaussian law and due to the systematic errors in the observations, often of an unknown nature. The actual accuracies of the parameters given below were estimated by comparing the values obtained in dozens of different test LSM solutions that differed by the sets of observations, their weights, and the sets of parameters included in the solution.

OBSERVATIONS, THEIR REDUCTION AND ERRORS

We used all the available radar observations of planets (58 116, 1961–1997), spacecraft and landers (195 271, 1971–2003) that were retrieved from the JPL database (http:/ssd.jpl.nasa.gov/iaucomm4/) created and maintained by Dr. Standish and that were supplemented by series of American and Russian radar observations of planets in the period 1961–1995 taken from different sources. The Russian radar observations of planets together with references to the sources are stored at the site of the Institute of Applied Astronomy, Russian Academy of Sciences, //www.ipa.nw.ru/ PAGE/DEPFUND/LEA/ENG/englea.htm. A brief description of all astrometric radar observations can be found in Table 2 from Pitjeva (2005).

The accuracy of the first time-delay (τ) measurements for planets performed in 1961–1962 was 200–500 μs. The accuracy of the 1964–1969 measurements was higher (30 μs). The current accuracy of the radar observations of planets and spacecraft reaches a few hundredths of a microsecond, which corresponds to an error of several meters.

The reductions of the radar observations, including the relativistic corrections—the delay of radio signals near the Sun (Shapiro's effect) and the transition from the coordinate time, the argument of the ephemerides, to the observer's proper time as well as the delay of radio signals in the Earth's troposphere and in the solar coronal plasma,—are well known and were described, for example, by Standish (1990). The observations of Mars and Venus were corrected for topography using the currently available hypsometric maps of the surfaces of these planets and the representation of the topography as a decomposition into spherical harmonics of degrees 16–18. Details on the corrections for the topographies of Venus and Mars can be found in our previous paper (Pitjeva 1996). The topography of Mercury was represented as a decomposition into spherical harmonics up to the second order inclusive; the harmonic coefficients were determined from Mercury's radar observations (Pitjeva 2000). The shortcomings of the reduction include the inability to allow for the rapid change of the surface relief using the harmonics of degrees 16–18 and the limited size of the grid cell in the correction for the surface topography using hypsometric maps. Therefore, unfortunately, the topography errors remain in the observations of planets and are ~100 m. Accordingly, high-precision observations of spacecraft orbiting planets and Martian landers, which are free from these topography errors, are of particularly great importance.

The time delay τ for the Viking-1 and -2 landers on Mars were measured at JPL in the period 1976–1982.

For 20 years, these measurements had been most accurate (an *a priori* accuracy of 7 m) among the positional observations of the major planets; in 1997, the new Pathfinder Martian lander was observed for three months. The differenced range $d\tau$ was measured simultaneously with the time delay. P. Wimberly managed to restore the differenced range for the Viking-1 lander observations in 1976–1978. To compute the lander positions on the Martian surface in the reference frame of the ephemerides, it was necessary to use a theory of the Martian rotation that included not only the precession and nutation of the Martian axis, but also the seasonal terms in the Martian rotation (Pitjeva 1999). The lander observations allowed not only the orbital elements of the Earth and Mars to be accurately determined, but also the Martian rotation parameters and, in particular, such an important (for understanding the geophysics of Mars) parameter as the Martian precession rate. Since the orbit of Mars is perturbed by Jupiter and asteroids, these observations can also be used to improve the masses of Jupiter and the largest asteroids.

The observations of Martian orbiters, Mariner-9 (1971–1972), Mars Global Surveyor (MGS, 1998–2003), and Odyssey (2002–2003), are given in the form of normal points of distances between the antennae of observational stations and the Martian center of mass and could contain systematic errors due to the insufficiently accurate elimination of the spacecraft orbit when producing the normal points. These systematic errors, which exceed the 2-m *a priori* errors, were seen in the original MGS data; these have now been reduced considerably. Unfortunately, in contrast to the two-frequency Viking observations, which made it possible to completely allow for the delay in the solar corona, the Mariner-9 observations as well as the MGS and Odyssey measurements were performed in one band. Therefore, the effect of the solar corona was significant, particularly near superior conjunctions with the Sun. We used the following model of the solar corona to reduce these observations:

$$N_e(r) = \frac{A}{r^6} + \frac{B + \dot{B}t}{r^2},$$

where $N_e(r)$ is the electron density; the parameters B and $\dot{B}$ were determined from observations and were different for different conjunctions. Although the residuals in the observations decrease significantly after this correction for the solar corona, the remaining influence of the corona is still noticeable in them. Moreover, the parameters of the corona correlate with other parameters being determined and adversely affect their determination.

In addition, for some of the series of observations, it was necessary to introduce constant shifts that were interpreted as systematic errors of an unknown origin or calibration errors of the instrumentation. We introduced the following constant shifts for six groups of observations: 6.9 km for the Goldstone observations of Venus in 1964, 2.9 km for the Crimean observations of Venus in 1969, 7.3 km for the Crimean observations of Mercury in 1986–1989, about 20 m for the Viking-1 and -2 observations, and 2.5 m for Odyssey. The possibility of such errors in the Crimean observations of Venus in 1969 and the Viking-1, -2 and Odyssey observations was pointed out by the observers themselves; the existence of systematic errors in the observations of Venus in 1964 in Goldstone and of Mercury in 1986–1989 in Crimea follows from a comparison with other radar measurements in the same period.

All of the above errors reduce significantly the accuracy of the parameters.

It should also be noted that in those cases where additional information about any parameters could not be obtained, the observations performed during a day or within one session for MGS and Odyssey were combined into normal points after applying all the necessary corrections. During the combination, we assigned a weight to all measurements according to their *a priori* accuracy that is generally given in the publications.

DETERMINING THE RELATIVISTIC PARAMETERS AND THE SOLAR OBLATENESS

The Secular Variation of the Gravitational Constant

Finding the possible secular variation of the gravitational constant is of crucial importance, since, basically, the strong equivalence principle is verified. If the cosmology of the Universe affects the local physical processes, then one could expect the coupling coefficients between the various physical fields to vary with cosmological time scale, and no single fundamental natural clocks are possible; i.e., the gravitational and atomic clocks are incommensurable. According to Canuto *et al.* (1979), the secular difference between the atomic time scale in which the observations are performed and the dynamical time scale in which the General Relativity equations of motion are valid can be interpreted in terms of the variation of the gravitational constant G. The directly observed effect in the planetary longitudes depends on the time interval quadratically, and one might expect the error in $\dot{G}/G$ from the *a priori* errors to be $\sim 10^{-12}$ per year or less. This is approximately the level at which the G variability is expected, as implied by certain physical arguments, for example, by Dirac's hypothesis of large numbers.

Table 1. Secular variation of the gravitational constant

$\dot{G}/G$ (10^{-11} per year)	
15 ± 9	Reasenberg and Shapiro (1978)
14 ± 2	Anderson *et al.* (1978)
0.2 ± 0.4	Hellings *et al.* (1983, 1989)
1.10 ± 1.07	Damour and Taylor (1991)
0.00 ± 0.11	Williams *et al.* (2002)
4.1 ± 0.8	Pitjeva (1986)
0.28 ± 0.32	Pitjeva (1993)
-0.002 ± 0.005	Pitjeva (this paper)

The parameter $\dot{G}/G$ was improved simultaneously with all the major parameters of the theory and the additional parameters β, γ, $\dot{G}/G$, and J_2 of the Sun. In addition, we calculated the test versions of the solutions where other unknowns or sets of observations were included in or excluded from the parameters to be determined. Just as Reasenberg *et al.* (1979), we calculated the masking factor: $\mu(\dot{G}/G) = \sigma(\dot{G}/G)/\sigma^*(\dot{G}/G)$, where σ and σ^* are, respectively, the standard deviations of the $\dot{G}/G$ estimates when all parameters are estimated simultaneously (σ) and when only one parameter is estimated (σ^*). The closer the value of μ to unity, the more stable the estimate of the parameter. In the case of a strong correlation between the parameters, μ can reach large values (several hundred). For $\mu(\dot{G}/G)$, we obtained a value of 28, which shows the achieved stability of the derived value ($\mu(\dot{G}/G) = 80$ in the paper by Reasenberg and Shapiro (1978)).

The possible variation of the gravitational constant can in principle be determined by analyzing lunar (including ancient) eclipses, lunar laser-ranging data, radar observations of planets and spacecraft, and pulsar timing data. Table 1 gives the values of $\dot{G}/G$ obtained by different methods. The first two values were independently obtained in 1978 by two groups by analyzing radar observations of planets and spacecraft on a relatively short time interval; the accuracy of the best observations was $\sim$1 μs at that time. A zero $\dot{G}/G$ was obtained when the 6-yr-long series of much more accurate Viking lander observations were included in the data analysis by Hellings *et al.* in 1983 and confirmed in 1989. Williams *et al.* determined $\dot{G}/G$ in 2002 by processing the 1970–2000 lunar laser-ranging data. Damour and Taylor (1991) derived $\dot{G}/G$ by analyzing the rate of change in the orbital period of the binary pulsar PSR 1913+16 and assumed that the variation of the gravitational constant could be determined most accurately only by this method. However, it subsequently emerged that the accuracy of this parameter is limited for pulsar timing and depends on the equation of state for a neutron star and the theory of gravitation in strong fields. Our values obtained in different years by processing radar observations of planets and spacecraft are given at the bottom of Table 1. The nonzero $\dot{G}/G$ in 1986 can probably be attributed to the systematic errors of the earliest radar observations. Substantial progress in the accuracy of estimating this parameter and a decrease in the possible range of the $\dot{G}/G$ variation can be seen from Table 1.

Parameters of the PPN Formalism

The quantities β and γ are the parameters of the PPN formalism that describe the metric theories of gravitation; β represents the degree of nonlinearity of gravitation, and γ characterizes the curvature of space produced by the rest mass. In General Relativity, $\beta = \gamma = 1$. The two classical relativistic tests, the deflection of light by the Sun and the delay of a signal as it passes near the Sun, measure the same effect, the propagation of photons in curved space near the Sun, and depend on the parameter γ. This parameter can be estimated with a high accuracy by measuring the deflection of light during VLBI observations of quasars. In Table 2, these are the values obtained by Robertson *et al.* (1991), Lebach *et al.* (1995), and Eubanks *et al.* (1997). The value of γ estimated by Eubanks *et al.* (1997) was combined with the latest values of Nordtvedt's parameter from lunar laser-ranging observations and the correction to the advance of Mercury's perihelion from radar observations of planets and spacecraft, which allowed them to also estimate β and the solar oblateness. Froeschle *et al.* (1997) estimated γ by analyzing optical Hipparcos observations.

After Shapiro *et al.* discovered the theoretical effect of the delay of radio signals as they pass near the Sun, in 1968, this effect has been measured several times using radar observations of planets and spacecraft: Anderson *et al.* (1975) (Mariner-6,7) and Reasenberg *et al.* (1979) (Viking). The most recent and accurate estimate (Bertotti *et al.* 2003) was obtained by measuring the frequency shift of radio photons to and from the Cassini spacecraft.

The possibilities for estimating β are much fewer. This parameter can be determined from Nordtvedt's effect ($4\beta - \gamma - 3$) when processing laser-ranging observations (Williams *et al.* 2002) or from the analysis of radar observations of the inner planets and spacecraft using the relativistic perturbations that produce periodic and secular variations in the orbital

Table 2. Parameters of the PPN formalism

$\gamma - 1$		$\beta - 1$	
0.00 ± 0.03	Anderson *et al.* (1975)		
0.000 ± 0.002	Reasenberg *et al.* (1979)		
0.0002 ± 0.0010	Robertson *et al.* (1991)		
-0.0004 ± 0.0017	Lebach *et al.* (1995)		
-0.003 ± 0.003	Froeschle *et al.* (1997)		
-0.00006 ± 0.00031	Eubanks *et al.* (1997)	-0.00019 ± 0.00026	Eubanks *et al.* (1997)
0.002 ± 0.004	Williams *et al.* (2002)	-0.001 ± 0.004	Williams *et. al.* (2002)
-0.0015 ± 0.0021	Anderson *et al.* (2002)	-0.0010 ± 0.0012	Anderson *et al.* (2002)
0.000021 ± 0.000023	Bertotti *et al.* (2003)		
-0.13 ± 0.06	Pitjeva (1986)	0.24 ± 0.12	Pitjeva (1986)
0.006 ± 0.037	Pitjeva (1993)	0.014 ± 0.070	Pitjeva (1993)
-0.0001 ± 0.0002	Pitjeva (this paper)	0.0000 ± 0.0001	Pitjeva (this paper)

elements of planets (Anderson *et al.* 2002); in particular, the relativistic secular motion of the perihelia depends on $(2 + 2\gamma - \beta)/3$. In these cases, the two parameters β and γ can be simultaneously estimated by also taking into account Shapiro's effect. It should be noted, however, that the correlation between β and γ is rather strong; it is 95% and 84% in the papers by Williams *et al.* (2002) and Pitjeva (2005), respectively.

Our estimates of β and γ obtained in different years by processing radar observations of the inner planets and spacecraft similar to Anderson *et al.* (2002) are given at the bottom of Table 2. Compared to the paper by Anderson *et al.* (2002), our 2005 results were obtained by including a large number of high-precision radar and VLBI observations of the MGS and Odyssey spacecraft (1998–2003) and some of the other series of observations, for example, the Russian radar observations (1961–1995), in the data analysis. In addition, the dynamic model of planetary motions was improved significantly by including 301 large asteroids and the perturbations from the asteroid ring with their masses estimated from observations in the simultaneous numerical integration; in this way, we reduced significantly the asteroid noise that deteriorates the accuracy of the solution parameters. The higher accuracy achieved in the last paper can probably be explained by these two factors.

The results show that the motions of the inner planets are in excellent agreement with General Relativity and leave increasingly few possibilities for alternative theories of gravitation.

The Secular Motions of Planetary Perihelia

Detecting the advance motions of planetary perihelia and, subsequently, their explanation in terms of General Relativity effects was one of the first relativistic tests. Indeed, the corrections to the motions of planetary perihelia are clearly revealed from observations; the masking factor $\mu(\Delta\delta_i)$ is only within the range 1.1–1.8 when determining these parameters from currently available observations.

The Schwarzschild advance of a planetary perihelion in a century is (Brumberg 1972)

$$\Delta\pi = \frac{3R_\mu n}{a(1-e^2)},$$

where R_μ and a are, respectively, the gravitational radius of the Sun and the semimajor axis of the planet in the same units; e is the eccentricity, n is the mean motion of the planet in arcsecs per 100 yr. The relativistic advances of the perihelia $\Delta\pi$ estimated for the inner planets are given in Table 3. However, the orbital elements of the planets vary with time due to the mutual perturbations of all objects in the Solar system; therefore, the precise advances of the perihelia cannot be given. Standish (2000) determined the mean secular relativistic advance of Mercury's perihelion, which is $42''.980$ on the interval 1800–2200, by comparing Mercury's perihelia every 400 days in two ephemerides obtained by integration and distinguished by the presence or absence (i.e., $\beta = \gamma = 0$) of the relativistic terms of General Relativity in the equations of motion for the planets.

Table 3. Secular motions of the planetary perihelia (arcsecs per century)

Mercury	Venus	Earth	Mars	Source
42.98	8.62	3.84	1.35	Brumberg (1972)
0.11 ± 0.22	-3.03 ± 0.71	-0.12 ± 0.16	-0.35 ± 0.24	Pitjeva (1986)
-0.017 ± 0.052	–	–	–	Pitjeva (1993)
-0.0036 ± 0.0050	0.53 ± 0.30	-0.0002 ± 0.0004	0.0001 ± 0.0005	Pitjeva (this paper)

For alternative theories of gravitation, the principal term in the advance of the perihelion is

$$\frac{1}{3}(2 + 2\gamma - \beta)\Delta\pi.$$

The second term for nonconservative theories of gravitation, which appears with the coefficient $M_\odot M_p/(M_\odot + M_p)$ ($M_\odot$ and M_p are the masses of the Sun and the planet, respectively), is negligible for the inner planets and is not considered below.

The situation is complicated by the fact that the solar oblateness also causes the secular advance of the planetary perihelia. Thus, the total advance of the perihelia (δ) is a linear combination of the post-Newtonian parameters and the gravitational quadrupole moment of the Sun (J_2):

$$\delta = \Delta\pi\left[\frac{1}{3}(2 + 2\gamma - \beta) - \frac{1}{2}\frac{R_\odot^2}{R_\mu a(1-e^2)}J_2(3\sin^2 i - 1)\right],$$

where i is the orbital inclination of the planet.

By comparing the model observations computed using the constructed ephemerides with actual observations, we can obtain the correction $\Delta\delta$ that can be interpreted as a correction to the combination of post-Newtonian parameters $2 + 2\gamma - \beta$ or as a correction to J_2, or as a correction to both. The accuracy and the number of existing observations in the 1960s–1970s were not enough to determine the individual parameters β, γ, and J_2; only the correction $\Delta\delta$ to their linear combination and only for Mercury could be determined. The actual corrections to the motions of the perihelia of other planets could not be determined at that time. At present, as a test, we can determine not β, γ, and J_2, but the corrections to the motions of the planetary perihelia, which allows us to judge whether the values of β, γ, and J_2 used to construct the ephemerides are valid.

Table 3 gives our corrections to the secular motions of the planets obtained in different years. We see from Table 3 that the accuracies of these parameters for all the planets, except Venus, has increased significantly due to the increase of the time interval on which the planets are observed and owing to the high-precision MGS and Odyssey observations. Table 3 shows that the parameters $\beta = 1$, $\gamma = 1$, and $J_2 = 2 \times 10^{-7}$ used to construct the EPM2004 ephemerides are in excellent agreement with the observations. Although the correction to the advance of Mercury's perihelion is within the error limits, a small negative correction to the combination δ may be required. Assuming that $\beta = 1$ and $\gamma = 1$, we obtain a new estimate of the solar oblateness, $J_2 = (1.7 \pm 0.5) \times 10^{-7}$. The solar oblateness is discussed in more detail below.

The Gravitational Quadrupole Moment of the Sun

Determining the dynamical oblateness of the Sun is of great importance, since the solar oblateness serves as a check for the theories that describe the interior structure of the Sun and its rotation and is one of the parameters required to construct high-precision theories of planetary and lunar motions. As yet, there is no universally accepted and satisfactorily determined value of the dynamical oblateness of the Sun. This parameter can be determined indirectly from various astrophysical observations of the Sun. However, such observations involve many problems: the rotation of the Sun around its axis is fairly complex, the outer layers have different angular velocities at different latitudes, the information about the rotation of inner layers is insufficient; the brightness of the solar limb depends on the latitude as well as on the solar cycle, the number of faculae, and the number of sunspots; the calibration of ground-based data for the atmosphere causes great difficulties. The initial estimates of the solar oblateness (before approximately 1970) using heliometers and photographic plates were often erroneous, but using new techniques, improving the theory of the solar interior structure, and performing satellite observations allow the gravitational quadrupole moment of the Sun (J_2) to be determined with a higher accuracy. Some of the J_2 values obtained from astrophysical observations are given in the upper part of Table 4. The value by Hill *et al.* (1982) was one of the most accurate for

his time, and it was commonly used in celestial mechanics for various estimates. The table also gives the recent and (probably) most accurate estimates obtained from astrophysical observations (Paterno *et al.* 1996; Pijpers 1998; Godier and Rozelot 2000). A good overview of all the available estimates of the solar quadrupole moment was given by Pireaux and Rozelot (2003).

The dynamic oblateness of the Sun can be determined independently during the construction of a theory for the motion of bodies in the Solar system when determining the parameters of this theory from observations. The solar oblateness produces secular trends in all the elements of the planets, except their semiaxes and eccentricities. The secular trends are inversely proportional to the square of the semiaxes; the largest secular trend due to the solar oblateness arises in Mercury's perihelion. According to Brumberg (1972), the rate of secular motion of the perihelion is given by

$$d\pi_S = \frac{3}{2}\left(\frac{R_\odot}{a}\right)^2 \frac{n}{(1-e^2)^2} J_2.$$

In constructing the JPL versions of the DE405 ephemerides and our EPM2000 based on the estimates by Duvall *et al.* (1984) and Brown *et al.* (1989) obtained from helioseismometric measurements (under certain additional assumptions) (see Table 4), a nonzero solar oblateness, $J_2 = 2 \times 10^{-7}$, has been used for the first time in the integration.

In this case, the main problem lies in the smallness of the parameter J_2 and in its separation from the post-Newtonian parameters β and γ. This could not be done before a large number of high-precision MGS and Odyssey data appeared in recent years, and the dynamic estimate of the solar oblateness was obtained from the estimates of the motion of Mercury's perihelion that included a linear combination of post-Newtonian parameters and the solar oblateness. Some of these estimates are given in the middle part of Table. 4. The estimate by Eubanks *et al.* (1997) was obtained by combining the resent estimates of γ, Nordtvedt's parameter, and the advance of Mercury's perihelion.

In 1990, the dynamic oblateness of the Sun was determined by the methods of celestial mechanics from the analysis of radar and optical (1960–1986) observations by Afanasieva *et al.* 1990. Unfortunately, most of the modern high-precision American radar observations of planets, spacecraft, and landers was inaccessible at that time, and the accuracy of the estimate obtained was not high enough. It has become possible to simultaneously estimate all three parameters J_2, β, and γ only in recent years. These determinations are given in the lower part of Table 4.

Table 4. The gravitational quadrupole moment of the Sun

$J_2 \times 10^{-7}$	
55 ± 13	Hill *et al.* (1982)
1.7 ± 0.4	Duvall *et al.* (1984)
1.7 ± 0.2	Brown *et al.* (1989)
2.08 ± 0.14	Paterno *et al.* (1996)
2.18 ± 0.06	Pijpers (1998)
2.0 ± 1.4	Godier and Rozelot (2000)
13.9 ± 24.7	Shapiro *et al.* (1972)
26.3 ± 16.5	Anderson *et al.* (1978)
12.3 ± 11.5	Anderson *et al.* (1992)
-1.8 ± 4.5	Eubanks *et al.* (1997)
-11.7 ± 9.5	Pitjeva (1986)
-1.3 ± 4.1	Pitjeva (1993)
2.4 ± 0.7	Pitjeva (2001)
6.6 ± 9.0	Afanasieva *et al.* (1990)
-5 ± 10	Williams *et al.* (2002)
2.3 ± 5.2	Anderson *et al.* (2002)
1.9 ± 0.3	Pitjeva (this paper)

The value by Williams *et al.* (2002) was obtained from the analysis of lunar laser-ranging observations. The estimates by Anderson *et al.* (1992) and our estimates were obtained by analyzing radar observations of the inner planets and spacecraft (the masking factor of the solar oblateness $\mu(J_2)$ is 17). The last, more accurate estimate agrees well with the estimate deduced from the advance of Mercury's perihelion in the previous section.

A test version of the EPM ephemerides similar to EPM2004, but with $J_2 = 6.52 \times 10^{-7}$ deduced from S. Lefevre's figure theory, was constructed at the request of the colleagues involved in preparing the European BepiColombo mission to Mercury. Subsequently, these ephemerides were improved using observations with an improvement of all the parameters, except J_2. As might be expected, the representation of the observations of Venus and Mars did not change, because this parameter is small. Although the usual accuracy of Mercury's observations is only about 1 km, a deterioration of Mercury's representation in the test version is still noticeable: the rms error of the residual of Mercury's observations was 1228 m compared to 1192 m for the main ephemerides, where $J_2 = 2 \times 10^{-7}$ was used for the integration. Improving the parameter J_2 for the test version of the the-

ory yielded $J_2 = 1.6 \times 10^{-7}$, which again agrees with the values obtained when improving the EPM2004 ephemerides.

Thus, we conclude that the gravitational quadrupole moment of the Sun is probably close to or slightly smaller than 2.0×10^{-7}.

CONVERSION FROM THE EPHEMERIDES IN THE TDB TIME SCALE TO THE EPHEMERIDES IN THE TCB SCALE

According to IAU resolutions, the ICRS should be considered as a four-dimensional coordinate system with an independent variable—the TCB coordinate time in the scale of which the planetary ephemerides should be given. For comparison with the widely used JPL DE ephemerides, our EPM ephemerides have been constructed until the present time with the TDB time scale (as an independent variable) close to $T_{\rm eph}$ (Standish 1998), which is used to construct the DE ephemerides. Since, according to IAU recommendations, the planetary ephemerides constructed in the TCB scale are required for the users that process VLBI measurements and observations of Earth satellites, we constructed an additional version of the EPM ephemerides in the TCB scale. The following transformations should be made to make a transition from the TDB scale to the TCB scale (see, e.g., Brumberg and Groten 2001):

(1) The initial epoch of integration JD = 2 448 800.5 TDB is expressed in terms of TCB:

$$\text{date(TCB)} = (\text{date(TDB)} - 2\,443\,144.5) \times L_B + \text{date(TDB)},$$

(2) The coordinates are multiplied by $(1 + L_B)$:

$$x_i(\text{TCB}) = x_i(\text{TDB}) \times (1 + L_B),$$

(3) The masses are multiplied by $(1 + L_B)$:

$$GM_i(\text{TCB}) = GM_i(\text{TDB}) \times (1 + L_B),$$

(4) The round-trip light time of the radar observations calculated in the TCB scale should be expressed in terms of the proper time, i.e., first

$$\tau_{\text{TDB}} = \tau_{\text{TCB}} \times (1 - L_B),$$

and then transformed to the proper time scale in a standard way.

Since the EPM ephemerides are close to DE405, we used

$$L_B = 1.55051976772 \times 10^{-8},$$

obtained for the relationship between TCB and TDB of the DE405 ephemerides.

The conversion to the TCB coordinate time scale should not and did not cause the accuracy of the ephemerides and the parameters being improved to increase. The residuals in the observations are identical for these two versions of the EPM ephemerides. As might be expected, the formal standard accuracies of all parameters and their values (except the orbital elements of the planets) are equal within the formal uncertainties.

CONCLUSIONS

The passage of photons and the motion of planets in the gravitational field of the Sun allow the Solar system to be considered as a convenient laboratory for testing various theories of gravitation. The currently available radar observations of planets and spacecraft with a meter accuracy (a relative error of 10^{-11}–10^{-12}) make it possible to test the relativistic effects and to estimate the solar oblateness. The uncertainties in these parameters (see Tables 1–4) has decreased significantly since 1993: by more than an order of magnitude for the gravitational quadrupole moment of the Sun and the advance of Mercury's perihelion and even by one and a half orders of magnitude or more for the remaining parameters (β, γ, $\dot{G}/G$, the advance of the perihelia of the Earth and Mars).

Substantial progress can be explained by several factors: an increase in the accuracy of observational data reduction procedures and dynamical models of motion as well as an improvement in the quality of observational data and an increase in their accuracy and in the length of the time interval on which these observations were obtained. As the uncertainties in these parameters decrease, the domain of possible values of the relativistic parameters narrows, imposing increasingly stringent constraints on the theories of gravitation alternative to General Relativity.

In conclusion, note that the numerical EPM2004 ephemerides of all planets and the Moon are available via FTP: flp://quasar.ipa.nw.ru/incoming/ EPM2004 or via the web site of the Institute of Applied Astronomy, Russian Academy of Sciences.

REFERENCES

1. E. I. Afanasieva, M. D. Kislik, Yu. F. Kolyuka, and V. F. Tikhonov, Astron. Zh. **67**, 1326 (1990) [Sov. Astron. **34**, 670 (1990)].
2. J. D. Anderson, J. K. Campbell, R. F. Jurgens, *et al.*, *6th Marcel Grossman Meeting on General Relativity*, Ed. by H. Sato and T. Nakamura (World Sci., 1992), p. 353.
3. J. D. Anderson, P. B. Esposito, W. Martin, *et al.*, Astrophys. J. **200**, 221 (1975).
4. J. D. Anderson, M. S. Keesey, E. L. Lau, *et al.*, Acta Astronautica **5**, 43 (1978).
5. J. D. Anderson, E. L. Lau, S. Turyshev, *et al.*, Bull. Am. Astron. Soc. **34**, 660 (2002).

6. B. Bertotti, L. Iess, and P. Tortora, Nature **425**, 374 (2003).
7. T. M. Brown, J. Christensen-Dalsgaad, W. A. Dziembowski, *et al.*, Astrophys. J. **343**, 526 (1989).
8. V. A. Brumberg, *Relativistic Celestial Mechanics* (Nauka, Moscow, 1972).
9. V. A. Brumberg and E. Groten, Astron. Astrophys. **367**, 1070 (2001).
10. V. M. Canuto, S.-H. Hsieh, and J. R. Owen, Mon. Not. R. Astron. Soc. **188**, 829 (1979).
11. T. Damour and J. H. Taylor, Astrophys. J. **366**, 501 (1991).
12. T. L. Duvall, W. A. Dziembowski, P. Goode, *et al.*, Nature **310**, 22 (1984).
13. T. M. Eubanks, D. N. Matsakis, J. O. Martin, *et al.*, *American Physical Society APS/AAPT Joint Meeting* (1997).
14. M. Froeschle, F. Mignard, and F. Arenou, *Hipparcos—Venice 97, ESA-402* (Venice, 1997), p. 49.
15. S. Godier and J. P. Rozelot, Astron. Astrophys. **355**, 365 (2000).
16. R. W. Hellings, P. J. Adams, J. D. Anderson, *et al.*, Phys. Rev. Lett. **51**, 1609 (1983).
17. R. W. Hellings, P. J. Adams, J. D. Anderson, *et al.*, Int. J. Theor. Phys. **28**, 1035 (1989).
18. H. A. Hill, R. J. Bos, and P. R. Goode, Phys. Rev. Lett. **49**, 1794 (1982).
19. G. A. Krasinsky, Commun. of IAA RAS **148**, 1 (2002).
20. G. A. Krasinsky, E. V. Pitjeva, M. V. Vasilyev, and E. I. Yagudina, Commun. of IAA RAS **139**, 1 (2001).
21. G. A. Krasinsky, E. V. Pitjeva, M. V. Vasilyev, and E. I. Yagudina, Icarus **158**, 98 (2002).
22. D. E. Lebach, B. E. Corey, I. I. Shapiro, *et al.*, Phys. Rev. Lett. **75**, 1439 (1995).
23. X. X. Newhall, E. M. Standish, Jr., and J. G. Williams, Astron. Astrophys. **125**, 150 (1983).
24. L. Paterno, S. Sofia, and M. P. Di Mauro, Astron. Astrophys. **314**, 940 (1996).
25. F. P. Pijpers, Mon. Not. R. Astron. Soc. **297**, L76 (1998).
26. S. Pireaux and J.-P. Rozelot, Astrophys. Space Sci. **284**, 1159 (2003).
27. E. V. Pitjeva, Byull. Inst. T. A., Ross. Akad. Nauk **15**, 538 (1986).
28. E. V. Pitjeva, Celest. Mech. **55**, 333 (1993).
29. E. V. Pitjeva, *Third International Workshop on Position Astronomy and Celestial Mechanics*, Ed. by G. A. Lopez, E. I. Yagudina, U. M. Martinez, and B. A. Condero (Observ. Astron. Univ. Valencia, 1996), p. 583.
30. E. V. Pitjeva, Tr. Inst. P. A., Ross. Akad. Nauk **4**, 22 (1999).
31. E. V. Pitjeva, Tr. Inst. P. A., Ross. Akad. Nauk **5**, 58 (2000).
32. E. V. Pitjeva, Celest. Mech. **80**, 249 (2001).
33. E. V. Pitjeva, Tr. Inst. P. A., Ross. Akad. Nauk **10**, 112 (2004).
34. E. V. Pitjeva, *Transit of Venus: New Views of the Solar System and Galaxy, IAU Coll. 196*, Ed. by D. W. Kurtz (Cambridge University Press, 2005).
35. R. D. Reasenberg and I. I. Shapiro, *On the Measurement of Cosmological Variations of the Gravitational Constant*, Ed. by L. Halpern (Florida Univ. Press, USA, 1978), p. 71.
36. R. D. Reasenberg, I. I. Shapiro, P. E. MacNeil, *et al.*, Astrophys. J. **234**, L219 (1979).
37. D. S. Robertson, W. E. Carter, and W. H. Dillinger, Nature **349**, 768 (1991).
38. I. I. Shapiro, G. H. Pettengill, M. E. Ash, *et al.*, Phys. Rev. Lett. **28**, 1594 (1972).
39. I. I. Shapiro, G. H. Pettengill, M. E. Ash, *et al.*, Phys. Rev. Lett. **20**, 1265 (1968).
40. E. M. Standish, Bull. Am. Astron. Soc. **32**, 870 (2000).
41. E. M. Standish, Astron. Astrophys. **233**, 252 (1990).
42. E. M. Standish, Astron. Astrophys. **336**, 381 (1998).
43. E. M. Standish and A. Fienga, Astron. Astrophys. **384**, 322 (2002).
44. J. G. Williams, D. H. Boggs, J. O. Dickey, and W. M. Folkner, *Ninth Marcel Grossman Meeting*, Ed. by V. G. Gurzadyan, R. T. Jantzen, and R. Ruffini (World Sci., 2002), p. 1797.

Translated by V. Astakhov

Astronomy Letters, Vol. 31, No. 5, 2005, pp. 350–356. Translated from Pis'ma v Astronomicheskiĭ Zhurnal, Vol. 31, No. 5, 2005, pp. 388–394.

On One Special Case of Parametric Resonance in Problems of Celestial Mechanics

A. P. Markeev*

Institute for Problems of Mechanics, Russian Academy of Sciences, Moscow, Russia

Received November 19, 2004

Abstract—We consider a periodic (in time) linear Hamiltonian system that depends on a small parameter. At a zero value of this parameter, the matrix of the system is constant, has two identical pairs of purely imaginary roots, and is not reducible to diagonal form. Therefore, the unperturbed system is unstable. We propose an algorithm for determining the boundaries of the instability regions for the system at nonzero values of the small parameter. This algorithm was used to analyze the stability of triangular libration points in the elliptical restricted three-body problem and in the stability problem in one special case of stationary rotation of a satellite relative to the center of mass. © *2005 Pleiades Publishing, Inc.*

Key words: *celestial mechanics, resonance, stability, three-body problem, satellites.*

INTRODUCTION

Many problems of classical and celestial mechanics necessitate analyzing a 2π-periodic (in time t) linear Hamiltonian system with two degrees of freedom that depends on a small parameter, ε. We assume that the corresponding Hamiltonian can be represented as a power series of ε, with it being independent of t at $\varepsilon = 0$. We also assume that the Hamiltonian depends on another parameter, μ, and that the characteristic equation for the unperturbed (at $\varepsilon = 0$) linear system of differential equations at a certain value of this parameter, $\mu = \mu_*$, has two pairs of purely imaginary roots, $\pm i\omega_1$ and $\pm i\omega_2$. The problem of the stability of a perturbed ($0 < \varepsilon \ll 1$) system for μ close to μ_* was analyzed in detail by Yakubovich and Starzhinskii (1987).

We consider the special, as yet unanalyzed case where $\omega_1 = \omega_2 = \omega$ and the corresponding unperturbed Hamiltonian cannot be reduced to the sum of two uncoupled harmonic oscillators with frequencies ω through canonical changes of variables. The unperturbed system is then unstable.

One of our goals is to develop an algorithm for determining the boundary of the instability region that emerges from the point $\mu = \mu_*$ of the $\varepsilon = 0$ axis in the ε, μ plane for small ε. Another goal is to apply our algorithm to two as yet incompletely solved problems of celestial mechanics: the stability of triangular libration points in the plane elliptical restricted three-body problem and the stability of the stationary rotation of a dynamically symmetric satellite around the normal to the orbital plane of its center of mass.

*E-mail: markeev@ipmnet.ru

ON THE METHOD OF ANALYSIS

We specify the equation for the boundary of the instability region adjacent to the point $\mu = \mu_*$ at $\varepsilon = 0$ in the form of a series,

$$\mu = \mu_* + \sum_{m=1}^{\infty} \varepsilon^m \mu_m, \tag{1}$$

where the constants μ_1, μ_2, ... are to be determined.

We substitute expansion (1) in the initial Hamiltonian $H = H(q_1, q_2, p_1, p_2, t; \mu, \varepsilon)$ and expand the derived function in a power series of ε. Subsequently, using a well-known algorithm (Markeev *et al.* 1985), we make a linear canonical change of variables, $q_1, q_2, p_1, p_2 \to x_1, x_2, X_1, X_2$, which reduces the unperturbed (at $\varepsilon = 0$) Hamiltonian to normal form. As a result, we obtain

$$H = H_0(x_1, x_2, X_1, X_2) \tag{2}$$
$$+ \sum_{m=1}^{\infty} \frac{\varepsilon^m}{m!} H_m(x_1, x_2, X_1, X_2, t, \mu_1, \mu_2, ..., \mu_m),$$

where

$$H_0 = \frac{1}{2}(x_1^2 + x_2^2) + \omega(x_1 X_2 - x_2 X_1), \tag{3}$$

and H_m ($m \geq 1$) are quadratic forms with respect to x_1, x_2, X_1, X_2 with 2π-periodic (in t) coefficients that also depend on the sought coefficients μ_1, μ_2, ... of expansion (1).

After reducing the Hamiltonian to form (2), we make a canonical 2π-periodic (in t) linear transformation, $x_1, x_2, X_1, X_2 \to y_1, y_2, Y_1, Y_2$, which eliminates the time from the new Hamiltonian

1063-7737/05/3105-0350$26.00

$K(y_1, y_2, Y_1, Y_2, t, \varepsilon, \mu_1, \mu_2, ...)$ up to the terms of order ε^n inclusive (n can be large). Discarding the terms of degrees higher than n in the expansion of the function K in terms of ε leads to an approximate transformed autonomous Hamiltonian system with two degrees of freedom. Determining the coefficients $\mu_1, \mu_2, ...$ of expansion (1) then becomes a simple problem, since it reduces to analyzing a biquadratic characteristic equation for this approximate system.

We can make the change of variables x_1, x_2, $X_1, X_2 \to y_1, y_2, Y_1, Y_2$ and construct the transformed Hamiltonian K by various methods of the perturbation theory (Giacaglia 1972). Below, we use the Deprit–Hori method in the Kamel modification (Markeev 1978).

THE CASE WHERE THE NUMBER 2ω IS NOT AN INTEGER

We write the new Hamiltonian K and the generating function W in the Deprit–Hori method as series,

$$K = \sum_{m=0}^{\infty} \frac{\varepsilon^m}{m!} K_m(y_1, y_2, Y_1, Y_2, t, \mu_1, ..., \mu_m),$$

$$W = \sum_{m=0}^{\infty} \frac{\varepsilon^m}{m!} W_{m+1}(y_1, y_2, Y_1, Y_2, t, \mu_1, ..., \mu_m),$$

where

$$K_0 = H_0(y_1, y_2, Y_1, Y_2).$$

Finding the terms of the first degree with respect to ε leads to analyzing the following linear partial differential equation:

$$K_1 = H_1(y_1, y_2, Y_1, Y_2, t, \mu_1) + (H_0, W_1) - \frac{\partial W_1}{\partial t}, \quad (4)$$

where (H_0, W_1) is the Poisson bracket,

$$(H_0, W_1) = \sum_{i=1}^{2} \left(\frac{\partial H_0}{\partial y_i}\frac{\partial W_1}{\partial Y_i} - \frac{\partial H_0}{\partial Y_i}\frac{\partial W_1}{\partial y_i}\right).$$

We write the quadratic form H_1 in Eq. (4) as

$$H_1 = \sum h^{(1)}_{m_1 m_2 n_1 n_2} y_1^{m_1} y_2^{m_2} Y_1^{n_1} Y_2^{n_2},$$

where the summation is over the integer nonnegative numbers m_1, m_2, n_1, n_2, the sum of which is equal to two. We also represent the quadratic forms K_1 and W_1 as similar sums.

The coefficients $w^{(1)}_{m_1 m_2 n_1 n_2}$ of the form W_1 should be chosen in such a way that they be 2π-periodic in t and the coefficients $k^{(1)}_{m_1 m_2 n_1 n_2}$ of the form K_1 be constant or (if this can be done) even zero.

Equating the coefficients of the same degrees of y_1, y_2, Y_1, Y_2 on the left- and right-hand sides of equality (4) yields ten relations that we break up into the following three groups:

$$\frac{dw^{(1)}_{0020}}{dt} = -\omega w^{(1)}_{0011} + h^{(1)}_{0020} - k^{(1)}_{0020}, \quad (5)$$

$$\frac{dw^{(1)}_{0011}}{dt} = 2\omega(w^{(1)}_{0020} - w^{(1)}_{0002}) + h^{(1)}_{0011} - k^{(1)}_{0011},$$

$$\frac{dw^{(1)}_{0002}}{dt} = \omega w^{(1)}_{0011} + h^{(1)}_{0002} - k^{(1)}_{0002},$$

$$\frac{dw^{(1)}_{1001}}{dt} = \omega(w^{(1)}_{1010} - w^{(1)}_{0101}) + w^{(1)}_{0011} + h^{(1)}_{1001} - k^{(1)}_{1001}, \quad (6)$$

$$\frac{dw^{(1)}_{0101}}{dt} = \omega(w^{(1)}_{1001} + w^{(1)}_{0110}) + 2w^{(1)}_{0002} + h^{(1)}_{0101} - k^{(1)}_{0101},$$

$$\frac{dw^{(1)}_{1010}}{dt} = -\omega(w^{(1)}_{1001} + w^{(1)}_{0110}) + 2w^{(1)}_{0020} + h^{(1)}_{1010} - k^{(1)}_{1010},$$

$$\frac{dw^{(1)}_{0110}}{dt} = \omega(w^{(1)}_{1010} - w^{(1)}_{0101}) + w^{(1)}_{0011} + h^{(1)}_{0110} - k^{(1)}_{0110},$$

$$\frac{dw^{(1)}_{2000}}{dt} = -\omega w^{(1)}_{1100} + w^{(1)}_{1010} + h^{(1)}_{2000} - k^{(1)}_{2000}, \quad (7)$$

$$\frac{dw^{(1)}_{1100}}{dt} = 2\omega(w^{(1)}_{2000} - w^{(1)}_{0200}) + w^{(1)}_{0110} + w^{(1)}_{1001} + h^{(1)}_{1100} - k^{(1)}_{1100},$$

$$\frac{dw^{(1)}_{0200}}{dt} = \omega w^{(1)}_{1100} + w^{(1)}_{0101} + h^{(1)}_{0200} - k^{(1)}_{0200}.$$

By successively considering relations (5), (6), and (7), we can derive the functions $w^{(1)}_{m_1 m_2 n_1 n_2}(t)$ and the coefficients $k^{(1)}_{m_1 m_2 n_1 n_2}$ that satisfy the requirements formulated above. Without giving our calculations in detail, let us immediately write out the result obtained.

We assume that the number 2ω is not integer; i.e., the resonance under consideration $\omega_1 = \omega_2 = \omega$ is not multiple. We use the following notation:

$$f_1(x) = \int_0^x e^{i2\omega t}[h^{(1)}_{0011} + i(h^{(1)}_{0020} - h^{(1)}_{0002})]dt,$$

$$g_1 = \int (h^{(1)}_{1001} - h^{(1)}_{0110} + k^{(1)}_{0110})dt,$$

$$f_2(x) = \int_0^x e^{i2\omega t}[h^{(1)}_{0101} - \omega g_1 + 2w^{(1)}_{0002}$$

$$+ i(h^{(1)}_{1001} + \omega g_2 + w^{(1)}_{0011})]dt,$$

$$g_2 = \int [(h^{(1)}_{0101} + h^{(1)}_{1010}$$

$$+ 2(w^{(1)}_{0020} + w^{(1)}_{0002}) - k^{(1)}_{1010}]dt,$$

$$f_3(x) = \int_0^x e^{i2\omega t}[(h^{(1)}_{1100} + w^{(1)}_{0110} + w^{(1)}_{1001})$$

$$+ i(h^{(1)}_{2000} - h^{(1)}_{0200} + w^{(1)}_{1010} - w^{(1)}_{0101})]dt,$$

$$g_3 = \int (h^{(1)}_{2000} + h^{(1)}_{0200} + w^{(1)}_{1010} + w^{(1)}_{0101} - 2k^{(1)}_{2000})dt,$$

$$F_j = e^{-i2\omega t}\{f_j(t) - [1 + i\cot(2\pi\omega)]f_j(2\pi)/2\}$$

$$(j = 1, 2, 3).$$

The functions $w^{(1)}_{m_1m_2n_1n_2}(t)$ and the coefficients $k^{(1)}_{m_1m_2n_1n_2}$ can be calculated using the formulas

$$k^{(1)}_{1100} = k^{(1)}_{1001} = k^{(1)}_{0101} = k^{(1)}_{0011} = 0, \qquad (8)$$

$$k^{(1)}_{0110} = \frac{1}{2\pi}\int_0^{2\pi} (h^{(1)}_{0110} - h^{(1)}_{1001})dt,$$

$$w^{(1)}_{0011} = \mathrm{Re}F_1,$$

$$k^{(1)}_{0020} = k^{(1)}_{0002} = \frac{1}{2\pi}\int_0^{2\pi} (h^{(1)}_{0020} - \omega w^{(1)}_{0011})dt,$$

$$w^{(1)}_{0020} = \int (h^{(1)}_{0020} - \omega w^{(1)}_{0011} - k^{(1)}_{0020})dt,$$

$$w^{(1)}_{0002} = w^{(1)}_{0020} - \mathrm{Im}F_1,$$

$$k^{(1)}_{1010} = \frac{1}{2\pi}\int_0^{2\pi} [h^{(1)}_{0101} + h^{(1)}_{1010} + 2(w^{(1)}_{0020} + w^{(1)}_{0002})]dt,$$

$$w^{(1)}_{0101} = \mathrm{Re}F_2, \quad w^{(1)}_{1001} = \mathrm{Im}F_2,$$

$$w^{(1)}_{0110} = w^{(1)}_{1001} - g_1, \quad w^{(1)}_{1010} = g_2 - w^{(1)}_{0101},$$

$$k^{(1)}_{2000} = k^{(1)}_{0200}$$

$$= \frac{1}{4\pi}\int_0^{2\pi} (h^{(1)}_{2000} + h^{(1)}_{0200} + w^{(1)}_{1010} + w^{(1)}_{0101})dt,$$

$$w^{(1)}_{1100} = \mathrm{Re}F_3, \quad w^{(1)}_{2000} = (g_3 + \mathrm{Im}F_3)/2,$$

$$w^{(1)}_{0200} = (g_3 - \mathrm{Im}F_3)/2.$$

By analogy, the second and higher approximations can be constructed by the Deprit–Hori method. In the limit, we find that the transformed Hamiltonian K has the structure

$$K = \frac{1}{2}(1 + 2k_{2000})(y_1^2 + y_2^2) + k_{0020}(Y_1^2 + Y_2^2) \quad (9)$$

$$+ \omega(y_1Y_2 - y_2Y_1) + k_{1010}y_1Y_1 + k_{0110}y_2Y_1,$$

where

$$k_{m_1m_2n_1n_2} = \sum_{m=1}^{\infty} \frac{\varepsilon^m}{m!} k^{(m)}_{m_1m_2n_1n_2}(\mu_1, \mu_2, ..., \mu_m). \qquad (10)$$

The roots of the characteristic equation

$$\lambda^4 + a\lambda^2 + b = 0 \qquad (11)$$

for the autonomous system with Hamiltonian (9) are the characteristic measures of the initial 2π-periodic (in t) system with the Hamiltonian $H(q_1, q_2, p_1, p_2, t; \mu, \varepsilon)$.

A sufficient stability condition is the satisfaction of the system of inequalities

$$a > 0, \quad b > 0, \quad d = a^2 - 4b > 0. \qquad (12)$$

If these inequalities are satisfied simultaneously, then the characteristic measures are purely imaginary and different. If, however, at least one of inequalities (12) is satisfied with the opposite sign, then characteristic measures with a nonzero real part exist and instability takes place.

We can find from the equations of motion with Hamiltonian (9) that the following estimates are valid for the coefficients a and b of Eq. (11):

$$a = 2\omega^2 + O(\varepsilon), \quad b = \omega^4 + O(\varepsilon).$$

At fairly small ε, the values of a and b are positive, and, hence, the sufficient stability condition is reduced to the third of inequalities (12). The boundary of the instability region is specified by the condition $d = 0$. This condition can be written via the coefficients of Hamiltonian (9) as the equality

$$k_{0020} = \frac{k^2_{1010}(4\omega^2 - 4\omega k_{0110} - k^2_{1010})}{8(1 + 2k_{2000})(2\omega - k_{0110})^2}.$$

Equating the terms of the same degrees of ε on the left- and right-hand sides of this equality, we obtain a system of equations for the sought coefficients $\mu_1, \mu_2, \mu_3, ...$ of expansion (1) that specifies the equation for the boundary of the stability region at small ε:

$$k^{(1)}_{0020} = 0, \quad k^{(2)}_{0020} = \frac{1}{4}(k^{(1)}_{1010})^2, \qquad (13)$$

$$k^{(3)}_{0020} = \frac{3}{4}k^{(1)}_{1010}(k^{(2)}_{1010} - 2k^{(1)}_{1010}k^{(1)}_{2000}), ...$$

By successively considering these equations, we can find the coefficients $\mu_1, \mu_2, \mu_3, ...$

It should be noted that the procedures for obtaining coefficients (10) of the transformed Hamiltonian and solving the system of equations (13) can be rather cumbersome. In general, these should be performed using computer systems of analytical calculations.

THE CASE OF A MULTIPLE RESONANCE (2ω IS AN INTEGER)

Let $2\omega = N$, where N is an integer. Then, $\sin(2\pi\omega) = 0$, and we seek a solution of system (5)–(7) in a form different from (8). However, we take a different approach to simplify the calculations.

First, before applying the Deprit–Hori method, we make the following canonical univalent change of variables $x_1, x_2, X_1, X_2 \to x_1', x_2', X_1', X_2'$ in the system with Hamiltonian (2) that simplifies significantly the unperturbed part of Hamiltonian (3) (eliminating the term $\omega(x_1X_2 - x_2X_1)$) from it):

$$x_1 = x_1' \cos\frac{Nt}{2} - x_2' \sin\frac{Nt}{2},$$
$$x_2 = x_1' \sin\frac{Nt}{2} + x_2' \cos\frac{Nt}{2},$$
$$X_1 = X_1' \cos\frac{Nt}{2} - X_2' \sin\frac{Nt}{2},$$
$$X_2 = X_1' \sin\frac{Nt}{2} + X_2' \cos\frac{Nt}{2}.$$

In the new variables, the Hamiltonian remains 2π-periodic in t, while its unperturbed part is (to save space, we omit the primes on the new variables)

$$H_0 = \frac{1}{2}(x_1^2 + x_2^2).$$

The system of relations for the coefficients of the quadratic forms W_1 and K_1 can be derived from relations (5)–(7) if we set $\omega = 0$ in the latter. By considering the derived ten relations successively, we can easily find (using most commonly a computer) the 2π-periodic (in t) functions $w^{(1)}_{m_1m_2n_1n_2}(t)$ and the constant coefficients $k^{(1)}_{m_1m_2n_1n_2}$:

$$k^{(1)}_{0020} = \frac{1}{2\pi}\int_0^{2\pi} h^{(1)}_{0020}dt,$$
$$w^{(1)}_{0020} = \int (h^{(1)}_{0020} - k^{(1)}_{0020})dt,$$
$$k^{(1)}_{0011} = \frac{1}{2\pi}\int_0^{2\pi} h^{(1)}_{0011}dt,$$
$$w^{(1)}_{0011} = \int (h^{(1)}_{0011} - k^{(1)}_{0011})dt,$$
$$k^{(1)}_{0002} = \frac{1}{2\pi}\int_0^{2\pi} h^{(1)}_{0002}dt,$$
$$w^{(1)}_{0002} = \int (h^{(1)}_{0002} - k^{(1)}_{0002})dt,$$
$$k^{(1)}_{1001} = \frac{1}{2\pi}\int_0^{2\pi} (h^{(1)}_{1001} + w^{(1)}_{0011})dt,$$
$$w^{(1)}_{1001} = \int (h^{(1)}_{1001} + w^{(1)}_{1001} - k^{(1)}_{1001})dt,$$

and so on.

In general, the transformed Hamiltonian K contains all tens monomials (rather than eight, as Hamiltonian (9) at nonmultiple resonance):

$$K = \frac{1}{2}(y_1^2 + y_2^2) + \sum k_{m_1m_2n_1n_2} y_1^{m_1} y_2^{m_2} Y_1^{n_1} Y_2^{n_2},$$

where the constant coefficients $k_{m_1m_2n_1n_2}$ can be calculated using formulas similar to (10), and the summation is over the integer nonnegative numbers m_1, m_2, n_1, n_2, the sum of which is equal to 2, etc.

The following estimates are valid for the coefficients a and b of the characteristic equation (11) for the transformed system:

$$a = 2(k^{(1)}_{0020} + k^{(1)}_{0002})\varepsilon + O(\varepsilon^2),$$
$$b = (4k^{(1)}_{0020}k^{(1)}_{0002} - {k^{(1)}_{0011}}^2)\varepsilon^2 + O(\varepsilon^3).$$

It follows from these estimates and from conditions (12) that the inequality $k^{(1)}_{0020} + k^{(1)}_{0002} > 0$ is satisfied at fairly small ε in the stability region, and $\mu_1, \mu_2, \ldots$ in Eq. (1) for the boundary of the instability region can be found from the condition $b = 0$.

ON THE STABILITY OF TRIANGULAR LIBRATION POINTS IN THE ELLIPTICAL RESTRICTED THREE-BODY PROBLEM

The stability of triangular libration points in the plane elliptical restricted three-body problem has been studied extensively. A brief history and main bibliography are given in the monograph by Markeev (1978).

We take the true anomaly ν in the elliptical motion of the main attractive bodies as an independent variable. For the proper choice of canonically conjugate variables, the Hamiltonian that corresponds to the linearized equations of perturbed motion can then be written as

$$H = \frac{1}{2}(p_1^2 + p_2^2) + p_1q_2 - q_1p_2 \qquad (14)$$
$$+ \frac{1}{8(1 + e\cos\nu)}[(1 + 4e\cos\nu)q_1^2$$
$$- 6\sqrt{3}(1 - 2\mu)q_1q_2 - (5 - 4e\cos\nu)q_2^2],$$

where e is the orbital eccentricity of the main bodies, and μ is the ratio of the mass of the smaller body to the sum of their masses.

The inequality

$$0 < \mu < \mu_*, \quad \mu_* = \frac{1}{2} - \frac{\sqrt{69}}{18} = 0.03852$$

is a necessary stability condition for the libration points in the circular restricted three-body problem ($e = 0$). At $e = 0$ and $\mu = \mu_*$, the characteristic equation of the linearized system has two identical pairs of purely imaginary roots, $\pm i\sqrt{2}/2$, and Hamiltonian (14) cannot be reduced to the sum of the Hamiltonians for two uncoupled oscillators. In the elliptical problem, the $\mu = \mu(e)$ curve, which is the boundary of the instability region, emerges from the point $(\mu_*, 0)$ of the μ, e plane. We represent its equation at low eccentricities as a series of form (1):

$$\mu = \mu_* + e\mu_1 + e^2\mu_2 + ... \tag{15}$$

We substitute this expression for μ in function (14), perform an expansion in a powers series of e, and introduce the new variables x_1, x_2, X_1, X_2 in place of the variables q_1, q_2, p_1, p_2 using the formulas

$$\begin{aligned}
q_1 &= -\frac{7\sqrt{22}}{44}x_2 - \frac{\sqrt{11}}{2}X_1,\\
q_2 &= \frac{14\sqrt{11}}{121}x_1 + \frac{15\sqrt{506}}{484}x_2\\
&\quad + \frac{\sqrt{253}}{22}X_1 + \frac{2\sqrt{22}}{11}X_2,\\
p_1 &= \frac{109\sqrt{11}}{484}x_1 - \frac{15\sqrt{506}}{484}x_2\\
&\quad - \frac{\sqrt{253}}{22}X_1 + \frac{3\sqrt{22}}{44}X_2,\\
p_2 &= -\frac{7\sqrt{253}}{484}x_1 - \frac{193\sqrt{22}}{484}x_2\\
&\quad - \frac{7\sqrt{11}}{22}X_1 - \frac{\sqrt{506}}{44}X_2.
\end{aligned}$$

This change of variables is a univalent canonical transformation. In the new variables, the Hamiltonian has form (2), where H_0 is given by formula (3) in which $\omega = \sqrt{2}/2$.

Based on the algorithm described above, we calculated the first four coefficients μ_i of expansion (15) using computer systems of analytical calculations. The sought equation for the boundary of the instability region turned out to have the following form near the critical mass ratio μ_*:

$$\begin{aligned}
\mu &= \frac{1}{2} - \frac{\sqrt{69}}{18} + \frac{2\sqrt{69}}{207}e^2 + \frac{13}{250}e^4 + O(e^5)\\
&= 0.03852 + 0.08026e^2 + 0.05212e^4 + O(e^5).
\end{aligned}$$

This expression agrees with the result by Nayfeh and Kamel (1970), who obtained the corresponding expansion to within the second order of e inclusive.

ON THE STABILITY OF THE STATIONARY ROTATION OF A SATELLITE

Let the center of mass of a satellite moves in an elliptical orbit of eccentricity e in a central Newtonian gravitational field. The satellite is a rigid body whose central ellipsoid of inertia is an ellipsoid of revolution. We denote the equatorial and polar moments of inertia by A and C, respectively.

As Sarychev (1965) showed, the problem of the motion of a satellite relative to the center of mass under the effect of gravitational moments admits of a particular solution for which the axis of dynamical symmetry of the satellite is perpendicular to the orbital plane and the satellite itself rotates around the axis of symmetry with an arbitrary constant angular velocity r_0.

The Hamiltonian that corresponds to the linearized equations of perturbed motion for the axis of symmetry near the normal to the orbital plane is (Markeev 1967)

$$\begin{aligned}
H &= \frac{1}{2(1+e\cos\nu)^2}(p_1^2 + p_2^2) \qquad (16)\\
&\quad + \left[\frac{\alpha\beta(1-e^2)^{3/2}}{(1+e\cos\nu)^2} - 1\right] q_1p_2 + q_2p_1\\
&\quad + \frac{1}{2}\left[\frac{\alpha^2\beta^2(1-e^2)^3}{(1+e\cos\nu)^2} - \alpha\beta(1-e^2)^{3/2}\right.\\
&\quad \left. + 3(\alpha-1)(1+e\cos\nu)\right] q_1^2 + \frac{1}{2}\alpha\beta(1-e^2)^{3/2}q_2^2,
\end{aligned}$$

where $\alpha = C/A$, $\beta = r_0/\omega_0$ ($0 < \alpha \le 2$, $-\infty < \beta < \infty$), ω_0 is the mean orbital motion of the center of mass; the true anomaly ν is taken as an independent variable.

At $e = 0$, the characteristic equation for the linearized system is (Beletskiĭ 1975)

$$\begin{aligned}
\lambda^4 + k_1\lambda^2 + k_2k_3 &= 0, \qquad (17)\\
k_1 &= \alpha^2\beta^2 - 2\alpha\beta + 3\alpha - 1,\\
k_2 &= \alpha\beta - 1, \quad k_3 = \alpha\beta + 3\alpha - 4.
\end{aligned}$$

In regions I and II specified, respectively, by the inequalities $k_2 > 0$, $k_3 > 0$ and $k_2 < 0$, $k_3 < 0$, $k_1 > 2\sqrt{k_2k_3}$, the roots of the characteristic equation (17) are purely imaginary and different. Therefore, the studied stationary rotation of the satellite around the normal to the orbital plane is stable in the linear approximation.

Next, let us analyze the stability of the rotation of the satellite in the case of a low-eccentricity orbit for the values of α and β that lie at or near the $k_1 =$

$2\sqrt{k_2k_3}$ boundary of region II. In parametric form, this boundary can be specified by the equalities

$$\alpha = \alpha(\eta) = \frac{1}{3}(2 + 2\eta - 2\eta^2 + 2\eta^3 - \eta^4),$$
$$\beta = \beta(\eta) = \frac{1-\eta^2}{\alpha(\eta)},$$

where $0 < \eta < \eta^*$, and $\eta^* = 1.83041$ is the root of the equation $\alpha(\eta) = 0$. At the boundary considered, the characteristic equation (17) has two identical pairs of purely imaginary roots, $\pm i\omega$, where $\omega = \sqrt{\eta(\eta^2 - \eta + 1)}$.

The linear transformation $q_1, q_2, p_1, p_2 \to x_1, x_2, X_1, X_2$ given by the formulas

$$q_1 = \frac{(\eta-1)^2}{4\omega^2\kappa}x_2 - \frac{\eta\kappa}{\omega}X_1,$$
$$q_2 = -\frac{(\eta-1)^2}{4\omega\eta\kappa}x_1 + \kappa X_2,$$
$$p_1 = \frac{3\eta^3 - \eta^2 + \eta + 1}{4\omega\eta\kappa}x_1 + (\eta-1)\kappa X_2,$$
$$p_2 = -\frac{3\eta^3 - \eta^2 + \eta + 1}{4\omega^2\kappa}x_2 - \frac{\eta(\eta-1)\kappa}{\omega}X_1,$$
$$\kappa = \sqrt{(\eta^2+1)/(2\eta)},$$

is canonical univalent and reduces (Sokol'skiĭ 1980) the unperturbed (at $e = 0$) Hamiltonian (16) to form (3). Consequently, for a circular orbit, the stationary rotation of the satellite is unstable at the $k_1 = 2\sqrt{k_2k_3}$ boundary of region II. At low eccentricities, we restrict our analysis to the case of a multiple resonance where the number 2ω is integer.

The function $\omega(\eta)$ monotonically increases, and the inequality $0 < \omega < \omega(\eta^*) = 2.14771$ holds in the range $0 < \eta < \eta^*$ of admissible values of the parameter η. Therefore, a multiple resonance is possible only at four values of η: (1) $\eta = \eta_1 = 0.319448$ ($2\omega = 1$), (2) $\eta = \eta_2 = 1$ ($\omega = 1$), (3) $\eta = \eta_3 = 1.41597$ ($2\omega = 3$), (4) $\eta = \eta_4 = 1.74296$ ($\omega = 2$). These resonances occur at the points $P_i(\alpha_i, \beta_i)$ ($i = 1, 2, 3, 4$), where $\alpha_i = \alpha(\eta_i)$, $\beta_i = \beta(\eta_i)$, with $\alpha_1 = 0.82986$, $\beta_1 = 1.08205$; $\alpha_2 = 1$, $\beta_2 = 0$; $\alpha_3 = 0.82668$, $\beta_3 = -1.21569$; $\alpha_4 = 0.25704$, $\beta_4 = -7.92834$.

The stability of the stationary rotation of a satellite at $\beta = 0$ and arbitrary eccentricities was previously analyzed by Markeev and Chekhovskaya (1976). Therefore, we consider below only three multiple resonances that correspond to the points P_j ($j = 1, 3, 4$).

Let the orbital eccentricity be low, but nonzero. At the boundaries of the instability regions that degenerate at $e = 0$ into the points P_j, $\alpha - \alpha_j$ and $\beta - \beta_j$ have the first or higher order of smallness in e. Using the algorithm described above, we constructed equations for the $\alpha - \alpha_j = S_j(\beta - \beta_j, e)$ surfaces that bound the stability and instability regions in the space of three parameters, α, β, and e. The functions S_j were represented as power series of e and $\beta - \beta_j$. To the second-order terms inclusive, these are

$$S_1 = 0.16514e - 0.31036(\beta - \beta_1) + 0.03597e^2 + 0.42937e(\beta - \beta_1) - 0.04003(\beta - \beta_1)^2,$$
$$S_3 = 0.20376(\beta - \beta_3) + 0.04393e^2,$$
$$S_4 = 0.02779(\beta - \beta_4) - 0.35240e^2.$$

The sections of the derived surfaces by the $\beta = \beta_j = \text{const}$ planes are the $\alpha = \alpha_j^*(e)$ curves in the α, e plane that specify the boundaries of the stability ($\alpha > \alpha_j^*$) and instability ($\alpha < \alpha_j^*$) regions at low e near the point $(\alpha_j^*, 0)$, $j = 1, 3, 4$. The functions $\alpha_j^*(e)$ were found to be

$$\alpha_1^* = \alpha_1 + 0.16514e + 0.03597e^2 + O(e^3),$$
$$\alpha_3^* = \alpha_3 + 0.04393e^2 + O(e^3),$$
$$\alpha_4^* = \alpha_4 - 0.35240e^2 + O(e^3).$$

CONCLUSIONS

For a linear Hamiltonian system in the case where the eigenvalues of the matrix for the unperturbed system are purely imaginary, but the matrix itself is not reducible to diagonal form, we proposed a constructive algorithm for constructing the boundaries of the regions of parametric resonance. This algorithm was used to determine the boundaries of the instability regions in the problems of the stability of libration points and the stability of the stationary rotation of a satellite around the normal to the plane of the elliptical orbit of its center of mass.

ACKNOWLEDGMENTS

This work was supported by the Russian Foundation for Basic Research (project no. 02-01-00831) and a grant from the President of Russia for support of leading scientific schools (no. NSh-1477.2003.1).

REFERENCES

1. V. V. Beletskiĭ, *The Motion of a Satellite Relative to the Center of Mass in a Gravitational Field* (Mosk. Gos. Univ., Moscow, 1975).

2. G. E. O. Giacaglia, *Perturbation Methods in Non-Linear Systems* (Springer-Verlag, Berlin, 1972; Nauka, Moscow, 1979).
3. A. P. Markeev, Kosm. Issled. **5**, 530 (1967).
4. A. P. Markeev, *Libration Points in Celestial Mechanics and Cosmodynamics* (Nauka, Moscow, 1978).
5. A. P. Markeev and T. N. Chekhovskaya, Prikl. Mat. Mekh. **40**, 1040 (1976).
6. A. P. Markeev, S. V. Medvedev, and A. G. Sokol'skiĭ, *Normalization Methods and Algorithms for Differential Equations* (Mosk. Aviats. Inst., Moscow, 1985).
7. A. H. Nayfeh and A. A. Kamel, AIAA J. **8**, 221 (1970).
8. V. A. Sarychev, Kosm. Issled. **3**, 667 (1965).
9. A. G. Sokol'skiĭ, Kosm. Issled. **18**, 698 (1980).
10. V. A. Yakubovich and V. M. Starzhinskiĭ, *Parametric Resonance in Linear Systems* (Nauka, Moscow, 1987).

Translated by V. Astakhov

Astronomy Letters, Vol. 31, No. 5, 2005, p. 357.

ERRATA

Erratum: "Two-Mirror Schwarzschild Aplanats: Basic Relations" [*Astron. Lett.* 31 (2), 129 (2005)]

V. Yu. Terebizh

The Editorial Board apologizes for a mistake allowed into the above article. The final sentence in the footnote on p. 129 should have read as follows:

"Using only part X of Schwarzschild's fundamental research of 1905, the above authors duplicated, in another form, some of the results contained in Part II of this study."